ABSTRACT

Title of Dissertation:	INTEGRATED MICROSYSTEM-BASED APPROACH FOR DETECTION AND TREATMENT OF BACTERIAL BIOFILMS ON URINARY CATHETERS
	Ryan Cornelis Huiszoon, Doctor of Philosophy, 2020
Dissertation directed by:	Professor Reza Ghodssi, Department of Electrical and Computer Engineering, Institute for Systems Research

Biofilms are a ubiquitous mode of growth for bacteria and present a significant challenge in healthcare due to their resistant nature towards traditional antibiotic therapy. Particularly, biofilms can form on indwelling urinary catheters, leading to catheter-associated urinary tract infections, which are one of the most prevalent healthcare-acquired infections. In recent years, microsystems-based approaches have been developed to measure and study bacterial biofilms. In this dissertation, microsystems are adapted for the catheterized urinary tract environment to address biofilm infections *in situ*. Specifically, a proof-of-concept device comprised of gold interdigitated electrodes on a flexible polyimide substrate is fabricated and characterized *in vitro*. This substrate allows the device to conform seamlessly with the cylindrical surface of a catheter. Real-time impedance sensing is demonstrated, showing an average decrease in impedance of 30.3% following 24 hours of biofilm growth. The device also applies the bioelectric effect, which yields an increase in impedance of 12% and the lowest biomass relative to control treatments. Furthermore, 3D-printed molds and commercial modeling software show that the cylindrical conformation does not have an appreciable impact on performance. This device is integrated with

a commercially available Foley catheter using two disparate approaches: (1) integration of the flexible proof-of-concept device using a 3D-printed catheter insert and (2) electroless plating directly onto the catheter lumen. In addition to electrode integration, miniaturized electronic systems are developed to control sensing and treatment wirelessly with a minimal form factor. A smartphone mobile application is developed in conjunction with this effort, to provide a user-friendly interface for the system. Several functions are verified with the integrated system, including biofilm sensing, wireless signal transmission, bladder drainage, and balloon inflation. To decrease the risk associated with this system for future research *in vivo* and in a clinical setting, sensing and treatment are evaluated under realistic conditions. The biochemical aspect of the catheterized environment is recreated using artificial urine, and the physical aspect is recreated using a silicone model of a human bladder and a programmable pump. A 13.0% decrease in impedance is associated with bacterial growth; this decreased magnitude relative to the proof-of-concept device is due to the reduced degree of growth in artificial urine. The bioelectric effect is demonstrated as well, showing a reduction in planktonic bacteria of 1.50×10^7 CFU/ml and adhered biomass equivalent to $OD_{590nm} = 0.072$ relative to untreated samples. This work provides a framework for developing microsystem-based tools for biofilm infection management and research from proof-of-concept to integrated system, particularly for CAUTI. The results demonstrate that the cylindrical conformation does not interfere with device sensing or treatment performance and that the system maintains functionality under realistic conditions, laying the groundwork for future *in vivo* and clinical testing. The system will provide *in situ* and real-time data regarding catheter biofilm colonization in a way that is not possible with existing techniques. Finally, the system can serve to reduce reliance on antibiotics and reduce the spread of antibiotic resistance in CAUTI and other vulnerable areas.

INTEGRATED MICROSYSTEM-BASED APPROACH FOR DETECTION AND TREATMENT OF BACTERIAL BIOFILMS ON URINARY CATHETERS

by

Ryan Cornelis Huiszoon

Dissertation submitted to the Faculty of the Graduate School of the
University of Maryland, College Park, in partial fulfillment
of the requirements for the degree of
Doctor of Philosophy
2020

Advisory Committee:
Professor Reza Ghodssi, Chair
Professor William E. Bentley
Professor Giuliano Scarcelli
Professor James N. Culver
Professor Vincent T. Lee, Dean's Representative

Dedication

To my parents,

who have provided unending support for my education,

and

to Helen,

whose love and partnership helped make this work possible.

Acknowledgements

I would like to thank my advisor, Professor Reza Ghodssi for his guidance and support over the course of this work. I would also like to thank the members of my dissertation committee, Professor William Bentley, Professor Giuliano Scarcelli, Professor Vincent Lee, and Professor James Culver, for their feedback and effort when completing this dissertation.

It is also important to acknowledge the contributions of former and current members of the MEMS Sensors and Actuators Lab for their assistance at every stage of this project. I would like to thank Dr. Sowmya Subramanian for her mentorship when I first began working on this project and in the lab. I am also thankful for the support of Dr. Sangwook Chu, who assisted greatly with the design and testing of the integrated system, and Dr. Luke Beardslee, who contributed to the design of the fabrication process and the printed circuit board. I am also grateful for each of the members of MSAL, Justin Stine, Ashley Chapin, Anthony Chung, Joanna Avery, and Jinjing Han, who helped me throughout my time working in the lab with thoughtful discussions and feedback. I also appreciate the help of the former members Dr. George Banis, Dr. Pradeep Ramiah Rajasekaran, Dr. Faheng Zang, Dr, Hyun Jung, Dr. Thomas Winkler, Himanshu Singhal, Nabid Ahmed, and Mayavan Sathyam for their insight and support. Furthermore, I am thankful for the undergraduates, Sam Preza, Justin Greene, and Dylan Jesner, that I had the opportunity to work with at MSAL for giving their time and effort on my project. I also need to thank our collaborators in the Bentley lab, Malik lab (Dr. Rena Malik), Sears lab (Dr. Cindy Sears and Dr. Shaoguang Wu), and Scarcelli lab (Dr. Jitao Zhang) for their expertise), materials, and facilities. I would also like to thank Dr. Rodney Donlan at the CDC for providing the inspiration for adapting these microdevices for catheters.

I would also like to acknowledge the support I received from Alla McCoy, Piotr Kulczakowicz, and Afsarul Mir from the University of Maryland Office of Technology Commercialization for their help marketing the inventions which arose from this project. I also want to thank Lou Cantoloupo, Yanfeng Wang, and Ric Hughen for their efforts conceptualizing the commercialization aspects of this work. I also appreciate the support of Harbor Designs and Manufacturing for their help designing the 3D-printed insert, notably Kevin Kubit. In addition, I am thankful for John Hadeed and JMH Technologies for their help constructing the mobile application. The Maryland Nanocenter and FabLab provided support for fabrication activities throughout this project, and I would particularly like to thank Mark Lecates for training me on each of the tools. I would also like to acknowledge Terrapinworks for their 3D-printing facilities. I also appreciate all of the help that I have received from the administrative staff at ISR and BIOE, including Regina King, Vicci Barrett, Carla Scarbor, Julianna Bynoe, Dawn Wheeler, Dr. Tracy Chung, and Bill Churma. This work was only possible thanks to the funding support from the NSF (under program manager Shubra Gangopadhyay through ECCS 1809436), TEDCO Maryland Innovation Initiative, and the Maryland Medical Device Development Fund.

Finally, I would like to thank my family and friends. My parents Jacquie and Cornelis, along with my sister Rietta, have always been so supportive of my education and have made it possible for me to succeed. I have also had the benefit of a strong support group in Maryland that have helped me relax and have fun, notably Andrew Lamont, Emily Gosselin, Mike Moulton, and Sarah Van Belleghem. Most importantly, I thank Helen for her unwavering support through the highs and lows, which has made completing this project possible, and for her boundless love that completes my life.

Table of Contents

List of Tables

List of Figures

List of Abbreviations

CDC	The United States Centers for Disease Control and Prevention
CAUTI	Catheter-Associated Urinary Tract Infection
IDE	Interdigitated Electrodes
PCB	Printed Circuit Board
FEA	Finite Element Analysis
EDL	Electrochemical Double Layer
QCM	Quartz Crystal Microbalance
QCM-D	Quartz Crystal Microbalance with Dissipation Monitoring
IM	Impedance Microbiology
SAW	Surface Acoustic Wave
EIS	Electrochemical Impedance Spectroscopy
ECM	Extracellular Matrix
BE	Bioelectric Effect
CV	Cyclic Voltammetry
DPV	Differential Pulse Voltammetry
PDMS	Polydimethylsiloxane
CRM	Confocal Reflection Microscopy
LOC	Lab-on-a-Chip
CVS	Crystal Violet Staining
SEM	Scanning Electron Microscopy
SR-FTIR	Synchrotron Radiation-based Fourier Transform Infrared
SPR	Surface Plasmon Resonance

CCD	Charge-Coupled Device
LED	Light Emitting Diode
OD	Optical Density
LB	Lysogeny Broth
DMEM	Dulbecco's Modified Eagle Medium
FBS	Fetal Bovine Serum
DI	Deionized
UV	Ultraviolet
EDS	Energy Dispersive Spectroscopy
MCU	Microcontroller Unit
BLE	Bluetooth Low Energy
CFU	Colony Forming Unit
PR	Photoresist
COTS	Commercial-off-the-shelf
RSSI	Received Signal Strength Indicator

Chapter 1: Introduction

1.1 Motivation & Background

Nosocomial infections remain a significant challenge in healthcare, accounting for a significant number of infections and contributing a large burden in terms of additional healthcare costs and patient-days [1]. These infections also disproportionately impact vulnerable patient populations in hospitals, such as the elderly or immunosuppressed individuals [2], [3]. Urinary tract infections, pneumonias, bloodstream infections, and surgical site infections comprise the most prevalent nosocomial infections [2]. Nosocomial urinary tract infections are predominantly associated with the use of an indwelling urinary catheter and can lead to a range of complications, like pyelonephritis and sepsis [4]. Despite recent research efforts, the typical approaches for diagnosing these infections still rely on the identification of symptoms that are often non-specific and urine bacterial cultures. In addition, conventional treatment relies upon administration of antibiotics [5]–[8].

The United States Centers for Disease Control and Prevention (CDC) guidelines for urinary catheter use do not recommend changing catheters at routine intervals. Rather, they suggest that catheters only be changed in response to clinical indications [9]. However, these indications typically only appear after an infection has developed, leading to entirely reactive interventions. The CDC guidelines also suggest that prophylactic antibiotics not be used routinely, due to the spread of antibiotic resistance [9]. This guidance represents an opportunity for improving the standard of care for catheterized patients and reducing the incidence of catheter-associated urinary tract infections (CAUTI) by identifying catheters at risk for developing these infections before symptoms are present. Furthermore, this guidance highlights the need to develop interventions that reduce the reliance on significant doses of antibiotics.

CAUTI development is driven by the attachment of bacteria to the catheter surface and subsequent biofilm formation [10]. Bacterial biofilm formation occurs when adhered bacteria at a threshold population encase themselves in a protective extracellular matrix, which offers numerous survival advantages. The matrix and the constituent cells comprise a biofilm. Bacterial biofilms are notably more tolerant of antibiotic therapy than their planktonic counterparts, and they can serve as a source of infection as bacterial cells shed and spread [11], [12]. Indwelling urinary catheters are inevitably colonized by biofilm, which, in turn, contribute to the development of CAUTI and difficulty associated with treating CAUTI.

In this dissertation, I hope to leverage microsystems technology to develop a system that can help address CAUTI. Microsystems have been extensively explored in recent years as a means for studying bacterial biofilms [13]. Microfluidic systems have reduced the required reagent volumes and decreased the variability associated with biofilm growth to enable high-throughput and reproducible studies [14]. Microscale sensors integrated within microfluidic systems offer unprecedented real-time information regarding the formation of biofilm and its response to novel antimicrobials [13]. The real-time biofilm monitoring offered by these sensors would provide significant utility for the management of implanted and indwelling medical devices by providing continuous data regarding the degree of colonization on the surface and efficacy of interventions. Identification of biofilm formation on a medical device like an indwelling urinary catheter could give healthcare providers an indication to remove the device if feasible or implement a prompt targeted treatment. In particular, microscale impedance sensors comprised of a pair of interdigitated electrodes (IDEs) provide a simple, low-power approach for continuous biofilm monitoring [15], [16].

In addition to detection of biofilm, microsystems can also be utilized to implement anti-biofilm therapy. Notably, the bioelectric effect (BE) has been demonstrated in a microfluidic system for biofilm reduction [16]. The BE consists of a low-intensity electric field that increases the susceptibility of the bacteria in the biofilm to antimicrobial compounds [17]. This effect can significantly reduce the antibiotic dosage needed for effective biofilm removal and infection clearance [12]. IDEs used for biofilm monitoring can also be used to generate the electric field needed for the BE, enabling a dynamic, feedback-driven treatment that can be applied in response to real-time information regarding biofilm formation on the surface [16]. This targeted treatment only requires a low dose of antibiotics compared to conventional infection therapy.

There are several barriers to widespread implementation of this approach for CAUTI management. Individuals involved in potentially translational research must consider how these planar systems can be integrated with actual medical devices that have complex surface geometries, such as the cylindrical lumen of a urinary catheter. They must also consider how these systems will operate in the physical and biochemical environment of the catheterized bladder. Finally, the system must be user-friendly to facilitate use by those without specific expertise.

1.2 Summary of Accomplishments

To my knowledge, there have been no studies that have developed integrated microsystems for both the detection and treatment of bacterial biofilms on urinary catheters. This type of approach has the potential to improve the lives of millions of patients worldwide. My research in this dissertation focuses on the development of integrated microsystems for biofilm monitoring and BE-based treatment on urinary catheters. This involves the adaptation of planar monitoring and treatment microelectrodes onto flexible substrates that conform to the cylindrical catheter surface. These flexible electrodes are then integrated with commercially available Foley catheters,

and the impedance sensing and BE-based treatment functionality is evaluated in a synthetic bladder model. The system developed in this thesis (Figure 1-1) enables care providers and researchers to identify biofilm colonization in real-time, which can potentially serve as a clinical indication for prompt treatment or catheter removal. This system also functions to administer the BE, reducing the reliance on antibiotics in CAUTI management. This dissertation achieves several important milestones towards improving CAUTI management and developing devices that address challenges associated with biofilm formation. The proof of concept demonstration in a cylindrical environment is the first flexible electrode system for biofilm detection and treatment, enabling these functionalities on a wide range of vulnerable surfaces. Integrating this system with the commercially available Foley catheter yielded a first of its kind system for managing biofilm in the urinary catheter environment. The custom developed printed circuit board (PCB) and mobile application helped make the integrated system user-friendly by providing a facile interface for controlling monitoring and treatment administration. The unique bladder model allowed *in vitro* characterization of this integrated system in a realistic environment to achieve a better understanding of how these devices will perform in the catheterized bladder.

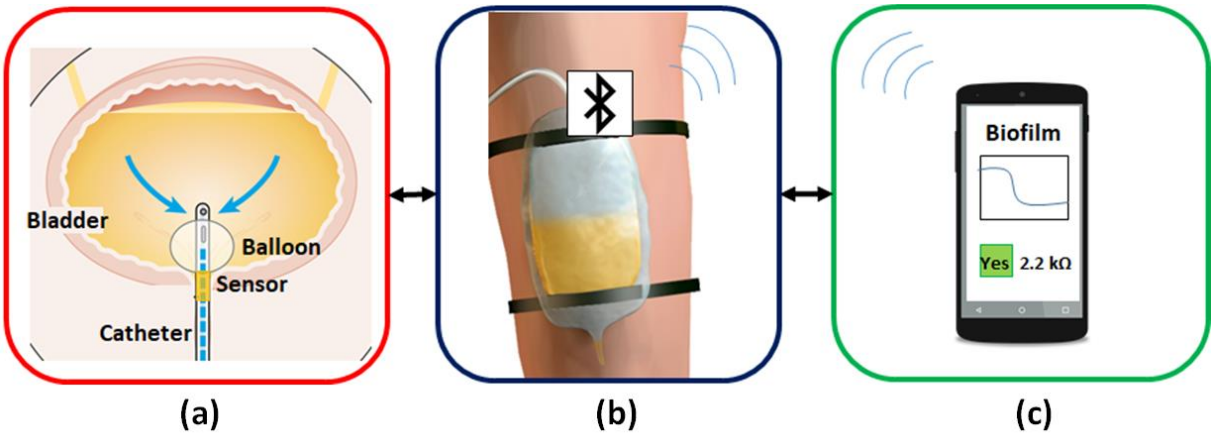

Figure 1-1: Overview schematic of integrated catheter biofilm management system: (a) Flexible sensor embedded in urinary catheter; (b) Wireless electronics module attached to external catheter bag; (c)

Smartphone application that provides an alert in the presence of biofilm and allows prompt implementation of treatment [18].

1.2.1 Flexible device for biofilm sensing and treatment in cylindrical environments

This thesis relies on previously published mechanisms for biofilm detection and treatment [16]. An IDE impedance sensor provides sensitive, nondestructive, and real-time monitoring of biofilm growth. In addition, these electrodes can be used to administer a low-intensity electric field that induces the BE. However, such lab-on-a-chip (LOC) systems typically utilize planar and rigid substrates that are incompatible with the complex surfaces of medical devices. This work overcomes this limitation by fabricating IDEs on flexible polyimide film that conforms seamlessly to the catheter surface. This flexible sensor enables real-time impedance measurements of the growth on the cylindrical surface, displaying similar trends to the previously reported LOC systems. The same IDEs allowed administration of the BE, showing a significant decrease in biomass adhered to the sensor. Furthermore, I examine how the device performance changes in the cylindrical catheter-scale geometry. COMSOL Multiphysics finite element analysis (FEA) simulations as well as sensor curvature experiments show relatively little change from planar to cylindrical surfaces at the catheter size scale. This proof-of-concept study provides the basis for my subsequent chapters exploring an integrated system for use in a catheterized bladder environment. In addition, this helps provide a more complete understanding of the relationship between electrode devices and the geometric space they operate in.

1.2.2 Foley catheter-integrated system for biofilm infection management

A key element of this thesis is the integration of a flexible monitoring and treatment device with a commercially available Foley catheter. The indwelling Foley catheter is one of the most commonly used medical devices, and is particularly vulnerable to biofilm colonization [10], [19]. A barrier to implementation is seamlessly integrating the electrodes with the catheters without

interfering with routine catheter function. This design is constrained by the design of the Foley catheter itself, which is highly standardized and uniform. I used a 3D-printed insert module to interface the sensor with the catheter, which can be incorporated post-production at a cut perpendicular to the catheter axis. The insert cytotoxicity was evaluated to help understand the safety of such a system. A custom PCB was developed to run both functions of the system via Bluetooth, which was controlled by a custom mobile application. The wireless control system, together with the insert module, comprised the integrated system. This novel system allows numerous future research and clinical studies regarding CAUTI and CAUTI management and generates insights into systems integration for medical devices.

1.2.3 Detection and treatment in synthetic model of catheterized bladder

One of the most significant barriers to translating *in vitro* LOC systems onto medical devices is the environment where these systems must operate. In particular, for CAUTI, this system must function in the catheterized bladder, exposed to urine under variable flow conditions. In this dissertation, I developed a synthetic bladder model in order to study the operation of an integrated biofilm detection and treatment system under realistic conditions. This model consists of a silicone bladder, artificial urine, and a programmable pump to recreate the biochemical and physical aspects of bacterial growth and their impact on system operation. I performed impedance sensing experiments using the integrated system in this model, confirming the viability of this approach for detecting more clinically relevant bacterial growth on catheters. Electrochemical impedance sensors of this type are impacted significantly by the composition of the media that they are immersed in, and this demonstration supports their use in this setting. The efficacy of the BE was also examined using this model, showing a decrease in biomass relative to untreated controls. This is the first study using a microsensor-based integrated system to detect bacterial growth and

administer BE-based treatment in a realistic setting. The accomplishments of this thesis lay the groundwork for future clinical studies using this integrated prototype.

1.3 Literature Review

1.3.1 Bacterial biofilms

Bacterial biofilms are ubiquitous in healthcare and the environment, representing the dominant mode of growth for bacterial microorganisms [20]. Biofilms present a significant challenge because they afford bacteria significant survival advantages compared to their planktonic counterparts, including increased tolerance to antimicrobial therapies [11], [12]. Limited diffusion into the biofilm matrix and the decreased metabolic rate of the constituent bacteria often allows biofilm to become highly tolerant to antibiotic therapy; an antibiotic dose 500–5000 times larger than that for planktonic bacteria is required to eliminate the biofilm and associated infection [11], [12]. In addition, increased horizontal gene transfer between bacterial cells within biofilms can help to exacerbate the spread of antibiotic resistance [21], [22]. Biofilms are implicated in numerous nosocomial infections, including surgical-site, bloodstream, and urinary tract infections often associated with medical implants, venous catheters, or urinary catheters, respectively [23]. Overall, these infections were estimated to be responsible for 67% of all hospital-acquired infections in the United States of America in 2002 [24]. Furthermore, bacterial biofilms are critical in the development of CAUTI, often leading to infections for patients with long-term indwelling catheters [10]. It should be noted, however, that not all biofilms lead to CAUTI [25].

Bacteria form sessile biofilm communities when they adhere to a hydrated surface such as that of a urinary catheter and, at a threshold population, encase themselves in a self-produced extracellular matrix (ECM) consisting primarily of polysaccharides and extracellular DNA, as well

as lipids and proteins [11], [20]. This process is depicted in Figure 1-2. The bacteria initially adsorb to the surface reversibly due to physical forces. They then undergo irreversible attachment through bacterial appendages like flagella, fimbriae, pili, and adhesins [10], [26]. The adhered bacteria communicate via small molecules through a process called quorum sensing, which coordinates their phenotype to become a biofilm [27]. The biofilm will continue to develop into a complex, mature biofilm structure from which bacteria disperse throughout the environment. These dispersed bacteria allow additional areas of the system to be colonized by biofilm and can serve as a source of persistent infections if the original biofilm is not removed [11]. Persister cells with relatively low metabolic activity compared to the other biofilm bacteria can survive antibiotic therapy and can repopulate a biofilm once the treatment regimen has been concluded [28], [29]. This leaves catheters or medical implants susceptible to recurring infections that can only be treated by removing the device or implant, often requiring revisional surgery [30]. Early detection of the biofilm formation, along with novel antibiofilm schemes, will thus help prevent these recurring infections.

Bacteria in biofilms are highly resistant to traditional antibiotic therapy compared to their planktonic counterparts [12]. Therefore, given the importance of biofilms in many infections, it is vital to consider treatments specifically designed to address biofilms. A number of different strategies have been explored, but these have not achieved widespread implementation for CAUTI care. Enzyme-based treatments, which degrade critical components of the biofilm ECM, have been developed for use against wound biofilms [31]. Another strategy involves interrupting the intracellular quorum sensing communication that bacteria use to drive biofilm formation. Specifically, a synthetic analog molecule of the universal signaling molecule, autoinducer-2, can interfere with this pathway via competitive inhibition and not allow the bacteria to express the

biofilm phenotype in a process known as quorum quenching [32], [33]. Quorum quenching can be implemented in conjunction with antimicrobials to achieve a more effective clearance [34]. The cells do not have the same protection that they have in a biofilm and are thus more vulnerable to the antimicrobial. Laser-induced nanobubbles have also been demonstrated to increase the susceptibility of specific biofilms to specific antibiotics, but this approach is only viable for wound biofilms that are not embedded deep within the body [35]. Biofilms have also been physically dispersed using low frequency ultrasound [36].

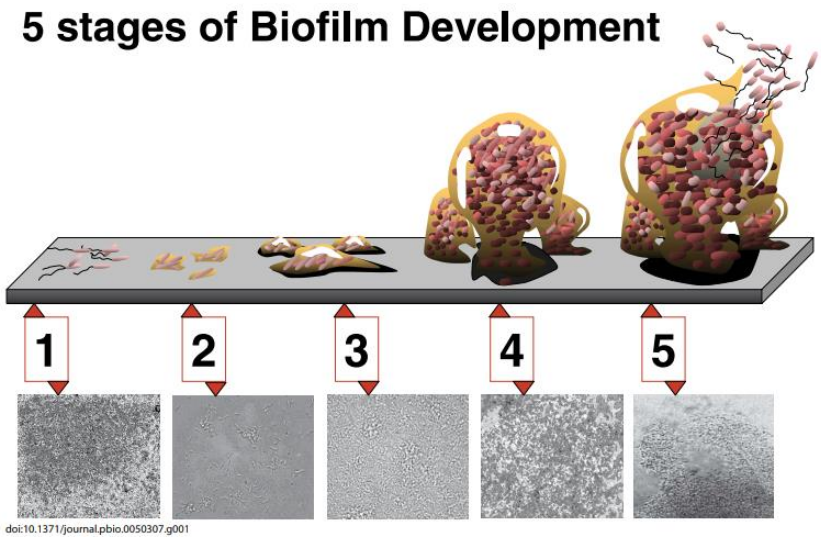

Figure 1-2: The five stages of biofilm development: (1) initial attachment, (2) irreversible attachment and initial matrix secretion, (3) colony maturation I, (4) maturation II, and (5) dispersion. Each stage has an accompanying image of *Pseudomonas aeruginosa* biofilm [37].

Another strategy developed to treat biofilms is the BE, which combines a low-intensity electric field with a low antibiotic dosage for synergistic biofilm clearance [17]. Exposing the biofilm to the electric field leads to a dramatic decrease in the necessary antibiotic concentration, at least two orders of magnitude lower, needed to completely kill the cells [38]. There are several hypotheses that attempt to explain this phenomenon, including electrochemical generation of

reactive ions, electrophoretic augmentation of antimicrobial transport, and electroporation [39]. The BE has also been demonstrated using biocides or quorum sensing inhibitors, as opposed to antibiotics [40], [41]. Other antibiofilm strategies, like electroceutical wound dressings, rely on an applied voltage alone to generate reactive compounds that can clear biofilm [42], [43]. This strategy relies on higher voltages and specific material interactions that are not applicable in all environments, particularly indwelling medical device applications.

1.3.2 Biofilm microsystems for characterization and treatment

While biofilms have been studied for decades, much is still unknown [44]. Over the last few decades, a number of *in vitro* models have been developed to not only understand the biology of biofilms, but also to study the response of biofilm to external stimuli such as pH changes or exposure to antimicrobials [45]–[51]. Biofilm characterization and evaluation often relies on bulky external quantification equipment or laborious protocols that label components of the biofilm and destroy the biofilm itself [52], [53]. Therefore, there is an urgent need to develop scalable and reliable systems that can noninvasively quantify and characterize biofilms. Considering the broad variations of the real environmental settings where biofilms form (e.g. implanted devices, surgical tools, etc.), it is also essential to develop different characterization methods in parallel to address the varying clinical needs.

Here, I give an in-depth overview of novel microtechnological approaches for biofilm characterization. Microscale devices and LOC sensing platforms have been considered an ideal solution to address this multi-faceted problem. Microfluidics provide several advantages including ease of fabrication, low reagent volumes and cost, tight environmental control, and high throughput; the implementation of microfluidic devices for biofilm studies has been discussed in detail by Greener et al. [14]. The review provides an in-depth view of polydimethyl siloxane

(PDMS) microchannel devices and the conventional metrology tools that these devices rely on. This section of my thesis discusses the microscale sensing technologies that can be used to evaluate biofilms in real time for label-free, continuous, and noninvasive characterization of biofilm properties such as growth, treatment susceptibility, surface coverage, biomass, metabolic activity, and viscoelasticity. I aim to present some of the *in vitro* microsystems developed over the past few years for biofilm testing and treatment evaluation. In particular, I review systems relying on optical, mechanical, and electrochemical sensing mechanisms for biofilm characterization. These microscale LOC systems provide numerous advantages in biomedical research and clinical diagnostics and could be valuable tools for investigating novel therapies. They enable functional integration with other technologies, leading to portability and high-throughput usage. These translational systems hold the potential for improved resolution, regulation, sensitivity, and flexibility over more traditional approaches. In addition, these devices can provide a dense array of sensors at the micro-scale to further reduce the necessary sample volumes, in conjunction with microfluidic systems, and enable real-time and non-destructive biofilm analysis. These are critical elements for both biological testing for drug discovery and translational biofilm detection systems. Studies on the development of antibiotic resistance, biofilm growth, and the role of intercellular communication have been improved with the use of these microsystem approaches [34], [54]–[58]. Furthermore, it has been suggested that microdevices will reduce the necessary analysis time from days to the order of 2 to 4 hours with more accurate recognition of specific biological targets [59], [60].

1.3.2.1 Optical Biofilm Characterization

Traditional biofilm studies rely on standard optical techniques such as confocal microscopy, crystal violet staining (CVS), or scanning electron microscopy (SEM). Many studies

have been performed on various biofilms using these techniques [53], [61]–[63]. However, these labeling procedures are often destructive to the biofilm, meaning that only end-point measurements are obtainable. Furthermore, these approaches do not lend themselves to integration *in situ* or *in vivo* for clinical applications.

In recent years, other optical techniques that allow for real-time, non-invasive detection of biofilms have been developed. For example, Yawata et al. report a non-destructive, label-free biofilm formation monitoring system using an image analysis technique based on a modified confocal reflection microscopy (CRM) in a single channel, PDMS/glass microfluidic device [64]. To overcome the challenge of image saturation when using CRM, the authors modified the technique to allow for continuous manual adjustment of the detector gain while scanning along the Z-axis to maintain the signal intensity of cells at a constant level. This modification of CRM with continuous gain adjustment was termed Continuous Optimizing CRM. Using this technique, successful visualization of *Streptococcus mutans* biofilm growth was obtained every 12 hours over a 60-hour growth period.

Imaging at long, 12-hour intervals yields poor temporal resolution of biofilm formation and growth. However, real-time chemical imaging of bacterial activities can facilitate a more comprehensive understanding of the dynamics of biofilm structures and functions. This has been demonstrated using synchrotron radiation-based Fourier transform infrared (SR-FTIR) spectromicroscopy in an open-channel microfluidic system by Holman et al. [65]. This imaging technique has been known to yield high spatial resolution and label-free vibrational signatures of chemical bonds in biomolecules but has been restricted in use due to the water in biofilms, shown to hinder SR-FTIR sensitivity. This was overcome by Holman, who developed a simple open-channel microfluidic system with hydrophilic deep reactive ion-etched microstructures that can

circumvent the water-absorption barrier for chemical imaging of the developmental dynamics of bacterial biofilms with a spatial resolution of several micrometers. To image the biochemical properties and the distribution of bacteria before and after antibiotic application, the entire field-of-view of the biofilm was divided into equal-sized squares before raster scanning and collecting full SR-FTIR spectra at each position, followed by scan processing using different algorithms. Recently, Mattana et al. reported using optical methods to generate maps of the bulk chemical and mechanical properties of biofilm on the microscale [66]. Biofilm matrix stiffness was determined using Brillouin microspectroscopy, and the composition was mapped using Raman microspectroscopy. *Candida* biofilms were grown for 72 hours and dried for one week before being introduced into the custom microscope setup for imaging, which collects Brillouin spectra using a multi-pass tandem Fabry-Perot interferometer and Raman spectra with a dispersive monochromator. While these were done as end-point measurements, the authors report that this approach could be used to probe these properties of biofilms *in situ*.

Surface plasmon resonance (SPR) has been demonstrated as a means to characterize biofilm physiology optically. A PDMS microchannel in combination with a gold sensing surface on a glass prism enables real-time and label-free dissemination of the attachment and growth dynamics of *Escherichia coli* and *Pseudomonas aeruginosa* biofilms [67]. The change in the resonance peak of the light reflected from the gold sensing surface arises from a change in refractive index, attributable to the attached biofilm biomass. SPR offers non-destructive and continuous monitoring over a larger surface area than many other optical techniques (up to 1 cm^2). Fiber optical methods of detecting biofilms have also been reported [68], [69]. One group reports a fiber-optic sensing system to detect the formation of electroactive biofilms – biofilms whose metabolism involves extracellular electron transfer that can be modulated by electrical signals [70]

– via electrochemical-SPR, where biofilm formation on the fiber surface leads to a measurable shift in the refractive index [68]. Here, the optical fiber consists of a tilted fiber Bragg grating coated in a nano-gold film, which acts as the working electrode. The gold-coating offers simultaneous electrochemical and optical SPR-based measurements of biofilm in hard to reach environments.

Simpler fiber optical microsystems for biofilm detection have also been studied. Zhong et al. report a gold coated fiber optic sensor for detection of biofilm growth in bioreactors via fiber-optic evanescence wave spectroscopy [71]. The fibers have a U-shaped chemically etched region, which was used as the exposed sensing region; the etched unclad fiber sensing region served to increase the evanescent field intensities. Each sensor contains an uncovered sensing probe as well as a parallel reference probe coated in a porous polyimide-silica film. The reference probe measures light transmission through the liquid, while the sensing probe measures the transmission through both the liquid and the bacterial biofilm. The sensing probe was able to measure a significant percent decrease in transmission intensity when biofilm formed, both with and without flow. Phillip-Chandy et al. present a similar plastic optical fiber with its cladding removed over a sensitized length that measures the growth of biofilms in a closed loop water process system by evanescent field attenuation and intensity modulation [72]. The sensor detects biofilm build-up at the fiber surface by means of refractive index modulation. The authors show that the increase in refractive index associated with the biofilm on the surface reduces the intensity of light propagating in the fiber and attenuates the high order propagation modes.

Although the aforementioned methods provide high sensitivity, they require extensive data collection and processing. Thus, simpler methods of imaging that require less or almost no data processing have been suggested. Biofilm thickness in microfluidic channels can be determined

using simple off-the shelf optoelectronic devices, such as photodiodes or charge-coupled device (CCD) arrays, shown in Figure 1-3 [54], [73]. Here, the optical density gives a direct measure of the biofilm thickness, while the CCD array functions in deriving the spatiotemporal thickness of the biofilms along the length of the channel.

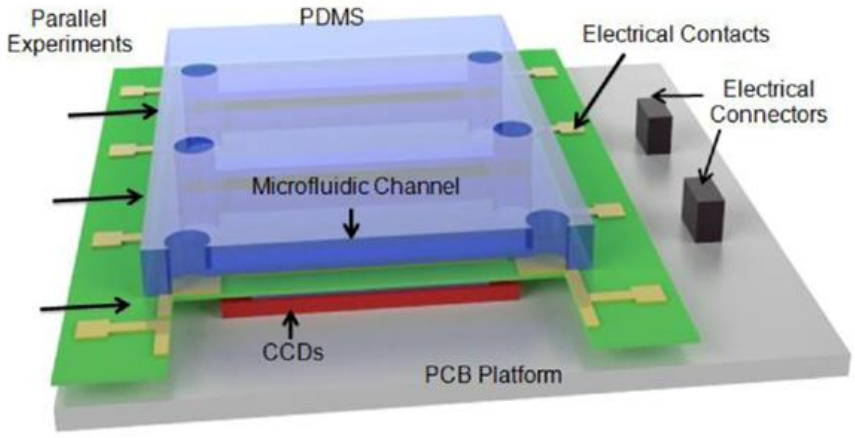

Figure 1-3: Schematic of the microfluidic biofilm observation, analysis, and treatment (Micro-BOAT) platform. The platform is capable of performing six experiments in parallel on a single chip. Real-time biofilm monitoring is achieved via the measurement of biofilm optical density (OD) using CCDs and a tuned light emitting diode (LED) source (not shown) [73]. Reproduced with permission from [73].

1.3.2.2. Mechanical Biofilm Characterization

Microsystems that utilize the inherent mechanical properties of the device to measure the mass loading onto the device surface have also been developed for accurate biofilm sensing in real-time. These microsystems typically employ a thin-film piezoelectric material, which can provide an electrical response corresponding to the amount of mass loading. The most commonly researched mass loading sensors include the quartz crystal microbalance (QCM), quartz tuning fork oscillators, and surface acoustic wave (SAW) sensors.

The QCM is a sensitive technique used extensively to study the solid-liquid interface. QCM measurements are based on a shift of the quartz crystal's resonant frequency due to interactions

with solution components [74]. QCMs have also been used to study and characterize biofilm growth and removal in real-time. Reipa et al. used the QCM in conjunction with optical techniques to monitor the long-term (6 days) growth of biofilms in a reactor [75]. The authors utilized a parameter, the ratio of change in resistance to change in frequency that reflects changes in the viscoelastic properties of the biofilm, to monitor its growth in low nutrient environments in real-time. In parallel, the optical technique of white light reflectance off the surface of the QCM gold electrode was used to determine the biofilm thickness. Similarly, Castro et al. used a QCM to analyze the viscoelastic properties of *Staphylococcus epidermidis* and *Escherichia coli*, identifying an increase in shear modulus as a distinctive characteristic in biofilm formation [76].

QCMs have been combined with dissipation monitoring, known as QCM-D, to continuously monitor *in situ* bacterial cell attachment and growth of biofilms [77]. Using this method, Schofield et al. showed that biofilms formed under continuous flow had greater biomass and were more viscoelastic, or softer, than biofilms that were seeded without flow and grown with flow. The energy losses represented by the increases in the dissipative factor (D) indicated an increase in 'softness' of the attached cells. Additionally, the ratio of the dissipative factor to frequency or D/f was used to provide information on how viscoelasticity changed per unit mass. These studies allowed not only for the detection of biofilm monitoring during the various stages of growth and treatment with antibiotics or antibacterial agents, but also the continuous monitoring of the properties of cells while establishing that flow conditions over cells on the surface are important in creating biofilms with greater complexity and stability. More recently, this technique has been used to assess cell-surface interactions as well [78]. Marcus et al. combined this technology with a fluorescent microscope and camera to monitor kinetics of cell adhesion over time. Two different surfaces, silica (SiO_2) and polyvinylidene fluoride, which are hydrophilic and

hydrophobic, respectively, were used to test the role of surface wettability on biofilm formation [78]. Olsson et al. studied the adhesion of a series of *Streptococcus salivarius* mutants, each possessing various surface appendages of known lengths, as a function of time using QCM-D. The experimental results were used to further understand and interpret the frequency change and dissipation signal due to the complex interactions within the 250 nm between the substratum and the bacterial cell surface [79]. The same group also showed that while only bacterial attachment to the QCM shifts the frequency in the positive direction, ECM-generating strains of bacteria that form biofilms elicit a frequency shift in the negative direction [80].

Waszczuk et al. developed disposable piezoelectric quartz tuning fork mass sensors to evaluate bacterial biofilm growth [81]. The authors demonstrate the use of this low frequency quartz tuning fork sensor to detect the dynamics of the various phases of *Pseudomonas aeruginosa* biofilm. Unlike QCMs, the effective mass of molecules adhering to a quartz tuning fork surface is not equal to real mass and is only a fraction of the real mass. However, the real mass of bacterial biofilm grown on the tuning fork can be estimated using the tuning fork resonant frequency shift. The authors thus validate the use of the tuning fork as a crystal oscillator, which experiences a change in frequency due to the change in mass resulting from biofilm growth on the sensing area. The same group demonstrate the use of quartz tuning forks to detect the viscosity and density of biofilms and report the development of a quartz tuning fork ring-down system, based on the modulated excitation signal technique to provide the quartz tuning fork excitation, for detecting the formation of *Pseudomonas aeruginosa* biofilm *in situ* [82]. The authors calibrate the quartz tuning fork ring-down system by measuring oscillation results in reference liquids so that unknown densities and viscosities could be determined. This system was also used to successfully measure

viscosity of the biofilm when subjected to different concentrations of the antibiotic ciprofloxacin at distinct incubation times.

SAW devices are an alternative platform to the QCM and quartz tuning fork, with the advantages of easier integration into array systems, simpler miniaturization, and significantly increased sensitivity due to the surface-guided nature of the mechanical wave and a higher operating frequency [83]–[85]. Berkenpas et al. developed a shear horizontal SAW device with stable temperature control and high frequency phase measurements for bacterial detection [86]. *Escherichia coli* were cultured and applied to the antibody-coated sensing surfaces, and the transmission coefficient phase of the biosensor was monitored continuously using a network analyzer. Sensitive real-time detection of biofilm growth was also demonstrated using a SAW sensor that is integrated with the BE treatment system [87], [88]. A schematic of the SAW sensor integrated with electrodes for the BE treatment application is shown in Figure 1-4. Real-time detection of biofilms is achieved by measuring the resonant frequency shift of the SAW system, which is a function of the total biomass adhered to the surface of the sensor and the change in viscoelasticity. As both biofilm growth and BE treatment cause a change in the adhered biomass, they can be measured in real-time by monitoring the resonant frequency of the system. While the described mechanical systems feature high sensitivity to mass loading, these sensors are constrained by the required piezoelectric materials that limit the viability of integration with indwelling medical devices.

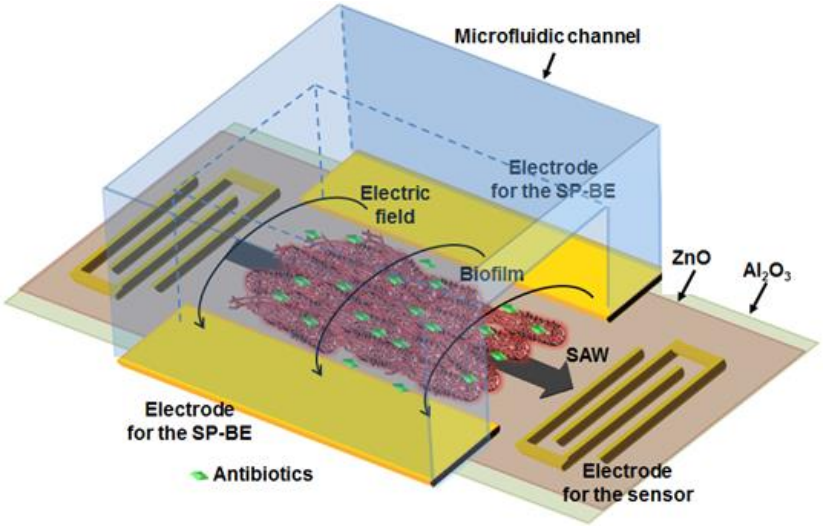

Figure 1-4: Schematic of a SAW sensor passivated with Al_2O_3 and integrated with BE treatment capabilities [87]. Reproduced with permission from [87].

1.3.2.3. Electrochemical Biofilm Characterization

Electrochemical biosensors are a well-studied class of sensors and are the first widely successfully commercialized biosensors [89], [90]. These are broadly divided into two categories according to the operating principle governing their method of measurement: impedimetric/non-faradaic and faradaic (potentiometric, amperometric) transducers.

Impedimetric Microsystems: Impedance based techniques have been used as a method of transduction for detecting and quantifying bacteria. Specifically, impedance microbiology (IM) has been used for decades to detect the presence of microorganisms in samples in the food industry, environment, and health care [91], [92]. In IM, the change in impedance is measured using a pair of electrodes that is submerged in the culture medium. To detect bacterial growth in real-time, the relative or absolute change in conductance, impedance, or capacitance of the solution are measured at a given temperature. While classical impedance microbiology uses either direct or indirect measurement techniques for measuring the impedance change of the media, several studies have found that the total impedance change during bacterial growth consists of two components that

can be measured at different frequency ranges: (i) impedance change contributed by the media and (ii) impedance change contributed by the electrode/electrolyte interface, also known as the electrochemical double layer (EDL) impedance. This electrochemical impedance measurement is generally a non-faradaic process that does not involve charge transfer at the electrode surface, which contrasts with the faradaic – amperometric or potentiometric – approaches discussed in the next subsection. The EDL impedance dominates at lower frequencies (typically < 10 kHz) while the growth medium impedance becomes more dominant at frequencies above 10 kHz. A simple equivalent circuit model, in which a resistor, R_s, is in series with two EDL capacitors, each of value C_{dl}, can be used to understand the frequency dependence of both elements on the overall impedance. The impedance (Z) of the circuit can be mathematically expressed as equation (1.3.1) below:

$$|Z| = \sqrt{{R_s}^2 + \left(\frac{1}{\pi f C_{dl}}\right)^2} \qquad (1.3.1)$$

where f is the frequency, R_s is the solution resistance, and C_{dl} is the EDL capacitance at the electrodes.

Similarly, IDEs – a conventional two-electrode system configuration at miniaturized scales – have been used for sensing biological samples via impedance and require smaller sample volumes while providing a higher signal to noise ratio, faster reaction kinetics, and faster attainment of a steady-state relative to other microelectrode approaches, along with a relatively low power requirement [59], [93]–[96]. The equivalent circuit model, mathematically expressed in (2.1), remains valid for the case of the IDEs. However, the frequency ranges over which the EDL capacitance and the solution resistance are dominant may change with the electrode spacing and width. Yang et al. demonstrated the use of IDEs for sensing bacterial growth; specifically, the

growth induced a 30% change in the EDL capacitance with almost no change in the solution resistance (-0.58%) [95]. IDE-based systems can be advantageous over conventional electrode systems in that the IDEs can measure the change in the EDL capacitance to monitor bacterial growth.

In biofilms, both the cells and the ECM within the biofilm serve as dielectric materials and thereby are responsible for its electrochemical impedance that varies with the time, composition, or metabolic state of the biofilm. Hence, bacterial biofilms grown on the surface of microelectrodes can be modeled as an electrical circuit. One such equivalent electrical model is presented in Figure 1-5 (a)-(c). Figure 1-5 (a) presents the electrical model of a sterile culturing media that does not contain any bacteria. Figure 1-5 (b)-(c) presents a simplified series and equivalent parallel electrical model for when biofilm and ECM grow between the two electrodes. In the circuit, the parameters represent the following: C_{dl} is the EDL capacitance, R_{sol} is the resistance of the media without bacterial cells, and C_{bio} and R_{bio} are the capacitance and resistance of the biofilm, respectively. The ideal circuit model for a given situation can be determined by comparing these models to experimental results. When bacterial metabolism causes a change in the first two parameters, the impedimetric response of the culture changes proportionally [97].

The magnitude of the impedance of the three electrical circuits shown in Figure 1-5 can be calculated using equations (1.3.2), (1.3.3), and (1.3.4) listed below. Paredes et al. calculated the numerical values of the various parameters by fitting these equations to experimental data obtained for *Staphylococcus epidermis* biofilms [97].

$$Z_{(a)} = R_{sol} + \frac{2}{j\omega C_{dl}} \qquad (1.3.2)$$

$$Z_{(b)} = R_{sol} + R_{bio} + \frac{2}{j\omega C_{dl}} + \frac{1}{j\omega C_{bio}} \qquad (1.3.3)$$

$$Z_{(c)} = \frac{R_{sol}\,R_{bio}}{R_{sol} + j\omega R_{sol} R_{bio} C_{dl} + R_{bio}} + \frac{2}{j\omega C_{dl}} \qquad (1.3.4)$$

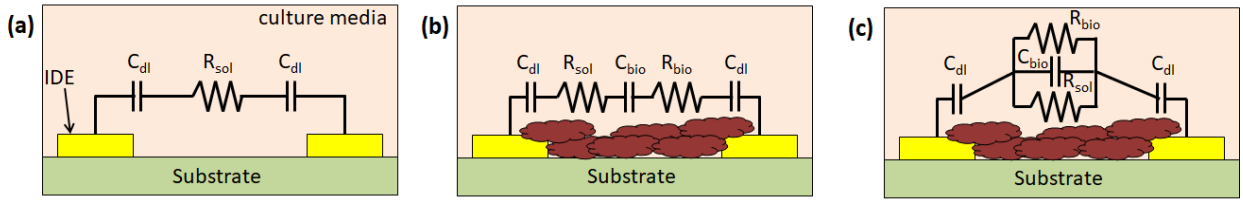

Figure 1-5: Cross-section schematic of electrical circuit model of a pair of electrodes. (a) Circuit model for sterile culture media before inoculation with bacterial cells. Equivalent (b) series and (c) parallel circuit models after biofilm and ECM formation [13].

By fitting these or other equivalent models to the experimental data, specific electrical parameters of the system can be tracked and used to accurately sense the onset of biofilm growth as well as the growth over time. For example, Liu et al. utilized an IDE based impedance sensor and an equivalent circuit model to track changes in the resistance and capacitance of *Escherichia coli* and *Salmonella* biofilms over time [98].

Impedimetric techniques have emerged as one of the most common methods for biofilm detection and characterization [92], [99]–[101]. Stöckl et al. employed a three-electrode setup, which separates reference and counter electrodes for a more stable electrode system than the two-electrode approach for impedance measurements, to determine the bacterial adhesion properties of *Shewanella oneidensis* biofilms using electrochemical impedance spectroscopy (EIS) [102]. EIS involves measuring the impedance of a sample over a range of frequencies to gain a greater understanding of the resistive and capacitive characteristics of the sample. The flow cell and

electrode setup developed by Stöckl et al. allows parallel confocal laser scanning microscopy in addition to EIS for biofilm characterization.

A microfluidic multi-channel device based on the principles of bifurcation has been developed that allows for spatial segmentation of biofilms with the ability to perform multiple experiments on the same chip (Figure 1-6) [16]. The sensor-treatment system is comprised of IDE electrodes that detect biofilms using traditional impedance measurements and performs treatment using the BE. In studies performed with this device, the BE treatment was applied based on the state of the biofilm, accessed by comparing the measured impedance values with a user-set impedance change threshold. Thus, this system allowed for continuous real-time monitoring of biofilm growth, while simultaneously being programmed to administer treatment when necessary.

More sophisticated impedimetric systems, with capabilities to monitor more than one parameter simultaneously, have also been reported. Bruchmann et al. reported a multi-parametric sensor, that uses both non-faradaic (EIS) and faradaic (amperometric current) measurements (discussed in the following subsection) within a multi-channel microfluidic platform to measure biofilm formation and activity, respectively [103]. Here, gold IDEs or circular electrodes were used to detect *Stenotrophomonas maltophilia* and *Pseudomonas aueruginosa* biofilms as well as complex mixed population biofilm formation, exoenzymatic activity, and their responses to disinfectant and anti-biofilm reagents, thus making this sensor a qualified tool for assessing biofilm formation in specific environments. However, a large experimental variation between biofilms was observed. Similarly, the sensor developed by Estrada-Leypon et al. used multiple sets of electrodes not only to detect biofilm formation and activity, but also to measure dissolved oxygen, Na^+, K^+, and pH levels within the biofilm [104]. This was achieved by using two sets of IDEs along with punctual electrodes. Carminati et al. utilized an impedimetric microsensor for measuring biofilm

formation along with sensors for pH, conductivity, and temperature for pipe water quality monitoring [105]. Furthermore, Tubia et al. demonstrated that IDE-based impedimetric sensors functionalized with antibodies could be utilized for detecting specific biofilm, in this case *Brettanomyces bruxellensis* [106].

Potentiometric and Amperometric Microsystems: Faradaic electrochemical techniques including potentiometric and amperometric methods have also been employed for real-time biofilm sensing. These types of measurements allow monitoring of faradaic current, generated by the reduction and oxidation of a redox species in contact with a solid electrode. It has been shown that during the first steps of bacterial adhesion, there is a charge transfer between the cells and the substrate [107], [108]. Bacterial cells generate a variety of molecules (e.g. pyocyanin, phenazine-1-carboxylic acid, etc.) that possess electrochemically active groups that can react with the free electrons of the surface. Electrochemical techniques enable tracking of this behavior, making it possible to study them, and hence, detect bacterial presence at the initial stages of adhesion and biofilm formation.

Becerro et al. achieved this by developing a thin-film sensor that was designed for cyclic voltammetry (CV) and differential pulse voltammetry (DPV) measurements [109]. The authors use a four-microelectrode configuration, which comprises two gold working electrodes along with a platinum counter electrode and a platinum pseudo-reference electrode. This configuration provided higher sensitivity, a lower ohmic drop, and faster achievement of a steady-state current than a two-electrode configuration [110], [111]. *Staphylococcus epidermidis* biofilm presence was detected within two hours after initial inoculation using CV and one hour after with DPV. An increase in both the current signal and the three recorded redox peaks were observed proportionally to biofilm growth. Additionally, the CV and DPV measurements yielded information about the

specific stage of growth of the biofilm, indicated by different oxidation and reduction peaks, along with shifts in the overall current value. Similarly, Fysun et al. used CV and square-wave voltammetry to assess *Paenibacillus polymyxa* attachment [112].

Other researchers use electrochemical sensing to spatially monitor the chemical distribution in biofilms, which can help characterize the biochemical processes and regulation involved in cellular community development. Bellin et al. used an electrochemical camera chip capable of simultaneous spatial imaging of multiple redox-active phenazine metabolites, which are associated with biofilm activity and colonization via square wave voltammetry [113]. The chip consists of multiplexed electrodes that enable potential-sweep-based electrochemical imaging of whole *Pseudomonas aeruginosa* biofilms. Using both wild-type and mutant biofilms, the authors were able to confirm the spatial location of different phenazine metabolites. Additionally, this method lends itself to detecting unanticipated compounds.

Thus, electrochemical biosensors are a promising class of microsystems that lend themselves to miniaturization, require low power, and are extremely sensitive to small changes in the environment. These advantages make this class of sensors a serious candidate for real-time biofilm detection in medical devices or other systems. None of the systems described, however, have been implemented in a urinary catheter environment for *in situ* monitoring of biofilm formation.

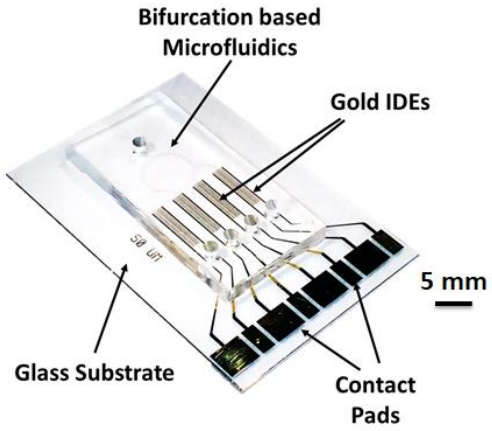

Figure 1-6: Photograph of the multi-channel microfluidic device with IDEs for biofilm sensing and treatment using the BE [16]. Adapted with permission from [16]. Copyright 2017 American Chemical Society.

1.3.3 Catheter-associated urinary tract infection (CAUTI) & CAUTI management

CAUTI is one of the most prevalent nosocomial infections, accounting for over 25,000 cases in United States' hospitals in 2018, according to the CDC [1]. In addition, the healthcare costs of CAUTI were estimated to be around $450 million in the United States in 2007 [114]. CAUTI is driven by the colonization of the catheter by bacterial biofilms [115]. An indwelling urinary catheter is initially coated with a conditioning layer of host proteins from the urine which promote bacterial adhesion [10]. Bacteria can attach and begin to colonize the catheter during catheter insertion or by migrating along the inner lumen or catheter-urethra interface [116]. These bacteria are often fecal contaminants or part of the skin microbiome, but they can also originate with the healthcare providers [10]. Once attached, the bacteria grow and form a protective biofilm, depicted in Figure 1-7 [10]. CAUTI can lead to severe complications such as blockages, bacteremia, sepsis, pyelonephritis, and mortality [117]–[119].

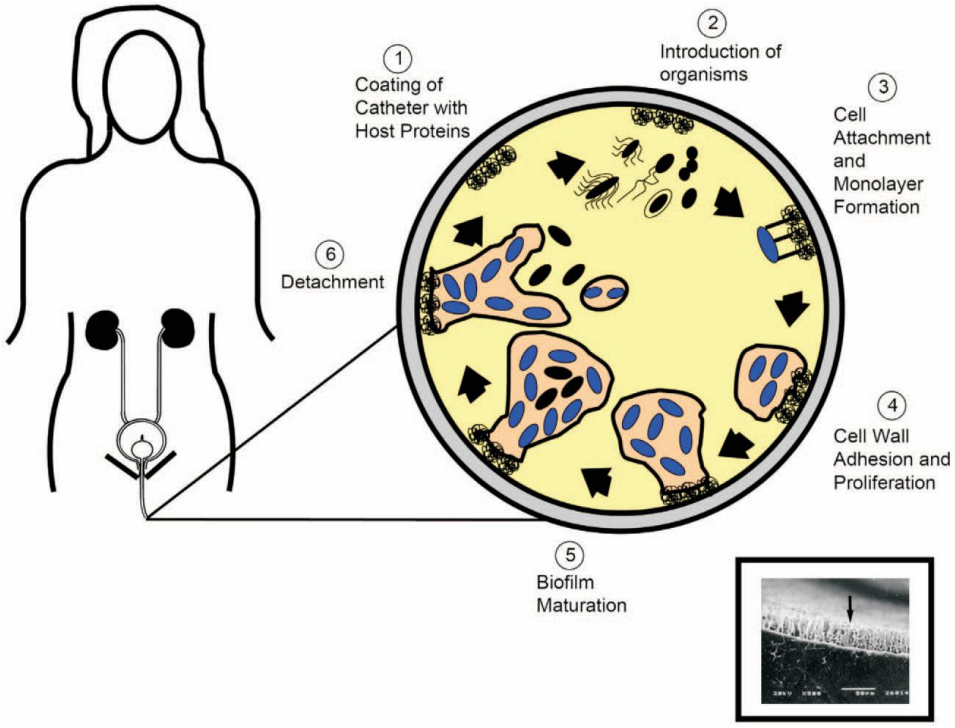

Figure 1-7: Biofilm development process in urinary catheters [10]. Reproduced with permission from [10].

Guidelines issued by the CDC recommend that indwelling urinary catheters not be changed at routine intervals, but rather based on clinical indications, such as infection or obstruction [9]. However, many clinical indications, such as conventional bacterial cultures, take hours or days to identify potential infections [120]. Furthermore, healthcare practitioners typically wait for symptoms of an infection, such as fever, pain, or dysuria, to develop before ordering cultures [5]. This time can allow infections to progress significantly; identification of infection risk (i.e. biofilm colonization), leading to prompt catheter removal or treatment, is important for CAUTI management. However, it is important to note that not all catheter biofilms lead to CAUTI [25].

Numerous strategies have been explored to reduce the incidence of CAUTI by modifying the surfaces of indwelling catheters. The catheter surface can be made to kill adherent bacteria by displaying or eluting antimicrobial molecules. Notably, chemical surface modifications such as impregnation with antiseptics, antibiotics, or metal ions have shown some efficacy in research but

have revealed inconsistent results in clinical practice [121], [122]. Furthermore, antibiotic-infused catheters are not desirable, as widespread antibiotic use increases the risk of selection for antibiotic resistance [5]. Catheter surfaces can also be modified to interfere with bacterial cells' ability to adhere. Notably, microscale topography, designed to mimic shark's skin, has been shown to reduce bacterial attachment and delay biofilm formation [123]. Similarly, liquid-infused surfaces have been shown to reduce the degree of biofilm formation on catheter-like materials [124]. Despite widespread efforts to mitigate the challenges associated with CAUTI, it remains a large-scale problem, demanding new and innovative approaches for effective management.

1.3.4 Catheter-integrated microsystems

An overarching theme in this thesis is the integration of microsystems with a urinary catheter to achieve effective biofilm management. An array of different microsystems have been integrated with catheters. However, none allow monitoring and treatment on urinary catheters for CAUTI mitigation. Microscale pressure sensors were one of the first microsystems integrated with catheters [125]. These were incorporated onto the tip of a vascular catheter to measure pressure in the heart. Other systems integrated with vascular catheters include flow sensors [126], glucose sensors [127], and magnetic actuators for biofouling removal [128]. Many sensors have been adapted for use on urinary catheters as well. Patents have been published describing incontinence [129], temperature [130], [131], and pressure [132] sensors integrated with urinary catheters. Temperature sensor-integrated Foley catheters, in particular, are currently commercially available and have achieved clinical use [133]. Other research groups have integrated pH-sensitive materials with urinary catheters to enable colorimetric detection of *Proteus mirabilis* infection [134]–[136]. In one variation of this approach, a catheter is coated in a pH-sensitive polymer that degrades when the pH rises above a threshold and releases an indicator dye [134]. While this may work for *Proteus*

mirabilis, this fails to account for the broad range of organisms associated with the majority of CAUTIs [116], [137]. To the best of my knowledge, no previous work integrates a more general biofilm or bacterial growth sensor with a urinary catheter. In addition, such a sensing approach has not been combined with BE treatment in this application to form a dynamic biofilm monitoring and removal system.

1.4 Structure of Dissertation

The first chapter of this dissertation has focused on the background and motivation for this work, introducing the challenge of CAUTI and a microsystems-based approach for addressing it. The second chapter describes the development and testing of a proof-of-concept flexible device for both impedance-based sensing and BE treatment of biofilm in a cylindrical catheter-like environment. Chapter three focuses on systems integration to incorporate the sensing and treatment functionalities with a standard, commercially available Foley catheter. Chapter four discusses the performance of the integrated system in a realistic bladder model. Finally, the key contributions of my dissertation are summarized, and the future directions of this work are given in chapter five.

Chapter 2: Impedimetric Sensing and Bioelectric Effect Treatment of Biofilm in a Cylindrical Environment

The first step in developing a microsystem-based approach for managing CAUTI is adapting existing LOC systems for use in geometrically complex environments, particularly the cylindrical geometry of the lumen of a urinary catheter. I relied upon the planar impedance-based sensor system that also incorporates BE-based biofilm treatment developed previously in our group [16], [41]. This design had to be adapted to a substrate that is conformable to the cylindrical surface but is also compatible with the fabrication techniques required for the IDE design. Furthermore, the device must maintain its sensing and treatment functionality when placed in the catheter-scale cylindrical environment. In this chapter, I produce a proof-of-concept device for biofilm monitoring and treatment in urinary catheters. First, I develop a fabrication process for IDEs on a flexible substrate that enables seamless conformation of the electrodes with geometrically complex surfaces. Then, I demonstrate that these electrodes can detect the growth of *Escherichia coli* biofilm in real-time via impedimetric sensing. These same electrodes are also shown to be capable of administering the electric field needed for the BE treatment of the biofilm. Lastly, the impact of varying curvature on device performance is also examined experimentally and using commercial modelling software.

I gratefully acknowledge Dr. Luke Beardslee for his help developing this fabrication process. I also must acknowledge Sam Preza for his help performing the COMSOL modeling.

2.1 Flexible Sensor for Impedimetric Biofilm Sensing on Complex Surfaces

Sensor systems fabricated on flexible substrates have drawn significant interest in recent years due to their potential for enabling integration in a diverse array of applications. Flexible

substrates allow devices to conform seamlessly and operate on complex 3D surfaces without interfering with the function of the target system. Highly deformable biocompatible polymeric substrates are specifically of interest for wearable or implantable devices. Thin polyimide films have been utilized extensively to fabricate conformal humidity sensors [138], tactile strain sensors [139], transistors [140], neural probes [141], etcetera, as it is robust with regards to fabrication as well as being highly flexible and biocompatible [142]. Parylene-C films have also served as flexible substrates, particularly for implantable probes or wearable devices [143], [144]. Elastomers, including PDMS, are also popular. PDMS fabrication is highly robust and flexible, enabling a wide range of potential devices and applications. Examples include wearable pulse sensors [145], electrochemical sensors [146], or stretchable circuit components [147]. Flexible substrates have also been interfaced with off-the-shelf electronic components [144]. The breadth of flexible substrates that have been utilized in recent years provides a diverse array of options when approaching the multidimensional surfaces susceptible to biofilm formation regarding fabrication, chemical and biological compatibility, and integration.

In this section, I describe a flexible impedance sensor capable of detecting biofilm formation in a cylindrical setting, specifically in the interior lumen of a catheter. The device is comprised of gold IDEs fabricated on a flexible polyimide film, allowing the electrodes to conform to the cylindrical inner surface of the catheter to sense biofilm in real-time. The highly flexible nature of the thin polyimide film encourages facile integration with the cylindrical architecture of the catheter lumen, and it is both biologically inert and compatible with microfabrication processes [142]. The platform was characterized in a custom flow system consisting of a catheter tube integrated with the device on which biofilm was grown. I characterized the impedance sensor response *in vitro* using a benchtop potentiostat. Both the end-point and real-time impedance

characteristics provide a clear picture of the viability of this device for continuous monitoring of the catheter surface with regard to biofilm colonization. CVS correlates the impedance change with the biofilm biomass to corroborate the relationship between biofilm growth and flexible sensor response.

2.1.1 Materials and methods

The electrodes were patterned on the polyimide substrate using a standard photolithography process. A 25.4 µm thick Kapton HD polyimide film (McMaster-Carr) was affixed to the surface of a 4-inch silicon wafer via heat-release tape (Semiconductor Equipment Corp.). A photolithography step with a positive photoresist (PR) (Shipley 1813 resist, Microchem) defined the IDE geometry on the polyimide substrate using the transparency photomask depicted in Figure 6-1 in Appendix A. Each patterned polyimide substrate was then exposed to oxygen plasma for 1 minute at 200 W immediately prior to metal deposition to improve adhesion (Branson). 20/200 nm of chromium/gold was deposited on the wafer via e-beam evaporation (Angstrom Engineering), with the chromium serving as an adhesion layer. Electrode fabrication was completed via a lift-off step in acetone for 1 minute. The electrode patterned polyimide substrate was removed from the wafer by heating to 150 °C on a hot plate, prompting release by the tape. The fabrication process is depicted in Figure 2-1. Each device consisted of gold IDEs with width and spacing of 300 µm over a 10 mm × 40 mm footprint, connected to 30 mm-long gold leads. The device schematic is shown in Figure 2-2 (a), along with a photograph of the actual device integrated with 18 Fr intermittent catheter tubing in Figure 2-2 (b).

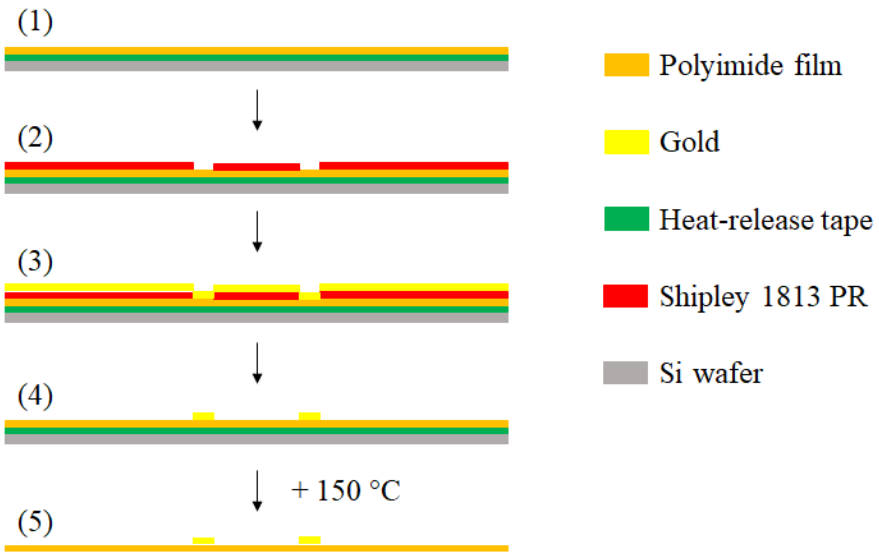

Figure 2-1: Fabrication process flow: (1) adhere polyimide film to wafer, (2) pattern PR, (3) metal deposition, (4) lift-off, and (5) release from tape at 150°C [148]. © 2018 IEEE

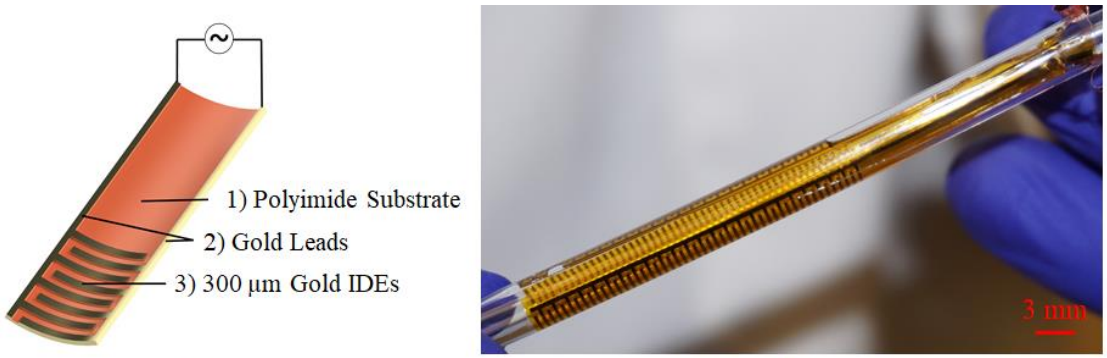

Figure 2-2: (a) A schematic of the flexible platform showing 1) the flexible 25.4 µm polyimide substrate, 2) gold leads for interfacing the sensor with a potentiostat, and 3) gold IDEs with 300 µm width and spacing over a 10 × 40 mm^2 footprint. (b) An optical image of the device interfaced with the interior lumen of the catheter tube (inner diameter of 4.5 mm). The device is seamlessly integrated onto the curved surface with no signs of degradation, highlighting the advantage of the flexible platform [148]. © 2018 IEEE

This proof-of-concept system was tested in a custom-designed flow system, depicted in Figure 2-3. This flow system consisted of two 500 ml flasks, with one serving as a media reservoir and the other as a waste container. The flasks were connected to an 11 cm section of 18 Fr

intermittent catheter tubing (Allegro Medical) with the sensor adhered. The flasks were sealed with rubber stoppers, with two holes for fluidic connections. Uncured PDMS (Dow-Corning) mixed at a 10:1 ratio of base to curing agent was coated on the interior of the catheter tube by introducing a large drop at the inlet and spreading it over the entire surface with a wooden applicator rod. The flexible device was introduced while the surface was coated in uncured PDMS. Throughout the process of adhering the device to the inner surface of the catheter, the tube was held in a vertical position to ensure any excess PDMS would flow away from the IDEs. Then, the PDMS was cured for 3 hours at 60 °C to fix the polyimide substrate in place. Once cured, fluidic connections were assembled with tygon tubing and luer connectors (Cole-Parmer), interfacing the sensor and catheter section with the media and waste reservoirs. The media container was filled with 500 ml of Lysogeny broth (LB) media (Sigma). The catheter/sensor system, tubing, and both reservoirs were autoclaved for 40 min at 121 °C for sterilization. The components were then connected in a sterile biosafety cabinet to prevent contamination. The outer diameter of the tubing and the inner diameter of the catheter tube are such that the connection is friction sealed. The electrical connections were made by sandwiching aluminum foil strips in between the contact pads and the tygon tubing. The friction seal helped to hold the foil contact in place and isolate it from the solution being flowed. The foil extended beyond the catheter tube on the outside of the tygon tubing, where it could interface with the potentiostat via alligator clips. Following assembly, pure LB media was introduced throughout the flow system for conditioning to remove air pockets. An air break was included to prevent bacteria traveling from the catheter into the sterile media reservoir. The reservoirs were connected to 0.2 µm syringe filters (VWR) to equalize the pressure during flow and maintain sterility. Flow was driven by a syringe pump (Cole Parmer, 74900) in

withdrawal mode at 7 ml/h. The sensor/catheter system was maintained at 37 °C in a closed incubator, to simulate an inserted catheter.

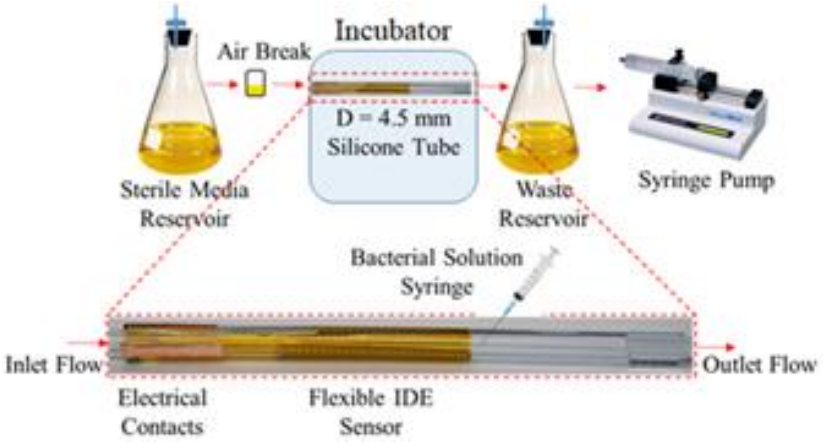

Figure 2-3: Custom flow system setup for testing in situ biofilm detection and BE treatment in a catheter model [148]. © 2018 IEEE

Prior to each experiment, *Escherichia coli* K-12 W3110, a wild-type strain exhibiting a biofilm-forming phenotype, were incubated in 5 ml of LB media for 20 hours at 37 °C in an Innova 4000 incubator shaker (New Brunswick Scientific) set to 250 rpm. The bacterial solution was then diluted to an $OD_{600\ nm}$ of 0.25 (corresponding to 6×10^7 CFU/ml). 1 ml of the diluted bacterial suspension was injected directly into the flow system connected to the catheter-sensor flow system. Bacteria were allowed to attach to the catheter and sensor surface for 2 hours under static (no flow) conditions, constituting the 'seeding' phase. Following seeding, fresh LB media was flowed through the system at 7 ml/h for 24 hours, constituting the 'growth' phase. Time-lapse images of biofilm growth were acquired using a digital camera (Sony Alpha 6000) at 0, 6, 12, and 24-hour time intervals. Throughout the experiment, impedance data were collected via a potentiostat (model 660D, CHInstruments) running through a previously-developed MATLAB-based graphical user interface [16]. In order to evaluate this device as a real-time monitoring tool, the impedance at 100 Hz was measured every 2.25 minutes. The impedance spectra from 10 Hz to 10^6

Hz at 50 mV was determined at four different phases of the growth experiments: conditioning with media before the addition of bacteria, seeding, 5 hours into growth, and 24 hours into growth. These were plotted using the Matlab (Mathworks) program in Appendix B.1. This allowed characterization of the impedance response due to biofilm growth. The impedance spectra could be compared to the equivalent circuit models in section 1.3.2.3 to identify the specific parameters driving the sensor response using the Matlab program in Appendix B.2. The relative percentage change in impedance was calculated and compared between an unseeded control and a biofilm sample using (2.1), where Z is the system impedance at the time of measurement and $Z_{initial}$ is the impedance at t = 0. One-way analysis of variance (One-way ANOVA) was performed to evaluate the significance of the changes in impedance.

$$\%\ change\ in\ Z = (Z - Z_{initial})/Z_{initial} \times 100 \qquad (2.1)$$

2.1.2 Flexible biofilm impedance sensor characterization

Impedance spectra were obtained and compared at four sequential phases during the biofilm growth process. The average impedance spectra are shown in Figure 2-4 (a)-(b), and the percentage change at each phase relative to the initial impedance measured during the conditioning phase is shown in Figure 2-4 (c)-(d) for 10 Hz, 100 Hz, 1 kHz, 10 kHz, and 100 kHz. The control sample in Figure 2-4 (a) was characterized by a relatively uniform increase in impedance across all frequencies, with a small positive shift apparent after 5 hours and a more significant shift after 24 hours. By contrast, samples with biofilm in Figure 2-4 (b) were characterized by decreases in impedance at lower frequencies, particularly below 5 kHz. The change was negligible after 5 hours of growth. However, after 24 hours of growth, a mature biofilm had formed, and the impedance spectrum had shifted at lower frequencies. The control showed an increase in impedance of 20-30% at each of the representative frequencies at the end of the 24 hours period (Figure 2-4 (c)).

This increase was irrespective of frequency and was attributed to the formation of small bubbles near the sensor surface due to the permeability of the silicone to air, which allowed air to diffuse through the tube walls. In addition, the media reservoir was being maintained at room temperature, and bubbles in the LB media experienced thermal expansion when they flowed into the catheter at 37 °C. The formation of small bubbles was further encouraged by the negative pressure created in the tube used to drive the LB media flow. This encouraged bubbles to expand with air from outside the tube. After 24 h of biofilm growth, there was a decrease in impedance of 5-20% at 1 kHz and below (Figure 2-4 (d)). Overall, the spectra showed significant differences in relative change in impedance with 24 hours of biofilm formation (Figure 2-4 (d)) compared to the bacteria free control (Figure 2-4 (c)) at 10 Hz ($p = 0.1901$), 100 Hz ($p = 0.0947$), 1 kHz ($p = 0.0553$), 10 kHz ($p = 0.0020$), and 100 kHz ($p = 0.0715$). Overall, this result suggests that the frequency-dependent decrease arises as the biofilm alters the capacitive components of the circuit, which are dominant at lower frequencies.

When comparing the experimental results to the equivalent circuit model equations 1.3.3 and 1.3.4, it becomes apparent that the series model (1.3.3) of biofilm formation is more appropriate in this case. For this model, at higher frequency, the capacitive terms disappear. This leads to a plateaued value approximately equal to the sum of the biofilm resistance and solution resistance at higher frequency (> 20 kHz region) and an exponential increase with decreasing frequency at lower frequency (< 20 kHz region). A representative impedance spectrum measured at the end of the seeding period was compared to the series equivalent circuit model 1.3.3, regarding the impedance of the sensor before significant biofilm formation (Figure 2-5 (a)). Figure 2-5 (b) depicts an experimentally determined impedance spectrum from the same device after 24 hours of biofilm growth, compared to the model 1.3.3. This model includes the resistance of the

bulk solution (R_{Sol}), the resistance of biofilm formed on the surface (R_{bio}), the interfacial capacitance (C_{dl}), and the capacitance of the biofilm on the surface (C_{bio}). The empirically determined circuit parameters for each time point are shown in table 2.1. This confirms that an increase in capacitance associated with the biofilm helped drive the impedance decrease in the lower frequency range (< 10 kHz) that was seen in Figure 2-4. This is consistent with previous works showing that increased capacitance from adhered biofilm and increased double-layer capacitance arising from biofilm metabolism contributes to decreased impedance [15], [149]. This conclusion could be further evaluated experimentally by examining the impedance shift with certain elements removed, such as mutant bacteria, which do not attach and produce biofilm.

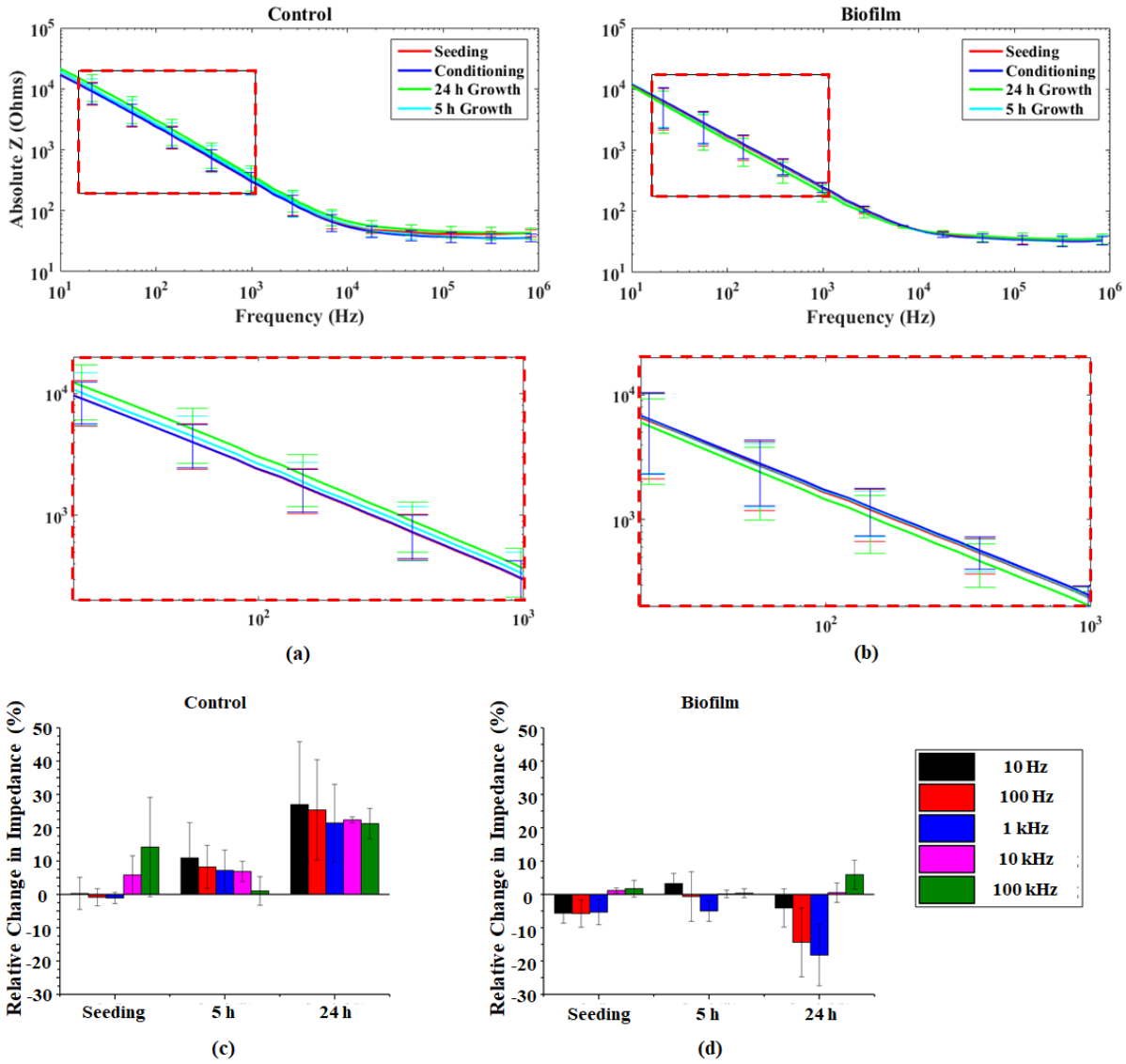

Figure 2-4: 50 mV impedance spectra at different intervals throughout biofilm growth experiments, (a) without biofilm (control) and (b) with biofilm formation. The dotted boxes (expanded below) highlight the region from 20 Hz to 1 kHz to emphasize the differing responses. Relative percent change in impedance at 5 representative frequencies (c) without biofilm (control) and (d) with biofilm formation. Control samples showed a uniform increase in impedance compared to a distinct frequency-dependent decrease in impedance with biofilm formation (N = 3) [148]. © 2018 IEEE

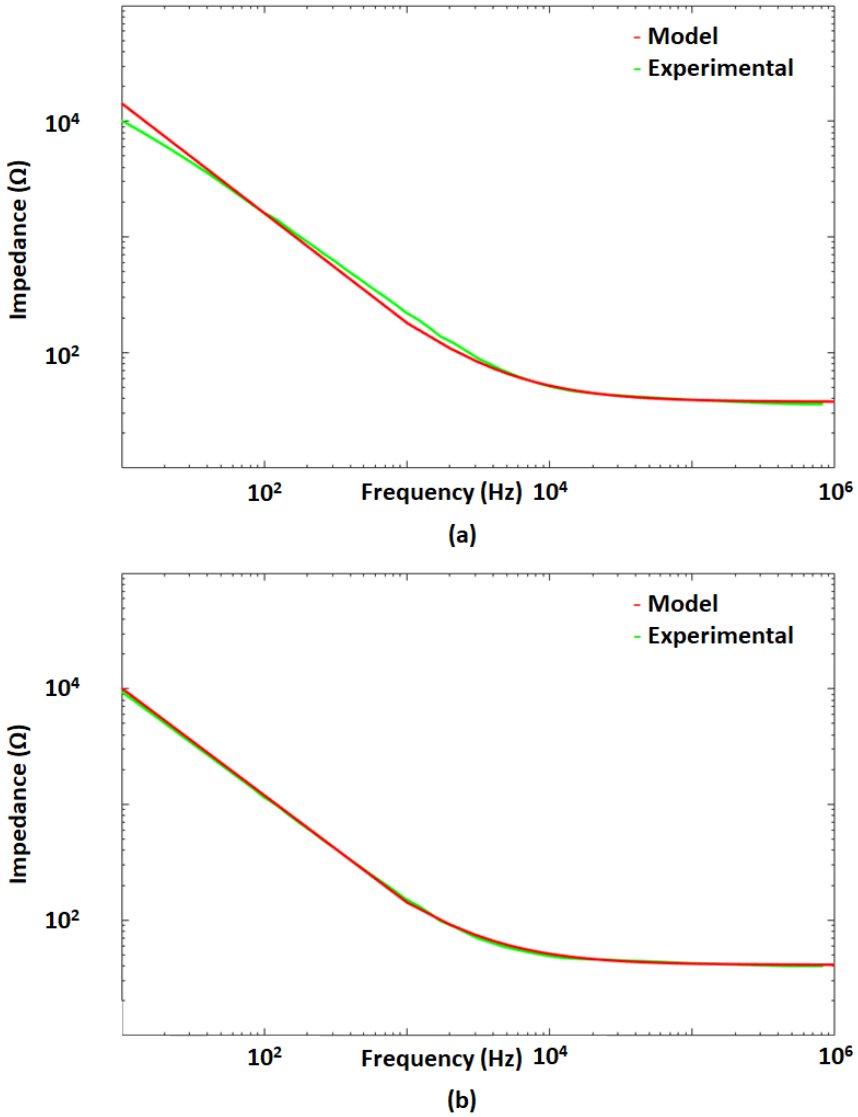

Figure 2-5: Theoretical models fit to match experimentally determined impedance spectra (a) before (t = 0) and (b) after (t = 24 h) biofilm formation. The empirically determined circuit parameters for each fit are shown in table 2.1.

Parameter	**t = 0**	**t = 24**
R_{sol} (Ω)	37.0	37.0
R_{bio} (Ω)	0.5	4.0
C_{dl} (μF)	18	18

C_{bio} (μF)	8	12

Table 2-1: Circuit parameters for biofilm sensing impedance spectra.

Furthermore, the real-time sensing capabilities of this flexible system were demonstrated, representing a significant advantage over present biofilm analysis techniques. To do so, the impedance at 100 Hz was tracked over the 24 hours growth period continuously to evaluate the real-time degree of biofilm formation. 100 Hz was selected as it showed highest sensitivity within the frequency range investigated, as shown in Figure 2-4 (d). The 100 Hz samples showed the largest change between the biofilm and the unseeded control in the impedance spectra. The percentage change in impedance over time, relative to the initial value, was calculated and compared for devices with and without biofilm formation. When bacteria were introduced into the device, biofilm formed on the surface and drove a decrease in the system impedance. The time-lapse images in Figure 2-6 (a), along with their corresponding impedance sensor signals in Figure 2-6 (b), indicate a correlation between this drop in impedance and the rapid expansion of the biofilm colony. The biofilm can be seen in the red boxes in Figure 2-6 (a), growing in a layer on the side of the catheter tube. The start of the growth phase at t = 0 ((i) in Figure 2-6) shows no biofilm and an impedance of 2.72 kΩ. An initial layer appears after 6 hours ((ii) in Figure 2-6), showing only a slight decrease in impedance relative to the impedance at t = 0. After 12 hours ((iii) in Figure 2-6) a thin layer of biofilm is visible, accompanied by a distinct drop in the impedance. The impedance decreases to 2.58 kΩ after 24 hours ((iv) in Figure 2-6) with a thick, mature biofilm present.

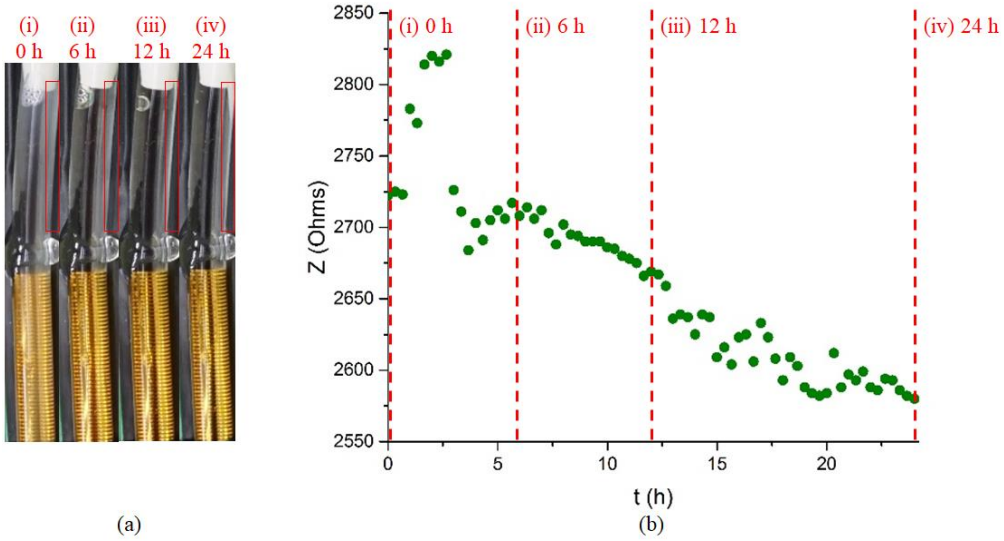

Figure 2-6: (a) Time lapse images of platform in catheter tube, with the device in orange and the biofilm forming as a white streak along the edge of the tube in the red boxed region. (b) Impedance transient with lines indicating the impedance at each image. The initial spike in impedance is attributed to a small air pocket being flushed out of the tubing and then passing over part of the sensor [148]. © 2018 IEEE

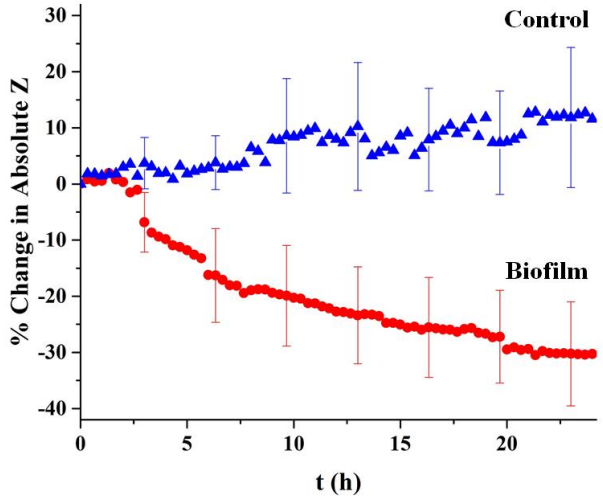

Figure 2-7: Average real-time impedance sensing results over the course of the 24-hour growth period, measured by the benchtop potentiostat. The blue triangles correspond to the control samples (without biofilm formation) and the red circles correspond to the samples with biofilm formation. The excitation

signal used was AC 50 mV at 100 Hz, chosen to optimize sensitivity. The error bars correspond to standard error (N = 5) [18].

The unseeded control, which has no bacteria to form a biofilm, showed a slight increase in impedance over the duration of the experiments (Figure 2-7). As described previously, this is attributed to the formation of small air bubbles on the sensor surface. Conversely, when bacteria are introduced into the tube, a biofilm forms, leading to a dramatic 30.3% decrease in the impedance (Figure 2-7) after 24 hours of growth. Similar to the above images, biofilm does not grow uniformly. On average, the impedance drops precipitously as the biofilm matures from the initial colonization to the rapid proliferation phase. The impedance decreases an average of 6.8% over the first three hours. However, there is a reduction in the rate of impedance decrease after this initial drop, as mature biofilms form and growth decelerates; from hour 3 to 24 the impedance decreases approximately 1% per hour. This result is consistent with the proliferation of biofilm after initial attachment (seeding phase), followed by a mature biofilm that may disperse bacteria throughout the system [150]. The shedding of planktonic cells could help contribute to the sensor signal plateauing by offsetting any continued growth [28], [29]. The lower rate of impedance decrease during the later portion of the growth phase could also be attributed to signal saturation, with additional biofilm growth beyond the range of the electrodes.

The end-point biomass determined via CVS can be compared between samples with and without biofilm in this system after 48 hours, and the trend can be compared with the impedance sensing results. The biomass quantification results are shown in Figure 2-10 in the next section (2.2). The absorbance nearly doubled on average in samples with biofilm (sensing only) compared to the biofilm-free unseeded controls. The control signal represents the contribution from the LB media alone. The increased absorbance associated with biofilm was statistically significant according to one-way ANOVA ($p < 0.05$), confirming the increase in biomass. Furthermore, this

increase in biomass is correlated with the decrease in impedance, measured with the flexible sensor. This corroborates the suggestion that biofilm growth drives a decrease in impedance in real-time with this flexible device.

2.2 Bioelectric Effect Treatment in a Cylindrical Environment Utilizing Flexible Sensor Electrodes

In addition to biofilm detection during growth, I demonstrate removal of biofilm using the BE with this flexible device in a cylindrical environment, which reduces the concentration of antibiotics required for biofilm elimination. The BE is comprised of a low-intensity electric field combined with a low concentration of an antimicrobial compound to achieve synergistic biofilm removal. For this setup, the same electric field introduced for impedance sensing was utilized to administer BE treatment. This allows the flexible proof-of-concept device to significantly reduce the medical burden of the infection without excessive antibiotic use. Following 24 hours of growth, as described in the previous section, the BE treatment is administered on mature biofilms. The efficacy of this approach for biofilm removal is evaluated using end-point CVS biomass quantification. In addition, the impedance sensor capabilities can also be used to monitor the decrease in biofilm on the device surface in real-time. It is invaluable to develop approaches such as this to provide techniques for removing biofilms on devices, in addition to identifying them in real-time.

2.2.1 Materials and methods

The flexible device used in 2.1 was also used to administer the electric field needed for the BE. These tests were done using the same setup described in Figure 2-3, and the treatments were applied after the conclusion of the 24 hour growth period. Five samples were compared to evaluate sensing and BE efficacy: 1) Unseeded, 2) Sensing-only, 3) BE treatment, 4) Antibiotic-only, and

5) Untreated. The unseeded samples did not have any bacteria added and did have the 50 mV, 100 Hz sensing signal. The Sensing-only sample was exposed to the 50 mV sensing signal over the duration of the experiment. BE treatment consisted of the sensing signal, with the gentamicin diluted in the LB media reservoir to a concentration of 10 µg/ml for the treatment phase. The Antibiotic-only samples did not have the impedance sensing voltage but did have 10 µg/ml gentamicin present during the 20-hour treatment period. An untreated control was seeded with bacteria but has neither the voltage associated with sensing nor the antibiotic. Only biomass quantification using CVS was performed for untreated samples; no impedance sensing was performed on these samples. The relative change in impedance was recorded as a percentage change relative to the initial impedance using (1). End-point CVS was performed at the end of the treatment period. The biofilm biomass following the completion of the growth phase was quantified using a CVS absorbance assay. CVS binds to the extracellular proteins and DNA associated with biofilm formation [151], [152]. CVS solution was prepared by adding 50 µg of CVS powder (Fisher Scientific) to 10 ml of deionized water. To perform the CVS assay, the catheter tube with the sensor was disconnected from the flow system, and one end was sealed with a 3-way stopcock. The tube was drained to remove media and non-adherent cells. The stopcock was sealed, and the tube was positioned vertically with the open end directed upward. The tube was then filled via pipette with 1 ml of the 0.0005% weight percentage CVS solution for 15 minutes. The CVS solution was then drained from the tube, and both the tube and sensor were gently rinsed 4 times with 1x PBS to remove unbound CVS stain. Following this, the tube was filled with 1 ml of decomplexation solution (4:1 ethanol to acetone) for 30 minutes. CVS is soluble in the decomplexation solution, so the CVS bound to the biofilm dissolved in the solution and could be measured using OD. Finally, the solution in the tube was drained into a cuvette, and the

biomass was quantified via OD measurements at 590 nm using a UV (ultraviolet)-visible spectrum spectrophotometer (SpectraMAX). 590 nm was selected as the wavelength with the highest absorbance of crystal violet. One-way ANOVA was performed to evaluate the significance of the biomass quantification results. The impedance was recorded continuously, as described in 2.1, for real-time biofilm monitoring. The experimental conditions and timing are summarized in Figure 2-8.

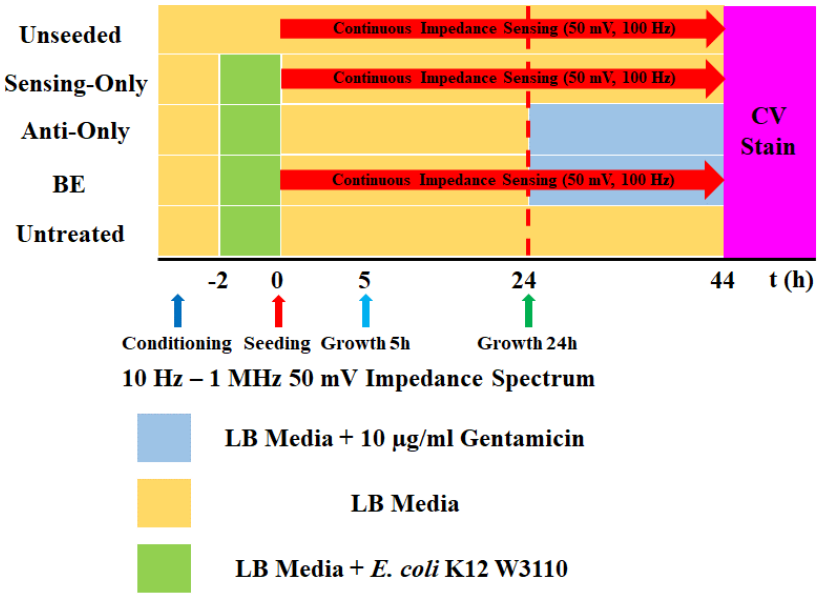

Figure 2-8: Experimental conditions and timing showing when treatments were applied and when data was collected. Colored arrows correspond to EIS sweeps [148]. © 2018 IEEE

2.2.2 Characterization of BE in a cylindrical environment

Following the formation of a mature biofilm during the 24-hour growth period, the flexible electrode system was used to apply a BE-based treatment to achieve synergistic biofilm removal. This 50 mV signal maintained a similar electric field strength compared to our previous work where the BE was implemented successfully in a microfluidic device [16]. The combined real-time impedance transients for both the growth and treatment periods are shown in Figure 2-9. The treatment portion of this plot was set to begin at 24 hours, with the subsequent change in absolute

impedance determined relative to the impedance at 24 hours and offset to the change in impedance for samples with or without biofilm during the growth period. The BE and (sensing-only) biofilm treatment transients start at the same point, as this is the average impedance for a 24 hour-old biofilm, which is then subjected to either the sensing signal or the sensing signal plus gentamicin (BE). The 50 mV signal alone (Sensing-Only, Biofilm) showed a 1% decrease in impedance during the treatment period relative to the impedance at the end of the 24-hour growth phase, indicative of negligible change in biofilm. However, when the synergistic BE treatment was applied, the sensor measured a 12% increase in impedance relative to the initial impedance of the mature biofilm at the start of the treatment phase/end of the growth phase. This suggests effective removal of the biofilm via the BE which has led to an increase in impedance because the film was no longer able to adhere strongly to the surface or accumulate ions after treatment.

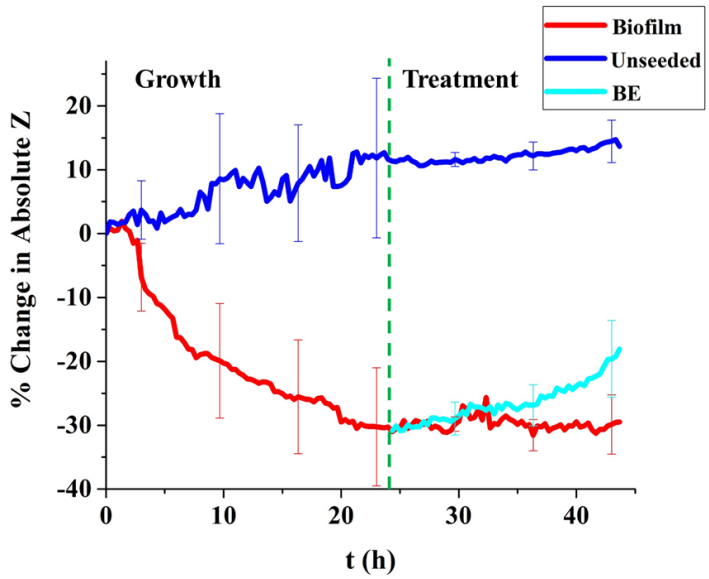

Figure 2-9: Growth (left): Percentage change in 50 mV impedance at 100 Hz for biofilm (sensing-only, red) and unseeded (blue) samples over a 24 hours growth period showing an initial drop followed by slowed growth. The large standard error indicates the high inherent variability of biofilm formation (N = 5). Treatment (right): Percent change in 50 mV 100 Hz impedance over the course of a 20-hour treatment period on a mature biofilm (i.e. relative to the impedance at the end of the growth phase). Removal of

biofilm via the BE led to a 12% increase in impedance compared with the 1% decrease for the sensing-only samples (N = 3) [148].

A CVS absorbance assay was performed to quantify the amount of strongly adhered biofilm material on the surface of the tube following the treatment period (Figure 2-10). The untreated control, without the sensing signal or antibiotics, presented an average absorbance of 0.385±0.106. This decreased to 0.159±0.021 for the BE treatment group, similar to the 0.143±0.023 absorbance found with the unseeded control. The absorbance for the untreated control is attributed to the adsorption of macromolecules from the LB media onto the surface. The antibiotic-only group showed an absorbance of 0.377±0.028, while the sensing-only group had an absorbance of 0.263±0.036. The small decrease for the sensing-only group suggests that the electric field may contribute in reducing biofilm slightly. BE treatment yielded a significant decrease in biomass compared to the antibiotic-only sample (ANOVA $p < 0.05$). This data also indicates a distinct trend, showing the decrease in biomass from untreated or sensing-only samples to BE treatment (ANOVA $p = 0.1054$ and $p = 0.0663$, respectively). The unseeded control absorbance corresponded to the signal attributed to the presence of pure LB media. The similar absorbance after 24 hours of BE treatment indicated there was a negligible amount of adhered biomass remaining in the tube. The unseeded samples displayed significantly less biomass when compared with the sensing-only ($p = 0.04693$), antibiotic-only ($p = 0.00287$), or untreated ($p = 0.08976$) groups. There appeared to be less biomass than the controls with the electric field or antibiotic alone, highlighting the synergistic effect of the treatment. Previous work suggests that the electrical energy of the sensing signal allows either an increase in the permeability of the bacterial cell membrane, enhanced diffusion of the charged antibiotic, or both [153]. This serves to explain the increased efficacy of antibiotics in reducing biofilm in the presence of the electric field introduced by this flexible platform.

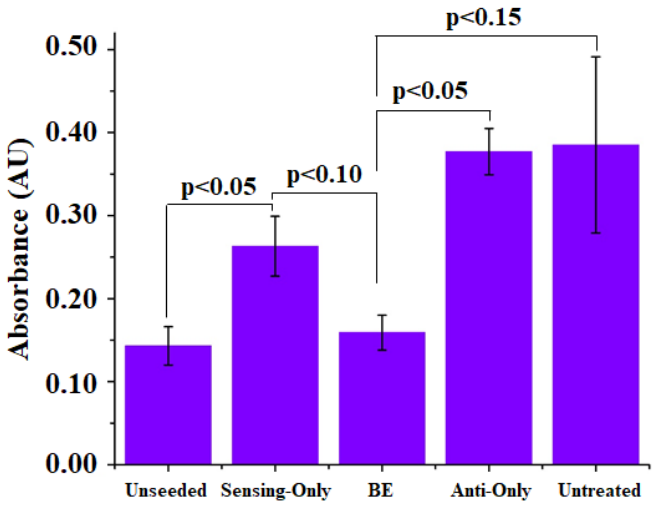

Figure 2-10: CVS to evaluate the biomass at the end of each of the five treatments, showing the decrease in biofilm due to the BE: Unseeded, Sensing-Only, Antibiotic (Anti)-Only, and Untreated, and the BE. (N=3) [148]. © 2018 IEEE

2.3 Impact of Curvature on Device Performance

An important factor to consider when adapting these devices from planar to cylindrical domains is how the sensing and treatment performance changes. The curved conformation of the electrodes can alter the electric field distribution and change the device functionality. I compare an electrode pair conformed in a catheter-scale cylinder to electrodes in a planar arrangement using a commercial FEA software. This approach allows a detailed study of sensitivity and saturation with regard to increasing biofilm thickness in each case. In addition to these simulations, I perform experiments conforming the flexible sensors designed in 2.1 to varying degrees of curvature relevant to biofilm formation. Performing biofilm detection and BE treatment experiments using this setup enables the identification of any significant deviations in device performance associated with curvature.

2.3.1 Materials and methods

2.3.1.1 FEA simulations

I utilized COMSOL Multiphysics 5.2 commercial FEA modeling software to create catheter-scale models of a single pair of electrodes in two different conformations, cylindrical and planar. The cylindrical model consisted of a 4.5 mm diameter and 2 mm long cylinder, with electrodes defined on the cylinder surface. The electrodes were defined on one side of a rectangular model for the planar conformation. The width of the rectangular model is the same as the circumference of the cylindrical model (14.1 mm), with the depth the same as the radius of the cylinder (2.25 mm), and the length 2 mm. The gold electrodes in each model had an arc length of 10 mm and a varying width of either 100 µm, 300 µm, or 500 µm. The spacing between the pair was also 100 µm, 300 µm, or 500 µm, respectively. These models are depicted in the results in Figure 2-14. From the outer surface of the cylinder to a depth varying from 0 to 0.5 mm, a layer of biofilm was defined. Biofilm was defined as a 10% dispersion of *Escherichia coli* cells in ECM via Maxwell's mixture theory [154], [155]. The apparent permittivity and conductivity of biofilm was determined using the permittivity and conductivity of ECM, cell membranes, and cytoplasm [156]–[158]. The remaining volume of the cylinder was defined with the electrical conductivity and permittivity of LB media [159]. This model for defining biofilm electrically was developed by Subramanian et al [16]. The 3D electrodynamic simulation determined the current density throughout the system based on an applied AC potential (50 mV, 100 Hz), which was used to determine the impedance based on the current across a probe surface separating the two electrodes. The surface area of the probe allowed the current to be determined, from which the impedance (Z) was calculated based on equation 2.2, where I is the complex current from the simulation and V is the applied voltage.

$$Z = V/I \quad (2.2)$$

The absolute impedance was determined as the magnitude of the complex impedance from equation 2.2 for each electrode width and spacing for biofilm thickness from 0 to 0.5 mm in 0.1 mm increments. These models allow the impact of conformation and electrode spacing on sensitivity to increasing biofilm thickness to be investigated through the relative change in absolute impedance. The absolute impedance is the same metric generated by the device in 2.1.

2.3.1.2 Variable curvature flow system

To test the impact of curvature on device performance, the sensors were conformed at specified curvatures and incorporated into flow systems. The flexible sensors were fabricated as described in section 2.1. The fabrication process for conforming the sensors at specific curvatures is shown in Figure 2-11. The device was conformed around a 3D-printed mold (Formlabs Form 2, clear resin) with the desired curvature and taped to a glass microscope slide. PDMS (10:1 base:curing agent, Dow Corning) was poured onto the molded device and cured for 3 hours at 60 °C to maintain the sensor at the specified shape. Three different molds were used: $r_{curvature}$ = 12.7 mm (curvature comparable to a 1 in pipe), $r_{curvature}$ = 2.25 mm (comparable to a 18 Fr intermittent catheter), and a planar control. The cross-sectional area of the molds was kept constant to ensure that the shear force was the same for each experiment. The mold was then removed and tygon tubing was added at the inlet and outlet to interface the curved electrodes with the flow system. Epoxy was used to seal the interface between the tygon tubing and molded device. The flexible sensor leads and contact pads extend beyond the PDMS-molded area and were exposed so that they can be interfaced with the potentiostat. Representative devices conformed in each of the three curvatures are depicted in Figure 2-12.

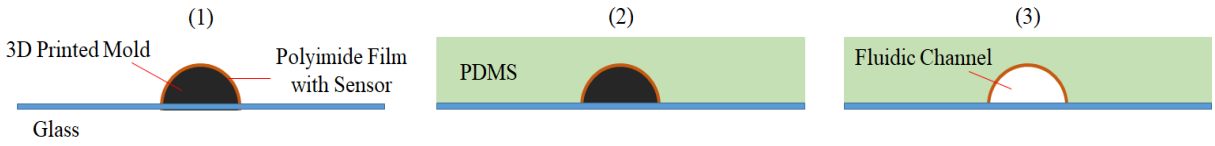

Figure 2-11: Fabrication process for microfluidic device with electrodes in a cylindrical conformation. (1) Polyimide film with sensor conformed around mold on glass. (2) PDMS was poured over sensor and mold. (3) Mold was removed, leaving the sensor in the appropriate curvature [160].

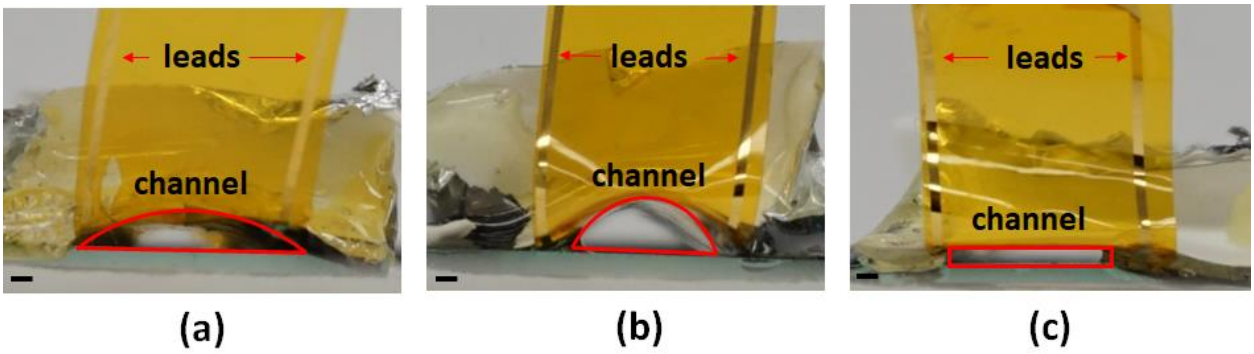

Figure 2-12: Flexible device conformed in (a) 1" water pipe configuration, (b) 18 Fr catheter curvature, and (c) planar configuration. Red outline delineates the fluidic channel with the same cross-sectional area around which the device is conformed. Scale bar 1 mm [160].

A flow system similar to the one used to evaluate the proof-of-concept device was used for examining the impact of curvature on device performance (Figure 2-13). A media reservoir was filled with 500 ml of LB media and interfaced with the curved device platform using tygon tubing. A peristaltic pump (Cole Parmer) was used to drive the flow. Tygon tubing from the outlet of the curved device platform connects to a waste flask. The curved device was contained within an incubator maintained at 37 °C.

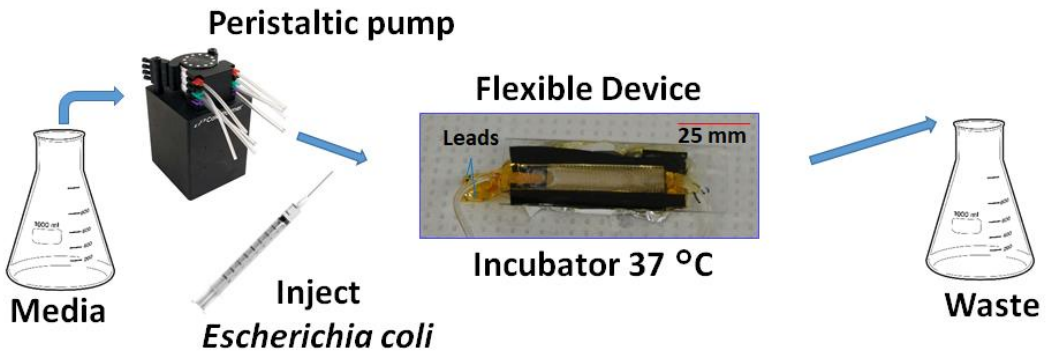

Figure 2-13: Experimental setup for growing and treating biofilm on curved device [160].

Escherichia coli were prepared to a concentration of OD_{600nm} = 0.25 in LB media as described in section 2.1.1. 1 ml of this preparation was introduced via the inlet tubing to the curved device and allowed to adhere for 2 hours (seeding). Seeding was followed by 24 hours of LB media flow at 3.5 ml/h (growth). Throughout the growth period, the impedance was recorded at 100 Hz (50 mV) using a potentiostat (Model 660D, CHInstruments) similar to the procedure described in section 2.1.1. After the conclusion of the growth period, gentamicin (Sigma) was added to the media reservoir to a concentration of 10 µg/ml and flow was continued for 24 hours (treatment). The antibiotic and sensor signal comprise the BE. Impedance spectra at 50 mV from 10-2000 Hz were recorded at the start of the treatment period and after 24 hours of exposure to the BE. This frequency range was selected based on the results from Figure 2-4 to be the most sensitive to biofilm formation. One-way ANOVA was performed to evaluate the significance of the changes in impedance.

2.3.2 Sensor curvature modeling

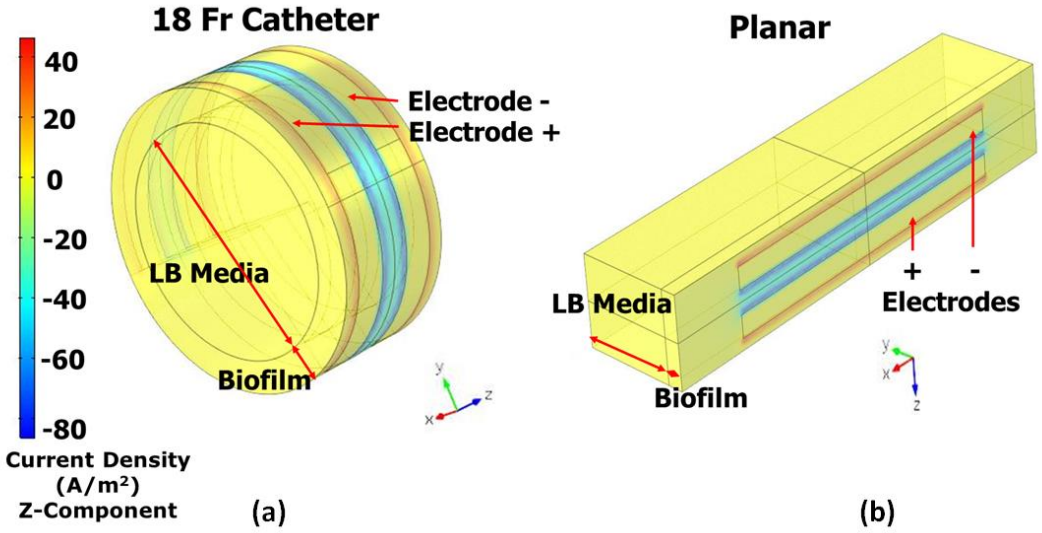

Figure 2-14: COMSOL electrodynamic simulations of electrodes with biofilm showing the resulting current density in (a) an 18 Fr catheter configuration and (b) in a planar configuration [160], [161].

The electrodynamic COMSOL simulations yielded the current density between two electrodes in a catheter-scale planar and curved domain. Representative 3D heat maps for each of these setups is depicted in Figure 2-14. These models clearly depict that the majority of the current is concentrated near the electrode surface. The measured impedance values in between the two electrodes were calculated based on the current density and applied voltage (50 mV), and the change in impedance with increasing biofilm thickness was determined. The relative change in impedance is shown in Figure 2-15. In each setting, the sensor response followed a similar pattern. The impedance increased with increasing biofilm thickness, approaching a 30% increase. The smallest electrode separation showed the largest change but also appeared to saturate quickly, showing little change after 0.2 mm of biofilm. By comparison, the widest electrode separation showed the smallest increase but did not appear to saturate at the higher thickness values. The 300 µm width/spacing proved to be an intermediate dimension, showing decreased saturation

compared to the 100 µm width/spacing and increased sensitivity compared to the 500 µm width/spacing. Notably, both the pattern and magnitude of the impedance change were very similar between the planar and cylindrical conformations. I attribute this to the fact that the radius of curvature is relatively large compared to the dimension of the electrodes and the resulting electric field distribution. The penetration depth of the electric field is expected to be comparable to the spacing of the electrodes [96]. In terms of sensor performance, this geometry appears effectively planar.

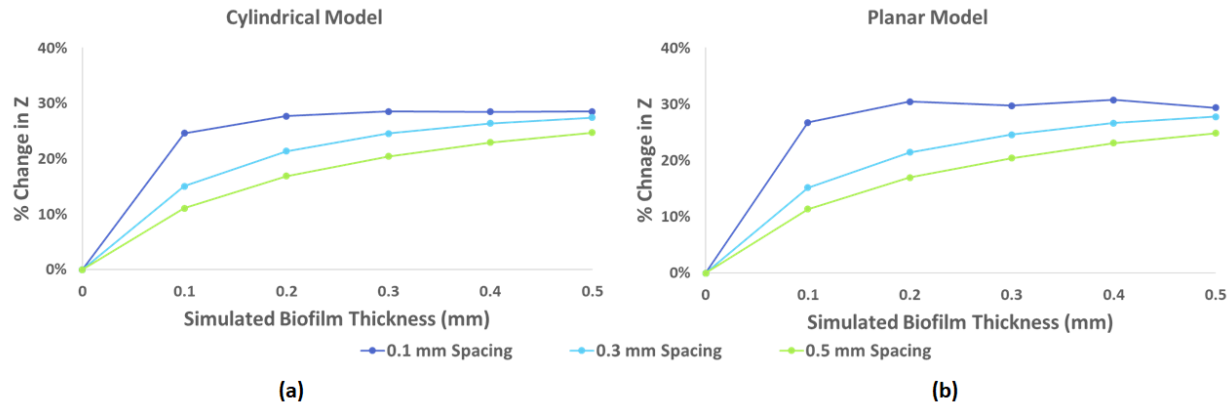

Figure 2-15: Current density yields relative change in impedance at 100 Hz as biofilm thickness increases above the electrode for the (a) cylindrical and (b) planar models [160], [161].

There are some notable weaknesses with this electrodynamic model for biofilm sensing. The impedance appeared to increase, directly contradicting the experimental results from section 2.2 indicating that a decrease in impedance is associated with biofilm growth. There are a number of factors contributing to this discrepancy. For one, this model only uses a single pair of parallel electrodes, as opposed to the IDE arrangement in the experiments. While this may impact the magnitude of the results, I would not expect this to produce the opposite trend. It is also important to note that biofilm is a highly complex material, and it does not grow in uniform layers. I would also not expect this to produce opposite results. Most importantly, this simulation models each

area as if it were a block of material with set dielectric properties. However, in reality these impedance sensors are electrochemical sensors that are responsive to the ions and molecules that are free to move and interact with the electrodes [162]. The LB media in the experimental setting contains numerous bacteria, while the simulation models the bulk solution as pure LB media with constant dielectric properties. In addition to the specified electrical properties of the cells and matrix, biofilm growth on the sensor surface is also associated with many charged molecules and metabolites that can impact the sensor [15]. Furthermore, the properties of biofilm and bacteria are dynamic, changing over time in different stages of development [109]. Regardless, this simulation still suggests that the cylindrical geometry does not significantly alter the current distribution. Thus, this simulation still supports the conclusion that cylindrical catheter-scale geometry does not impact biofilm sensor performance.

2.3.3 Experimental sensor curvature evaluation

Each of the three curvatures displayed a similar pattern during the growth period. The impedance decreased approximately 15% rapidly over the first 5 hours after the seeding period. The rate of decrease then slowed until it appeared to plateau. Based on the known characteristics of biofilm growth, this pattern seems to correspond to the rapid proliferation of bacteria and biofilm, followed by a mature biofilm phase [37], [109]. Importantly, the average relative 100 Hz impedance changes for the $r_{curvature}$ = 2.25 mm, $r_{curvature}$ = 12.7 mm, or the planar control at the end of the 24-hour growth period were not significantly different ($p > 0.05$). These impedance transients are displayed in Figure 2-16.

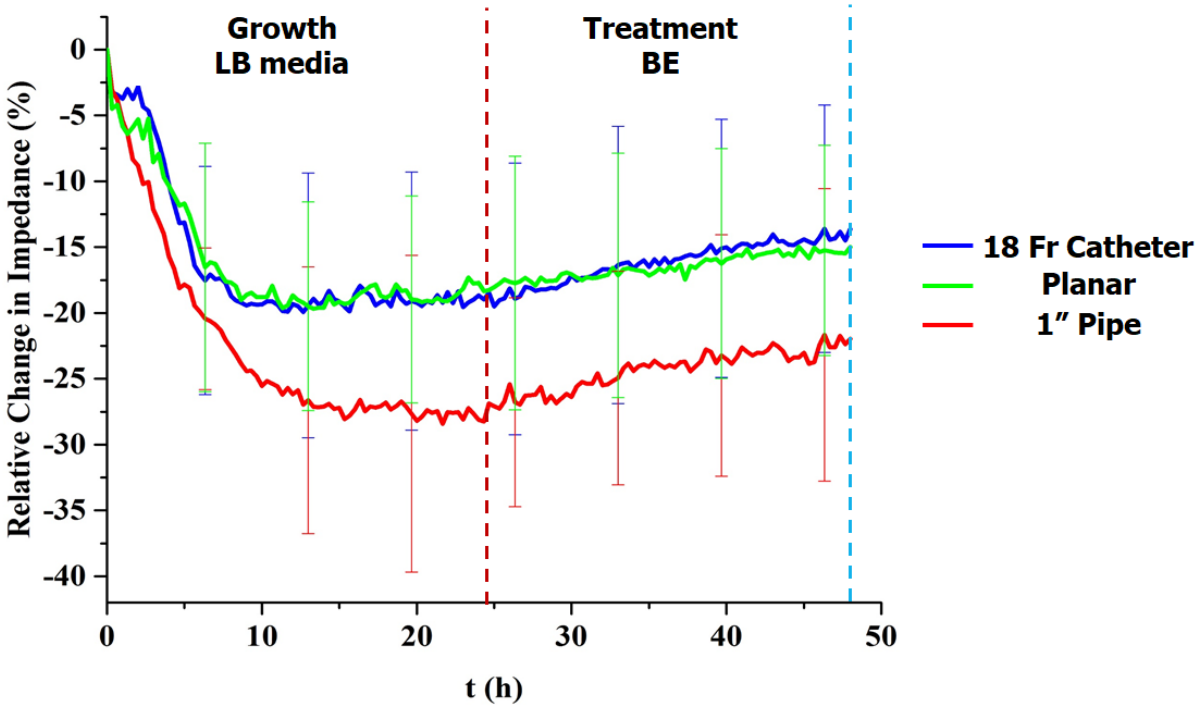

Figure 2-16: Temporal impedance response at 100 Hz showing similar decreases in impedance during the 24-hour growth phase, followed by similar increases in impedance during the subsequent treatment phase for 18 Fr curvature (blue), planar (green), and 1" pipe curvature (red). The error bars correspond to standard error (N = 3). Dashed lines correspond to when impedance spectra (Figure 2-17) were gathered following biofilm growth (red) and treatment (blue) [160].

The BE was also administered using this system, and the real-time relative impedance change was examined. In each case, the average impedance change increased steadily throughout the treatment period, suggesting that there was a biofilm removal effect with the application of the electric field and 10 µg/ml gentamicin. Likewise, the average change in impedance was not shown to be significantly different at the end of this period ($p > 0.05$). It is expected that the BE would function similarly since the electric field distribution did not appear to be altered dramatically between the planar and curved conformations. EIS at the beginning and end of the treatment periods shows a comparable increase in impedance following BE application for each of the conformations across the lower frequencies most sensitive to biofilm formation (Figure 2-17).

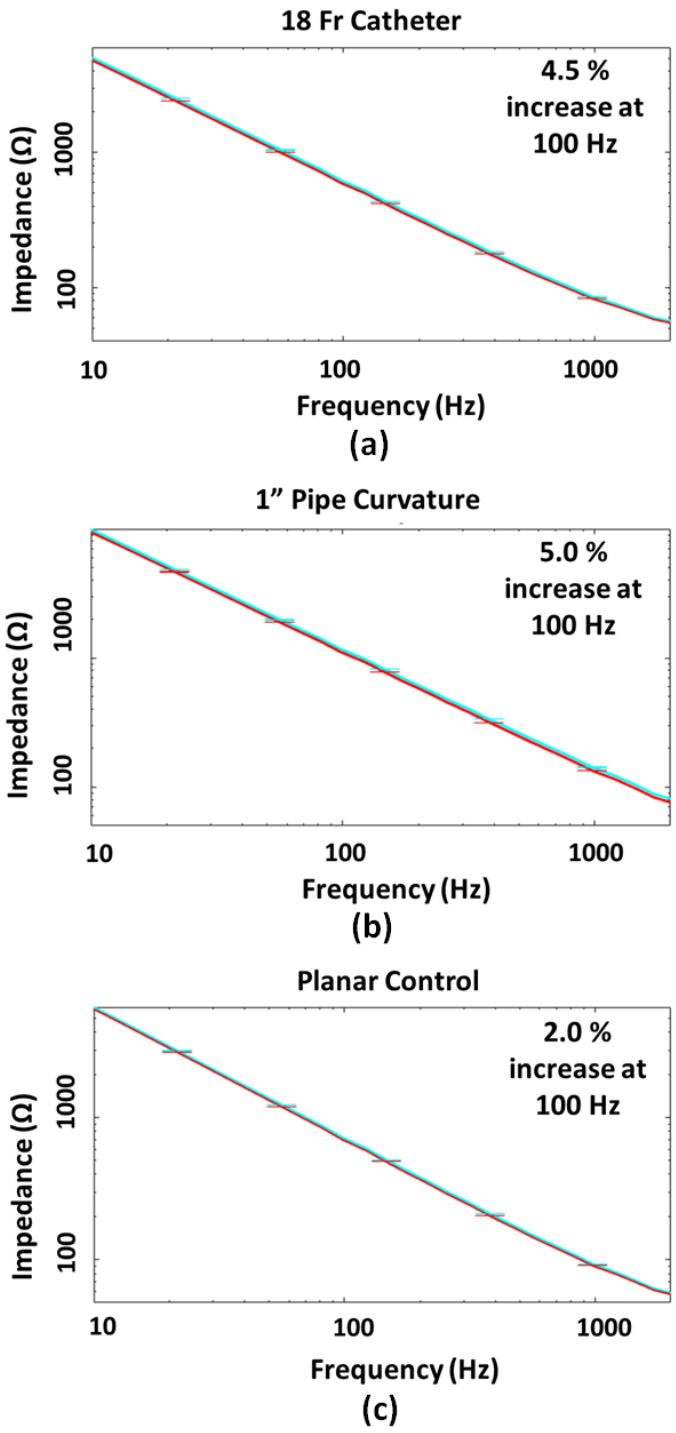

Figure 2-17: 10 Hz - 2 kHz impedance spectra at 50 mV for (a) 18 Fr catheter curvature, (b) 1" pipe curvature, and (c) planar control. The red corresponds to the impedance after the growth of a biofilm and the blue corresponds to the impedance after 24 hours of treatment. Each sample displays similar characteristics, increasing at low frequencies (N = 3 measurements on a single sample) [160].

In total, it appears that curvature at this scale produces no significant differences in flexible device functionality for both impedimetric detection and BE treatment. At this scale the electric field is concentrated at the surface, with similar current distributions in the planar and curved conformations. This similarity was identified using COMSOL commercial modelling software and confirmed experimentally with regard to both aspects of the device. This conclusion is significant, as it supports the use of this system in catheters, as well as other domains with complex surface geometry at this size scale.

2.4 Synopsis/Summary

In this chapter, I have presented a strategy for fabricating flexible electrodes to adapt LOC biofilm sensing and treatment systems for use in cylindrical domains where biofilms can lead infections, such as urinary catheters. I utilized this proof-of-concept device in a catheter-scale cylindrical conformation and demonstrated the capacity for real-time monitoring of biofilm growth via impedance sensing. This is the first step towards implementing novel microsystems approaches in CAUTI applications. I was also able to show that the same device could be used to apply the BE for biofilm elimination with reduced antibiotic use. The efficacy of this treatment in the cylindrical domain was supported by biomass staining and real-time impedance sensing. These key functions form the basis of the integrated sensing and treatment system for CAUTI management throughout the remainder of this thesis. I was also able to explore the impact that the cylindrical conformation may have on device performance. Both the commercial modelling software and experiments with precisely conformed sensors suggested that the device performance does not change notably in a cylindrical arrangement at the catheter size scale. This supports the use of this device for urinary catheter applications, but also other domains with non-planar geometry at this scale in the future.

Chapter 3: Foley Catheter-Integrated System

The proof-of-concept device developed in the previous chapter represents a potentially meaningful approach for addressing the challenges associated with biofilm formation. In order to realize the potential of this device for reducing CAUTI, it must be seamlessly integrated with existing catheters in a way that does not interfere with standard urinary catheter operation, including urine drainage and balloon anchoring. Furthermore, to achieve successful integration with current medical practices, this system must demonstrate biocompatibility with human tissue and allow users to adjust monitoring and treatment parameters in a user-friendly manner.

In this chapter, I explore two disparate electrode integration strategies. The first involves containing the flexible proof-of-concept impedance sensor, described in Chapter 2, within a 3D-printed insert, which can then be directly interfaced with the catheter. To further verify the viability of this approach for catheter integration, I examined the biocompatibility of the materials required. As an alternative strategy, electrodes were electroplated directly on the catheter surface. Finally, I describe the development and implementation of the microelectronics and mobile application needed for system control for CAUTI management. The results from this chapter comprise an integrated system with both sensing and treatment capabilities, as described in the previous chapter, incorporated with a commercially available Foley catheter.

I am very grateful for the help of Dr. Sangwook Chu with regard to the design and fabrication of the insert and the process flow for the *in situ* electrodes. Ashley Chapin provided support for the biocompatibility experiments. Dr. Luke Beardslee and Justin Stine provided invaluable help developing the electronic system. I also appreciate John Hadeed for building the mobile application.

3.1 3D-Printed Insert for Flexible Electrode Integration

This approach relies on a 3D-printed device-insert module to integrate the electrodes with a commercially available Foley catheter, depicted in Figure 3-1. The device-insert module is comprised of two channels that match the dual channels of the Foley catheter (Figure 3-1 (a)). The main channel mimics the dimensions of the urine drainage channel and houses the flexible device. The second channel is a groove that can contain a steel tube for the anchoring balloon inflation channel (Figure 3-1 (b)-(c)). In this manner, the device-insert module allows the essential functions of the urinary catheter to be maintained while adding the functionality of the flexible sensing and treatment electrodes. A transverse cut can be made in the catheter at any point along the main catheter body, and the insert module can be interfaced with each cut end, ensuring continuity for both channels.

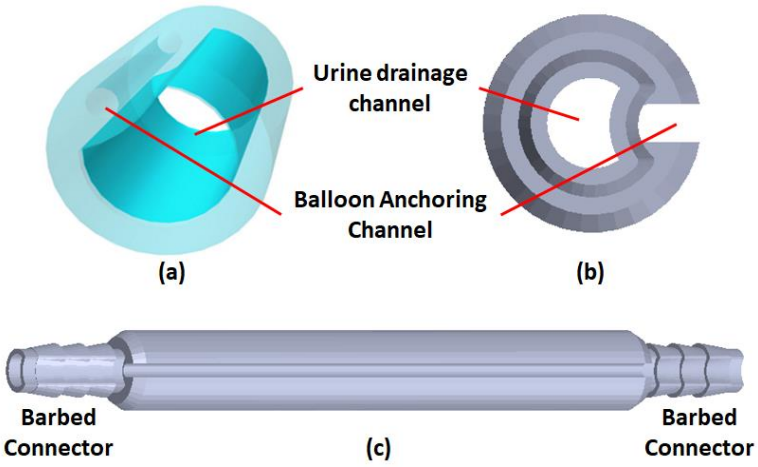

Figure 3-1: (a) Foley catheter cross section showing the urine drainage and balloon anchoring channels. (b) Cross section of insert showing channels corresponding to the two channels of the urinary catheter. (c) Schematic of insert module for housing the flexible device with barbed connectors for leak-free interfacing with a Foley catheter.

In this section, I introduce this integration approach in detail, confirming that each of the essential functionalities of the catheter are maintained after inserting the module. I also confirm

that the materials used are biocompatible per an ISO-10993-5 standard biocompatibility assay [163].

3.1.1 Materials and methods

3.1.1.1 Insert fabrication and integration

The device-insert module was 3D-printed using a Form 2 sterolithography (SLA) 3D printer (FormLabs) using standard clear resin [164]. As shown in Figure 3-2 (a), barb structures at the insert tips allowed a robust leak-free connection with the 22 Fr Foley catheter (Bard) urine channels, and a longitudinal groove along the outside wall accommodated a stainless-steel tube (McMaster-Carr) to connect the saline channel for balloon inflation. The flexible electrodes (20 nm Cr/200 nm Au) were fabricated on polyimide substrates (24 μm thick) via a standard electrode patterning microfabrication technique (lift-off, described in chapter 2), and the overall device footprint (48 mm x 10 mm) was adjusted via optical mask design (Figure 6-2 in Appendix A) to conform onto the inner lumen of the insert module without any overlap. Prior to being rolled into the module, electrical contact leads were established with 36-gauge wires (Calmont Wire and Cable, Inc) and copper tape (McMaster-Carr), followed by insulation with polyimide tape (McMaster-Carr). The wires ran along the inside of the catheter until exiting near the connection for the urine bag and were connected to the PCB.

The key catheter functions, urine drainage and balloon anchoring, were verified with the device-insert module integrated with the catheter and inserted into a 3D-printed silicone bladder model (Lazarus 3D). The bladder was filled with deionized (DI) water and drained continuously at a rate of 2.5 ml/min. The drainage function was confirmed as water was drained from the bladder via the insert-modified catheter for 4 hours. An additional bladder model customized to be printed with translucent silicone (Lazarus 3D) was used to confirm the balloon anchoring function. The

balloon was inflated after insertion with 1x phosphate-buffered saline solution with blue food dye for visualization.

3.1.1.2 Insert biocompatibility evaluation

Material cytotoxicity testing was performed following the ISO 10993-5 protocol [163]. This assay involved incubating materials with growth media for a set period. Cells were then exposed to the media to determine the impact of any potentially cytotoxic compounds that leached into the media. The cytotoxicity of two 3D-printable potential insert materials was examined: standard clear resin (Formlabs, Form 2) and MED610 (Stratasys, Objet500 Connex 3) [164], [165]. These materials were selected because they can be printed with sufficient resolution to generate the insert features reliably. In addition, the MED610 is claimed to be biocompatible by the manufacturer [165]. The silicone catheter material served as a non-toxic negative control. 0.06% hydrogen peroxide served as the positive control, inducing a cytotoxic response [166]. Blank samples without any material were also tested.

Caco2 epithelial cells (ATCC: HTB-37) were seeded onto sterile glass coverslips and grown to sub-confluency at 37 °C under 5% CO_2 in Dulbecco's Modified Eagle Medium (DMEM) with 10% Fetal Bovine Serum (FBS) in a standard 24-well cell culture plate (BD). Material samples were prepared using a modified washing/rinsing protocol described by Ngan et al. [167]. Any support material remaining on the MED610 after 3D-printing was removed using a 2% sodium hydroxide and 1% sodium sulfite solution, which was then neutralized using 5% acetic acid for one minute. Subsequently, samples from both printers were soaked in DI water for one minute then sonicated in isopropyl alcohol followed by DI water for 2 hours. Finally, the samples were sterilized in 70% ethanol and allowed to dry in a sterile biosafety cabinet under UV irradiation.

The cleaned samples were immersed in DMEM with 10% FBS at 37 °C for 24 hours. This temperature corresponds to average body temperature, and the duration of immersion corresponds to a catheter that was indwelling for one day. These conditions help to ensure that the biocompatibility assay results were relevant for indwelling catheters. The samples were then removed, and the remaining solution was referred to as the extract, containing the variety of compounds that may have leached out of the 3D-printed material into the surrounding media. The extract was then introduced to the sub-confluent culture and incubated at 37 °C for 24 hours. The cells were imaged using bright field optical microscopy (Olympus, CKX53) before and after exposure to the extract. After exposure and bright field imaging, the cells are fixed in 4% paraformaldehyde. This was done by removing the media, gently rinsing with tris buffer, and immersing with paraformaldehyde for 10 minutes in each well. Then, the wells were stained for viability using LIVE/DEAD stain (Thermo Fisher Scientific) and imaged using a confocal microscope (LSM 700, Zeiss). The LIVE/DEAD stain consisted of 1.5 µl/ml each of propidium iodide and syto-9 in tris buffer. The stain was incubated in each well for 15 minutes. The samples were then mounted onto glass slides after being rinsed with tris buffer. Each type of sample was done in triplicate.

3.1.2 Foley catheter integration

A Foley catheter was integrated with the device insert module, as depicted in Figure 3-2 (b). The modular assembly of the flexible IDEs and 3D-printed insert allows facile integration at a sliced interface of the commercial urinary Foley catheter via two flow channels - saline and urine channels. The insert module is integrated near the distal tip close to the balloon with the sensor on the inner lumen, as this is the area most commonly colonized by biofilm [168]. A major design consideration was to maintain the standard urinary Foley catheter configuration when integrating

the insert module and associated electronics. This was to assure that the primary functions of the urinary catheter (urine drainage, bladder anchoring by inflating the balloon at the tip) would be sustained. The system displayed appropriate liquid drainage from the bladder through the normally inserted catheter without any leakage, draining water at a rate of 2.5 ml/min over four hours (Figure 3-3). In addition, this system enabled inflation of the anchoring balloon, demonstrating that the intended function of the catheter is maintained (Figure 3-4). This approach allows not only unimpeded functionality of the Foley catheter but will also enable biofilm management via the integrated flexible device.

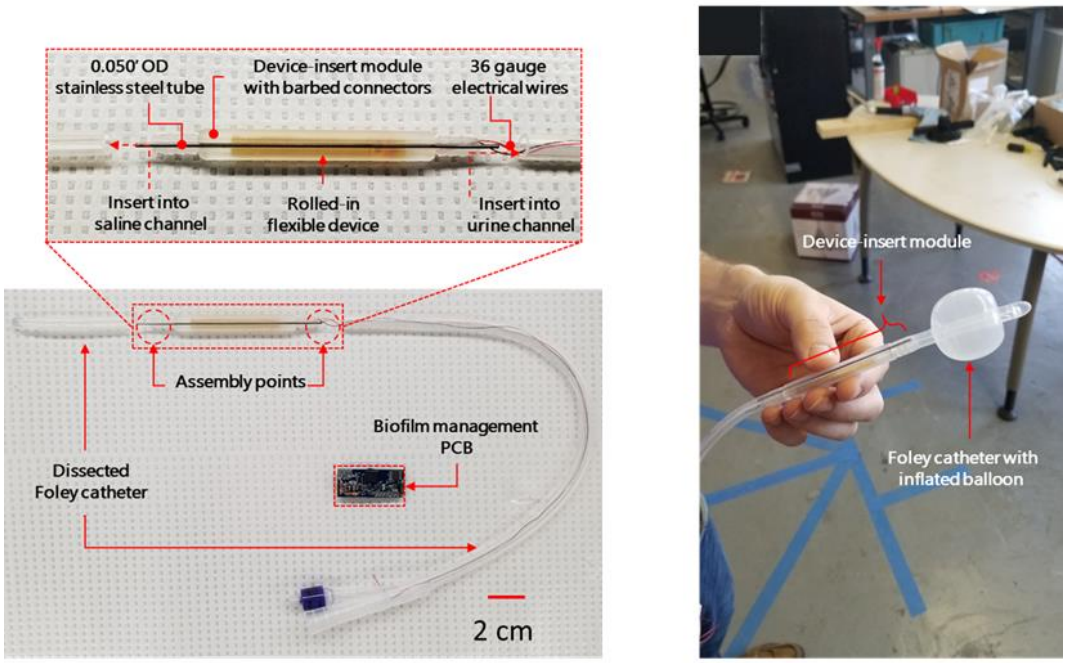

Figure 3-2: (a) Components comprising integrated system including steel tube for saline balloon inflation channel, 36 AWG wires to connect PCB with embedded sensor, flexible IDEs, and 3D-printed insert module with barbed connectors for leak proof connection with urine drainage channel. (b) Optical image of insert module interfaced with 22 Fr Foley catheter with inflated balloon [169].

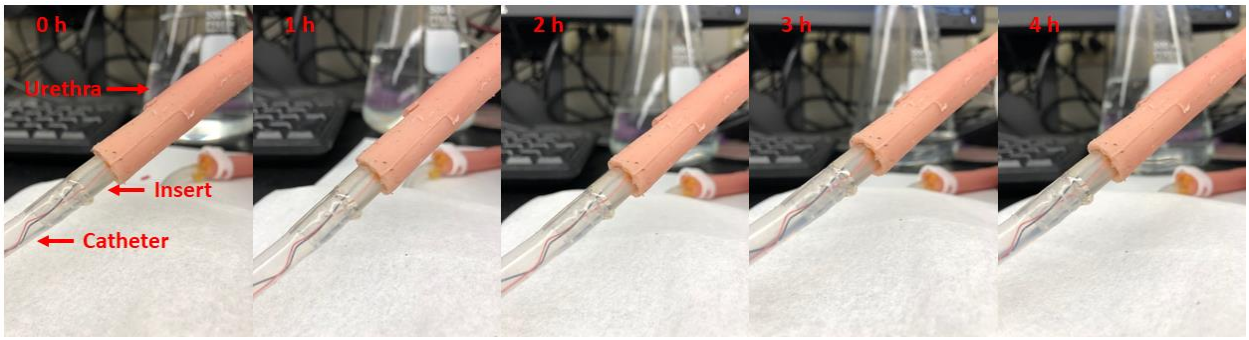

Figure 3-3: System inserted into silicone bladder with water flowed continuously over 4 hours at 2.5 ml/min. Optical images confirm no leakage from the insertion interface [169].

Figure 3-4: Optical image of device inserted into translucent silicone bladder, showing the anchoring balloon inflated with phosphate buffered saline solution colored with blue food coloring [169].

3.1.3 Biocompatibility testing

It is very important to establish that this approach is not harmful towards the host when inserted. This is a key concern of regulatory agencies such as the US Food and Drug Administration. Towards this end, I evaluated the cytotoxicity of the potential materials for the Foley catheter insert using a protocol based upon the ISO10993-5 standard for evaluating material cytotoxicity [163]. Representative bright field images of the cells at subconfluency immediately before the addition of the material extract and after 24 hours of exposure to each of the material

extracts are shown in Figure 3-5. In each case, the cell morphology does not show a noticeable change. The exception is the positive control containing hydrogen peroxide; these cells are small with rounded morphology indicative of cell damage [170]. This result is further examined by the LIVE/DEAD stain images showing healthy cells with propidium iodide concentrated on the outer membranes and syto-9 concentrated within the cells at the nucleus (Figure 3-6). This stain indicates healthy membrane integrity, in addition to cell morphology. Again, the positive control is an exception, showing poor morphology with propidium iodide penetrating the intracellular space due to poor membrane integrity. Notably, MED610 also showed poor morphology with the LIVE/DEAD stain. This could be indicative of some harmful compound being released, such as MED610 support material. This support material is potentially toxic, and it has been shown that thorough cleaning processes are necessary to remove these materials to ensure optimal biocompatibility [167].

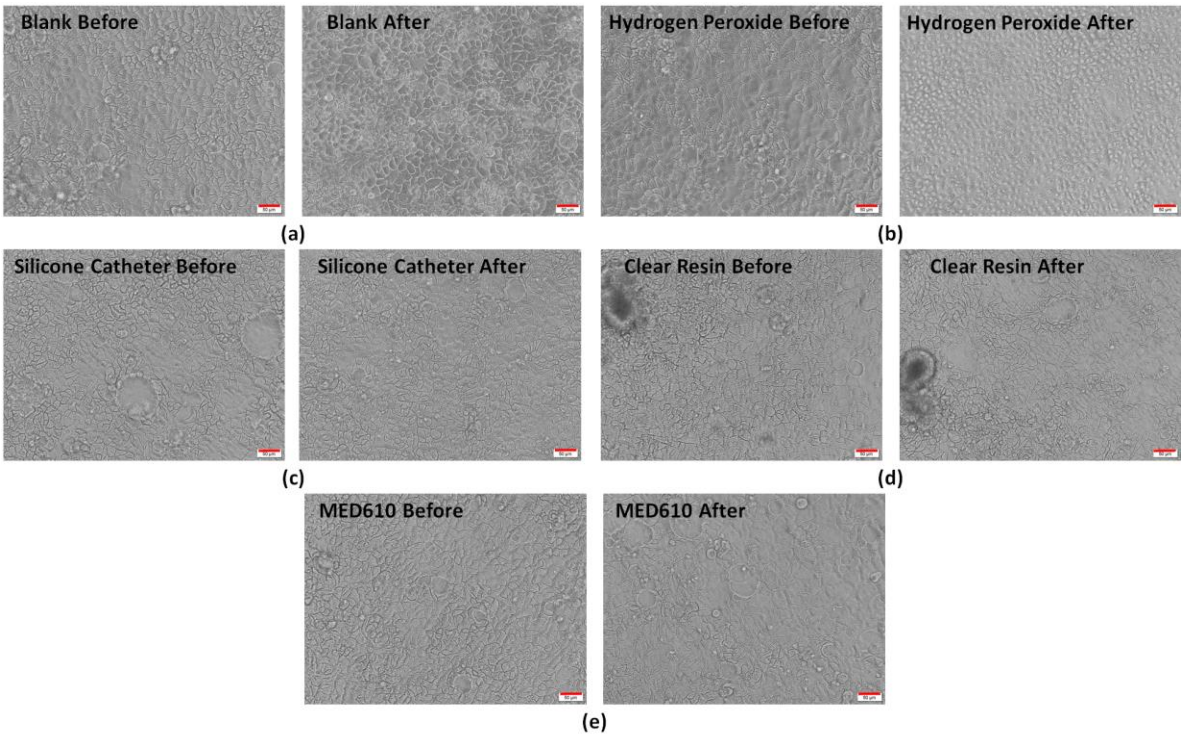

Figure 3-5: Brightfield images of representative samples before (left) and after (right) exposure to material extracts: (a) blank sample, (b) hydrogen peroxide (positive control), (c) silicone catheter (negative control), (d) clear resin, and (e) MED610. Scale bar corresponds to 50 µm.

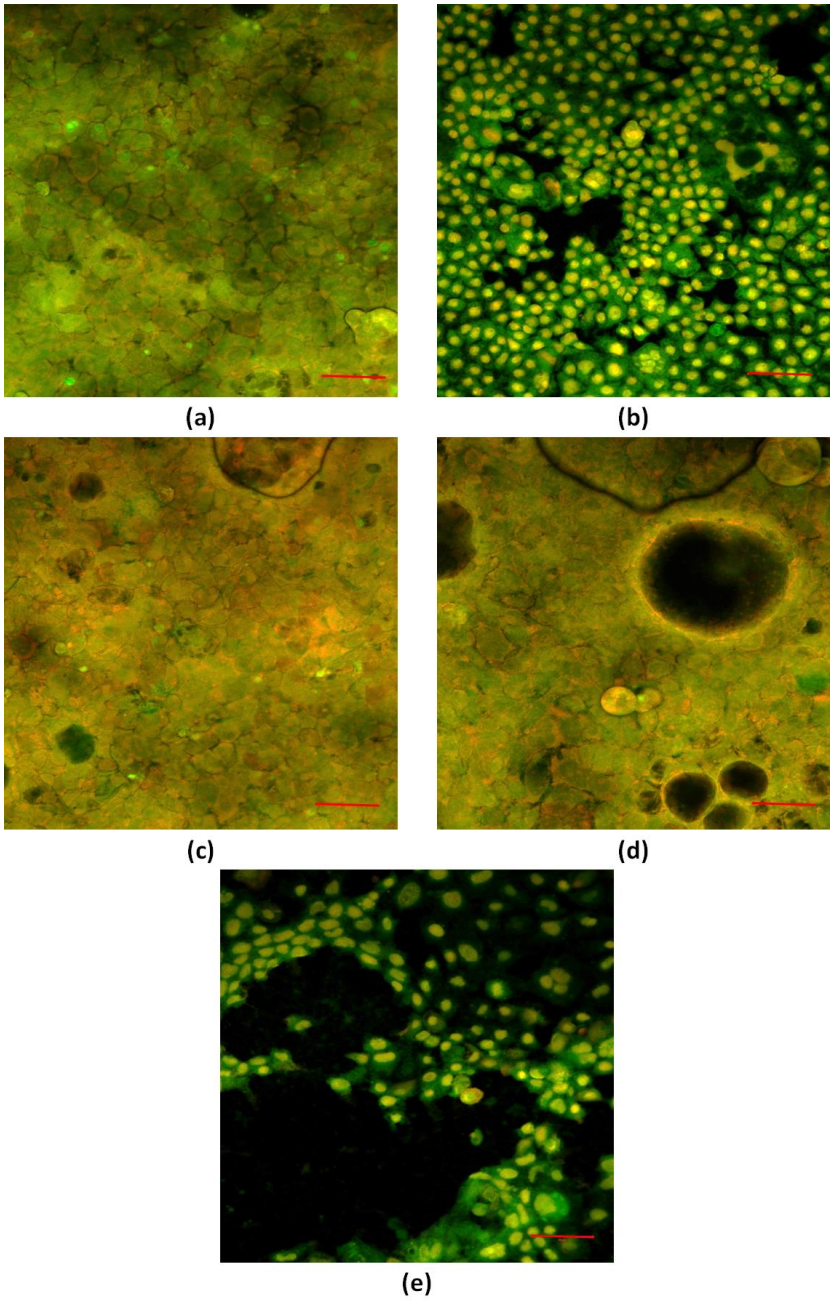

Figure 3-6: Representative LIVE/DEAD stain images after exposure to material extracts and fixing with formaldehyde: (a) blank sample, (b) positive control (hydrogen peroxide), (c) negative control (silicone

catheter), (d) clear resin, and (e) MED610. Contrast was decreased 20% and brightness was increased 40%. Scale bar corresponds to 50 μm.

This analysis suggests that there are not harmful leachates in the clear resin that will damage human cells. It is also important to note that the standard clear resin does not have a secondary support material that may be toxic and easily leached into the surrounding environment, as seen with MED610. Improving the washing protocol to better remove this material could improve the biocompatibility of MED610. This analysis only examined one aspect of biocompatibility – the material leached from the device into the environment. These potentially harmful leachates are important when evaluating cytotoxicity of indwelling devices [167]. However, this analysis did not include direct contact between the materials and the cells, as occurs when a catheter is inserted. Furthermore, testing should be performed utilizing a more realistic medium, such as artificial urine. These experiments would help further establish the viability of these materials for an integrated catheter system.

3.2 In situ *Fabrication of Urinary Catheter Electrodes*

The insertion process for integrating flexible electrodes can present limitations as the rolling/deforming of the brittle thin-film metal electrodes can lead to unwanted fractures and poor electrical contact [171], [172]. Furthermore, electrode-based transducers fabricated on non-stretchable polymeric substrates do not conform well to more complex surfaces [173]. In this section, I overcome this potential challenge by incorporating direct plating of the electrodes onto the catheter surface, with 3D-printed templates serving to selectively screen the catheter surface. This process does not rely on cumbersome fabrication technologies such as photolithography and physical vapor deposition. Instead, an aqueous electroless plating process is carried out directly on the inner lumen of the catheter with the 3D-printed mold, and a subsequent electroplating process

completes the electrode patterning. Electroless deposition of nickel yields a conformal metal coating via immersion in a plating bath, and this layer acts as a conductive seed layer for gold electroplating [174], [175]. I demonstrate electrode fabrication and biofilm sensing directly on the cylindrical polymeric surface of the catheter. Given the multitude of medical devices with similarly complex polymeric surfaces that would benefit from integrated sensors, this technique has the potential to be readily applied for a wide range of applications.

3.2.1 Materials and methods

The gold impedance sensor electrodes were fabricated directly on a 22 Fr elastomeric Foley catheter (Bard) using the process depicted in Figure 3-7. (i) The catheter was initially coated in a 25 µm-thick layer of parylene-C (Specialty Coating Systems, Labcoter 2) to reduce the mechanical mismatch between the plated metal and the silicone polymer substrate and improve adhesion. Cracks appeared in the metal without this initial parylene-C layer, resulting in a significant loss of conductivity. (ii) The samples were then cleaned using acetone, methanol, and isopropanol to be prepared for the following Ni electroless plating step. Oxygen plasma treatment (200 W, 1 min) (Branson, Barrel Photoresist Stripper) introduced reactive carboxylic groups to the surface of the parylene-C to improve the adhesion of the electrodes. Immediately after oxygen plasma treatment, the catheters were immersed in 0.026 M stannous chloride solution in 1:1 methanol and water with 0.07 M trichloroacetic acid for 45 minutes. This sensitization step bonded tin ions to the surface. After rinsing with methanol, a 3D-printed mold was inserted into the catheter, screening portions of the inner lumen from the electroless plating solutions and producing separate electrodes. 3D printing dramatically simplified the electrode patterning compared to techniques like photolithography, particularly in hard to reach areas like the catheter lumen. The mold was printed using a FormLabs Form 2 SLA 3D printer with clear resin. After the mold was added, the catheter

was filled with a 10 mM sodium tetrachloropalladate solution for 5 hours, which replaces the tin on the surface with palladium. Palladium served as a nucleation site for the formation of the nickel seed layer for the following gold electroplating step. Immersion for 45 seconds in a nickel electroless plating bath generated a thin nickel layer (<50 nm) on the catheter inner lumen. (iii) The 3D-printed mold was removed for the Au electroplating. The device was immersed in TSG-250 (Transene) commercial electroplating solution and cycled from 0 to -0.5 V for 100 cycles at a scan rate of 25 mV/s using a VSP-300 potentiostat (Biologic). (iv) The resulting electrodes were then coated with a 1-μm thick layer of parylene-C to prevent metal ions from leaching into the environment. SEM and energy dispersive spectroscopy (EDS) analysis were used to examine the cross section of the fabricated device.

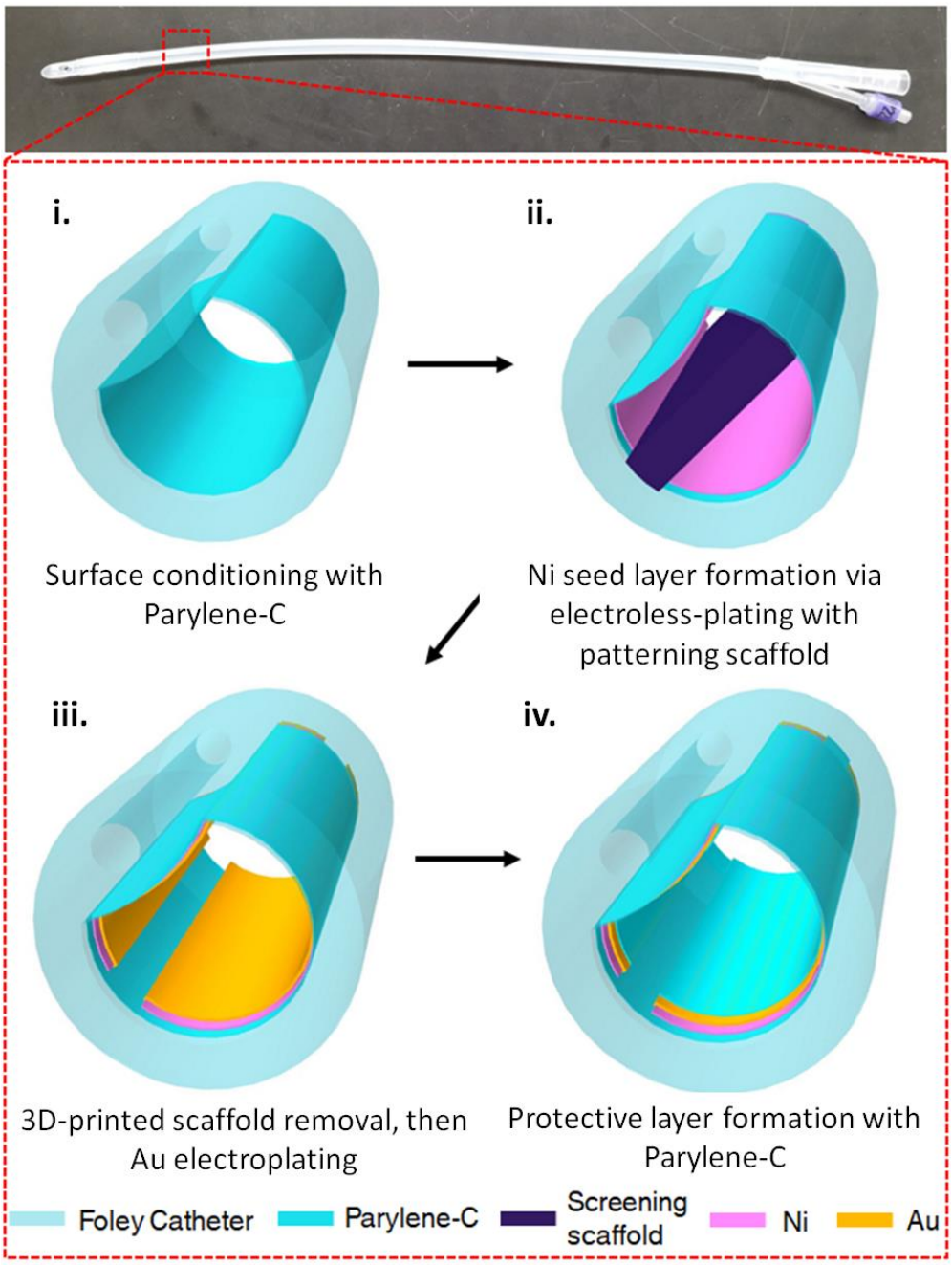

Figure 3-7: Foley catheter and the process flow depicting the *in situ* sensor electrode patterning on the inner lumen of a urinary catheter for biofilm detection [176]. © 2019 IEEE

As depicted in Figure 3-8, the catheter sections with plated electrodes were interfaced with tygon tubing (Cole Parmer) to form a flow system for introducing fresh LB growth media (Sigma) and bacterial cells. Electrical connections were made using 24-gauge wire clipped to each of the

two electrodes. The electrical connections and tubing were sealed using epoxy. A peristaltic pump (Cole Parmer) was used to drive flow at 7 ml/h through the system from an LB media reservoir through the catheter with the sensor to a waste reservoir. The media and waste reservoirs were sterilized in an autoclave at 121 °C. The catheter and tubing were sterilized by flushing with ethanol and UV light exposure for an hour. The entire system was assembled in a sterile biosafety cabinet.

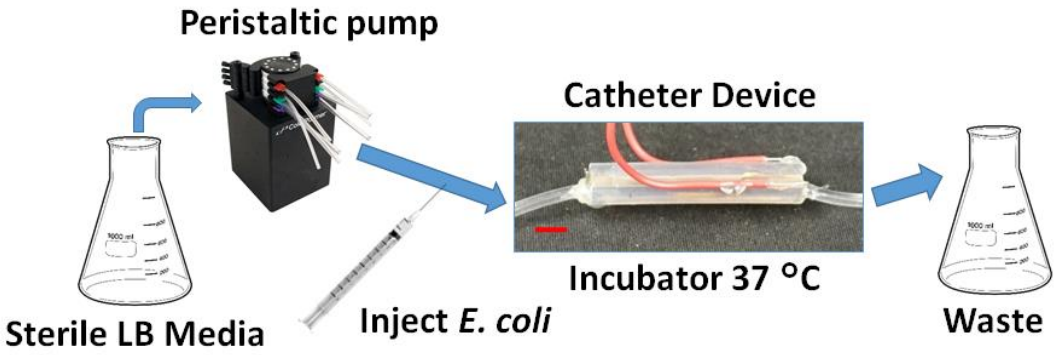

Figure 3-8: Experimental setup comprised of the catheter device interfaced with media and waste reservoirs via tygon tubing for delivering fresh media during biofilm growth experiments. Scale bar 5 mm [176]. © 2019 IEEE

Escherichia coli K12 W3110 were cultured overnight in a 5 ml culture tube in an incubator shaker (Brunswick Scientific) at 250 rpm and 37 °C. The bacterial culture was diluted to an $OD_{600\ nm}$ of 0.25 and added to the system via syringe. The bacteria were allowed to attach for 2 hours to the sensor surface under a no-flow condition. Then, LB media was flowed for 24 hours as the biofilm grew. No bacterial cells were added in the control samples. Impedance spectra were gathered using a potentiostat (CHInstruments) from 10-10^6 Hz at a 50 mV amplitude. These spectra were gathered before the introduction of bacteria with LB media only, at the beginning of the 24-hour biofilm growth period, at the end of the biofilm growth period, and after the growth period after cleaning with ethanol. This last measurement with LB examined the electrode

integrity. In addition, the impedance was monitored in real-time at 100 Hz throughout the growth period.

3.2.2 Electrode materials characterization

The sensor electrodes patterned on the inner lumen of the catheter are shown in the cross-section image of the catheter section in Figure 3-9 (a), demonstrating the viability of this approach for patterning electrodes for sensing on a catheter. The pattern used in this case was a rectangular mold with rounded edges (Figure 3-9 (b)) to screen the inner catheter lumen for selective electroless plating. More complex electrodes with larger sensor interfaces could be produced using more complex 3D printed molds, such as interdigitated patterns. Figure 3-9 (c) i-iii shows cross-section SEM images from the electrode-patterned catheter with corresponding EDS scans. The silicone, metal, and the two parylene-C layers are shown distinctly on the surface. EDS analysis (Figure 3-9 (c-d)) confirms each of these layers by means of their signature elements, gold at 2.120 keV (electrodes), chlorine at 2.622 keV (parylene-C), and silicon at 1.749 keV (silicone catheter). The key difference between the screened (Figure 3-9 (c) i) and the exposed (Figure 3-9 (c) ii) areas is the lack of a metal layer. The well-defined electrode pattern edge (Figure 3-9 (c) iii) clearly indicates the success in use of the 3D-printed screening mold for patterning of *in situ* electroless plating on curved confined surfaces.

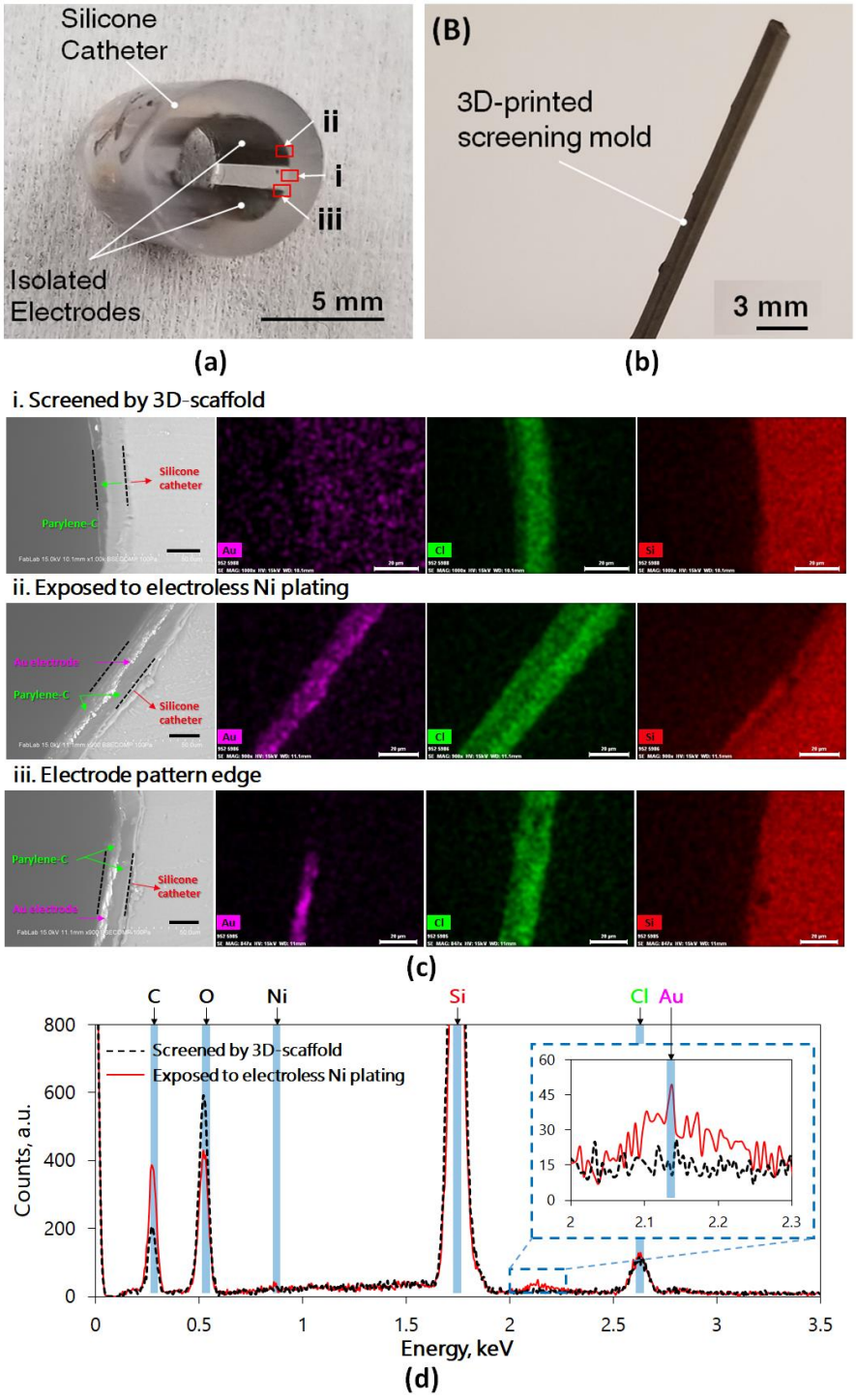

Figure 3-9: (a) Cross-sectional optical image of the *in situ* electrode patterned Foley-catheter. (b) Optical image of the 3D-printed mold for selective screening of electroless plating process, which appears black due to the nickel layer. (c) SEM characterization corresponding to areas (i-iii) in (a) of layer formation with EDS scans from gold, chlorine, and silicon, which are the signature elements for the electrodes, parylene-

C, and the catheter, respectively (scale bar: 20 μm unless specified). (d) A comparison EDS spectrum acquired from catheter sections screened by the screening mold (black) and exposed to Ni electroless plating (red), confirming selective pattering of gold electrodes [176].

3.2.3 Plated electrode biofilm sensing

Impedance spectroscopy at the beginning and after 24-hours of biofilm growth displayed a frequency-dependent decrease in impedance associated with biofilm growth (Figure 3-10 (a)). This is consistent with previous reports and the results from Chapter 2, indicating that the capacitive component of the impedance changes with biofilm formation due to the accumulation of charged proteins and metabolites, leading to a decrease in capacitance [15], [148], [149]. In contrast, control samples without any biofilm showed a frequency-independent increase in impedance (Figure 3-10 (b)). We suggest that this is related to electrode degradation, potentially caused by the dissolution of metal ions due to the applied voltage in an electrolyte media containing chloride ions [177]. This is further evidenced by impedance spectroscopy of the sensor electrodes, which had been used to detect biofilm before the cells were added and after cleaning with ethanol. The electrodes displayed a frequency-independent increase in impedance when measuring the impedance in LB media after the electrodes had been cleaned of biofilm (Figure 3-10 (c)). A similar trend is seen in the control electrodes before and after the growth period (Figure 3-10 (d)). The increase in impedance after the removal of biofilm with ethanol reinforces the role of biofilm in the decrease in impedance seen with the sensor. Overall, this suggests that this is a viable approach for sensing biofilm on urinary catheters.

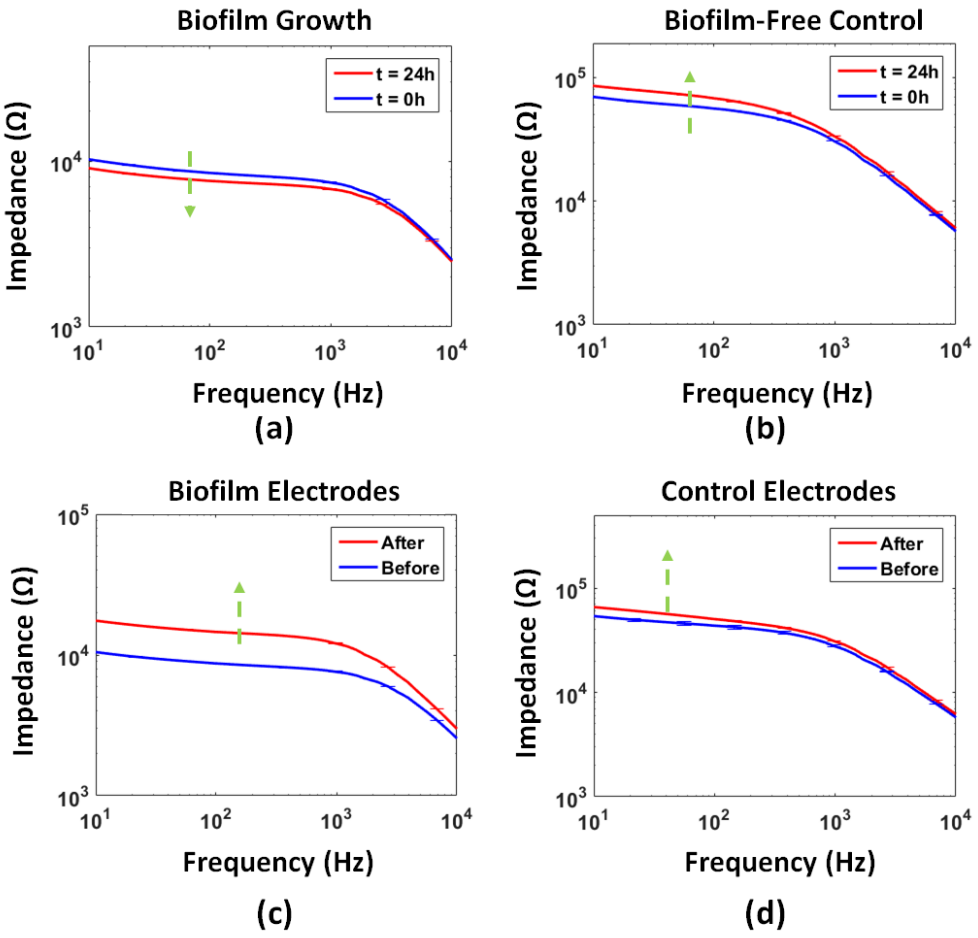

Figure 3-10: 50 mV impedance spectra with *in situ* fabricated electrodes (a-b) at the beginning of the biofilm growth period (blue) and at the end of 24 hours of biofilm growth (red). Samples with biofilm (a) showed a decrease in impedance, whereas control samples (b) without bacterial cells showed an increase in impedance (N = 3 measurements). (c-d) Electrodes in only LB media before and after use in biofilm sensing experiments for (c) biofilm sensing and (d) control samples (N = 3 measurements) [176]. © 2019 IEEE

The *in situ* patterned electrodes were further utilized for continuous, real-time monitoring of biofilm formation. This is an essential element of more effective biofilm infection management, allowing a continuous readout of the state of the device surface. 100 Hz was selected for biofilm monitoring, as it is in the middle of the frequency range, which displayed an impedance decrease (Figure 3-10 (a)) consistent with the results from Chapter 2. The impedance was recorded

continuously for samples with and without biofilm over 24 hours (Figure 3-11). The samples with biofilm showed a sharp decrease over the first 7 hours, followed by a plateau of relatively little change over the next 17 hours. In total, the impedance decreased approximately 10% over the 24-hour period. This is consistent with the growth dynamics of bacterial biofilm, with a rapid growth phase followed by a stationary mature biofilm phase [109]. In contrast, the control sample without any bacterial cells showed an increase in impedance of approximately 20%. This increase was relatively steady throughout the 24-hour period. We suggest that this is due to the electrode degradation and the formation of small bubbles that arise due to thermal expansion when the media becomes warmer in the incubator after being stored at room temperature.

These results were also compared to continuous biofilm impedance sensing results using the flexible impedance sensor conformed on a urinary catheter. This device was fabricated monolithically using photolithography, and then must be rolled and inserted into the catheter. Both the control and biofilm sensing samples displayed similar behavior to the *in situ* fabricated electrodes. Each of the biofilm samples showed a significant decrease in impedance, but the *in situ* fabricated electrodes saturated faster. This is not considered a problem as the initial onset of biofilm formation is most important for prompt infection detection. The larger overall decrease with the flexible device is attributed to the larger electrode interface; this device was comprised of interdigitated electrodes.

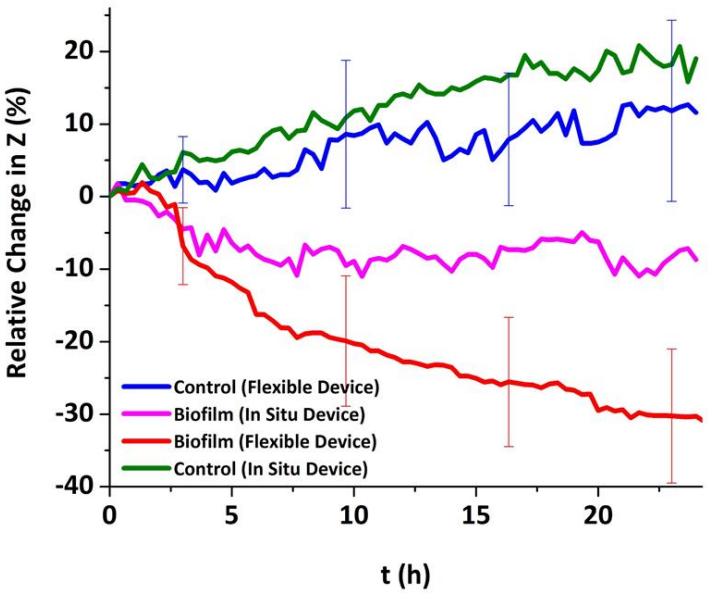

Figure 3-11: Impedance transients at 100 Hz showing real-time biofilm sensing results. The green and blue lines show the increasing impedance of control samples for the *in situ* fabricated device and flexible device, respectively. The magenta and red lines show the decreasing impedance for the biofilm samples of the *in situ* fabricated device and flexible device, respectively [176]. © 2019 IEEE

We have introduced an innovative *in situ* fabrication strategy for producing sensor electrodes on inaccessible medical device surfaces, particularly on urinary catheters. The sensors show similar performance to externally fabricated biofilm impedance sensors without a complicating integration step. It should be noted that this approach was only demonstrated on sections of a urinary catheter. The patterning scaffold would need to be redesigned to robustly pattern a full-scale catheter. This sensor system has the potential to serve as an integral tool for biofilm infection management. This technique can be applied to additional medical device surfaces that are vulnerable to biofilm colonization, particularly polymeric surfaces with complex geometries. Furthermore, introducing more complex mold designs to increase the electrode interface can improve the performance of these devices.

3.3 Custom Electronics Development for Wireless Control of Sensing and Treatment

In order to integrate this sensing and treatment approach most effectively with a urinary catheter, the electronics and control systems that accompany the flexible transducer also need to be integrated in a seamless and user-friendly manner. To achieve this goal, commercial off-the-shelf (COTS) electronic components were utilized to miniaturize the sensing and treatment control system. This approach also enables wireless communication via Bluetooth, allowing patients and healthcare providers greater freedom while monitoring biofilm growth and administering treatment. Also, a custom mobile application was developed to facilitate the implementation of this system by researchers and clinicians who have no special expertise in utilizing this type of transducer. This application integrates both functionalities in a seamless way using a single interface. In this section, I describe the custom-developed electronic system and mobile application in detail. In addition, I confirm the viability of the COTS impedance converter used for biofilm monitoring.

3.3.1 Biofilm management printed circuit board (PCB)

The goal of the embedded system development was to incorporate the impedance sensing and BE treatment capability presented in previous sections with a user-friendly interface and control system, which can be seamlessly integrated with an indwelling catheter in either a hospital or ambulatory setting. The PCB can be adhered to the external portion of the catheter, connected via 36 AWG wires (McMaster), and reused. The key specifications for the circuit design include effective implementation of the sensing and treatment signals, small form factor, low power consumption, and the ability to transfer data wirelessly. Furthermore, the system was specifically designed to measure impedances on the order of 10^2 Ω, which was determined in previous sections.

The circuit for the biofilm management PCB, shown in Figure 3-12, contains three critical components: the BGM121 Bluetooth microcontroller unit (MCU), the AD5933 (Analog Devices) impedance sensing module, and the AD2S99 (Analog Devices) sinewave oscillator [178]–[180]. The BGM121 MCU is an ideal wireless Bluetooth Low Energy (BLE) solution (Silicon Labs), which contains several energy modes to conserve power, an integrated antenna for efficient radio frequency data transmission, necessary peripheral functions to obtain data, and a robust integrated development environment for MCU programming. This system allowed wireless control over switching between three major modes of operation: Sensing mode with the AD5933, Treatment mode via the AD2S99, as well as a Shutdown mode that consists of both ICs being switched off for efficient energy use. In Sensing mode, the AD5933 measures the 2 kHz impedance of the electrodes to determine the degree of bacterial growth. In Treatment mode, the AD2S99 generates a 20 kHz sine wave that has been shown to be capable of inducing the BE [153]. Electrical specifications for the BGM121, AD5933, and AD2S99 are summarized in Table 3-1.

Power State and Current Consumption for Key Components					
Mode	**BGM121**	**AD5933**	**AD2S99**	**Current (mA)**	**Output**
Sensing	ON	ON	OFF	~25	2 kHz, 0.600 mV
Treatment	ON	OFF	ON	~40	20 kHz, 0.650 mV
Shutdown	ON	OFF	OFF	~<1	NONE

Table 3-1: Specifications for each of the key components in each mode of operation.

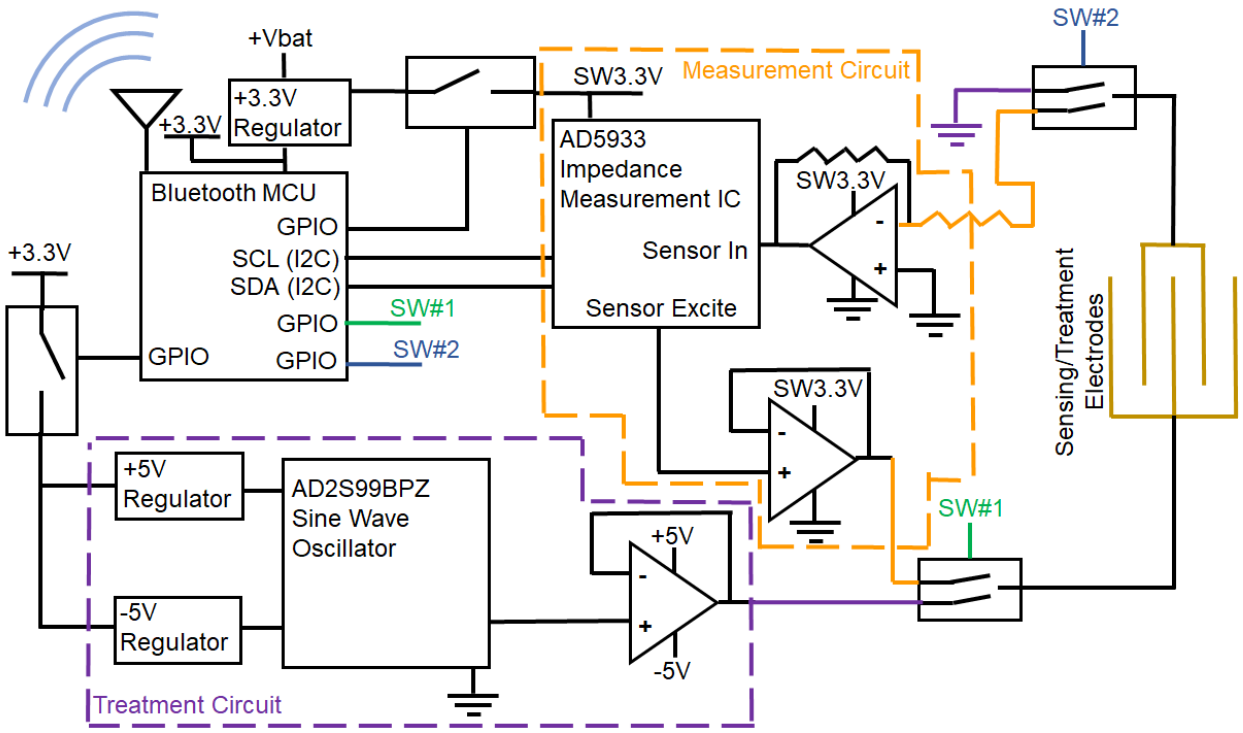

Figure 3-12: Circuit diagram for the PCB incorporating Bluetooth MCU, impedance sensing module, and sine wave oscillator for wireless detection and treatment of bacterial biofilms on catheters [169].

Figure 3-12 depicts the circuit diagram for the custom PCB. The MCU connects to the AD5933 impedance sensing module via an I^2C serial interface. The AD5933 is responsible for generating a 2 kHz, 0.600 mV signal across the flexible electrode and digitizing the sensor impedance output using a built-in analog-to-digital-converter for data acquisition. The AD5933 is configured, per the datasheet [179], to measure small impedances (< 1 kΩ) by placing op-amps at the Sensor Excite pin to amplify the excitation signal and at the Sensor In pin to properly bias the signal. More specifically, the op-amp at the AD5933 output is a non-inverting buffer, and the op-amp at the AD5933 input is in an inverting configuration with a gain of 10. In this case, the AD5933 is setup to measure impedance at a single frequency, 2 kHz. For the treatment circuit, the AD2S99 is configured to create a 0.650 Vpk-pk sine wave with a 2.5 V DC offset, which is applied via a voltage divider circuit. An op-amp buffer is used to isolate the output of the oscillator from

the current load of the biofilm electrodes. Voltage controlled switches are used to alternate the signals going to the biofilm electrodes between those needed for the AD5933 (sensor in/sensor out) and those needed for the AD2S99 (oscillator output and ground). This fully isolates both circuits from the electrodes when the other circuit is being used. Voltage regulators are used to generate 3.3 V, 5 V, and -5 V, which are needed to drive each of the components. To conserve power, power switches (TPS22810, Texas Instruments) are used to turn off the power going to either the sensing or treatment circuits when not in use.

The entire circuit is laid out on a 15.5 mm wide by 37 mm long (Figure 3-2 (a)) custom four-layer FR-4 PCB using Eagle AutoCad (Autodesk). Per the datasheet for the BGM121 [178], specific considerations are required to ensure that the on-package antenna can operate efficiently and propagate the 2.45G Hz wireless signal. Major considerations for the board layout that directly relate to propagation distance are the placement of the chip (i.e., centered with the edge where the antenna is located next to the board edge) and the ground plane clearance areas in the board layers surrounding the antenna (to avoid a short). The signal transmission was assessed using received signal strength indicator (RSSI), where decreasing values correspond to decreasing signal strength. The BGM121 antenna has a sensitivity of -90 dBm; if the RSSI is any lower, the signal is no longer being received reliably. Taking these considerations into account, the board is able to transmit a Bluetooth signal to a smartphone at a distance of at least 40 meters within a hallway in our laboratory building (Figure 3-13). This result supports the wireless use of this system in a similar indoor setting like a hospital or care facility when in the same room or nearby.

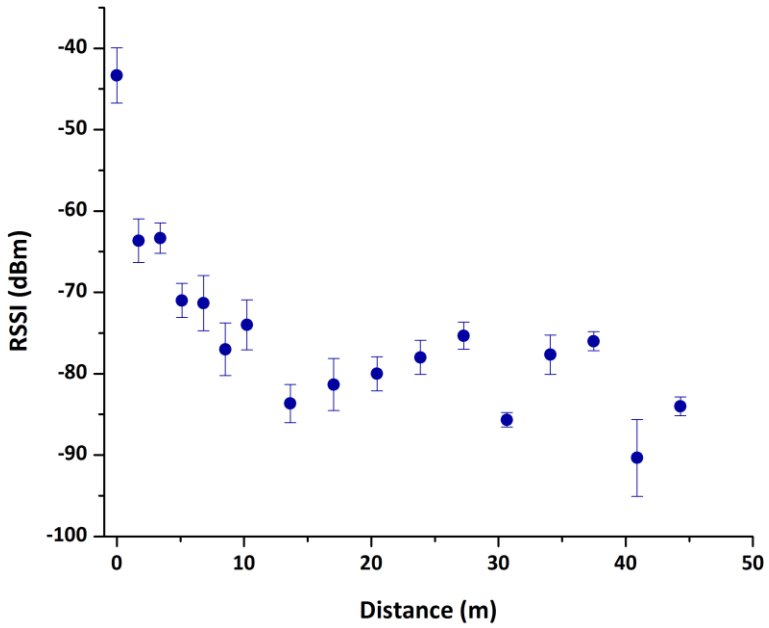

Figure 3-13: Bluetooth transmission relative signal strength (RSSI) between phone and PCB measured in laboratory building hallway (N = 3) [169].

The MCU is used to program the AD5933 via the I^2C interface per the datasheet [179] for configuring the start-up and measurement sequence and to read the data stored within the device registers. A frequency sweep is used to obtain the necessary impedance data, with the measured impedance value recorded at 2 kHz. This was selected to be above the lowest frequency that could reliably be measured using the AD5933. Briefly, commands formatted as 8-bit words are sent to the AD5933 in the following sequence to initiate a frequency sweep. (1) The start frequency, number of frequency increments, and the frequency increment are programmed, (2) the AD5933 is placed in standby mode, (3) the AD5933 is initialized with a start frequency command, and (4) the start frequency sweep command is sent after a specified settling time. (5) The MCU then polls a status register to see if the frequency data is present. (6) If data is present, the impedance value is read from the AD5933 and (7) the MCU polls the status register to see if the frequency sweep is complete. (8) If it is not complete, the frequency is incremented and the measurement is repeated

starting with step (5), and if the frequency sweep is complete the AD5933 powers down. A key consideration for the impedance measurement circuit is the calibration of the AD5933. This is accomplished using resistors with known impedance values, as described in the AD5933 datasheet [179].

3.3.1.1 Impedance converter biofilm sensing

The AD5933 impedance converter was utilized to miniaturize the impedance sensing functions of this system. The first step towards implementing this component was verifying its capability for biofilm sensing. This was evaluated using the setup described in Figure 2-3. Real-time impedance monitoring was performed with the AD5933 impedance converter. The 200 mV impedance at 1 kHz was measured every 2 minutes by connecting the device leads to the AD5933 on the UG-364 evaluation board (Analog Devices), utilizing the accompanying evaluation board software. The different sensing parameters were selected due to the limitations of the evaluation board and AD5933. The 200 mV was the minimum excitation signal possible with the board, and 1 kHz was the minimum frequency that could be reliably measured using the AD5933.

Impedance changes measured with the AD5933 impedance converter are depicted in Figure 3-14. The trends produced reflect the similar sensing characteristics measured with the potentiostat for both control and biofilm samples. The biofilm-free samples yielded a slight increase in impedance, after the 24-hour growth period, of approximately 2%. By comparison, biofilm formation led to a drop of about 5% in the measured impedance after 24 hours of growth. The most notable difference between the results with the AD5933 and the standard benchtop potentiostat is the decreased magnitude of the changes in impedance for both samples. The signal change equated to only 16% of the average percent change seen in Figure 2-7 over the same period using the potentiostat. This decreased sensitivity is likely attributed to differences in system

calibration and variations in impedance of the measurement electronics. It is also important to note that the frequency used in this case was higher (1 kHz versus 100 Hz in previous setup) and therefore, may be less sensitive to biofilm formation. Nonetheless, the similar trend versus the standard indicates that biofilm detection with AD5933 is feasible.

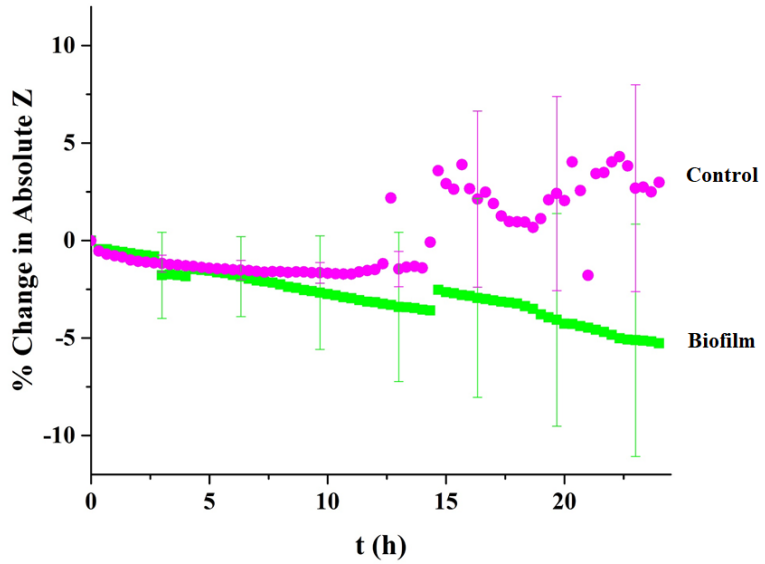

Figure 3-14: Percent change in 200-mV impedance at 1 kHz measured with the AD5933 impedance converter for biofilm (green) and control (pink) samples over a 24-hour growth period, showing a steady drop associated with biofilm growth. The large standard error indicates the high inherent variability of biofilm formation (N = 3) [148]. © 2018 IEEE

CVS was also performed per the procedure described in Chapter 2 to quantify the end-point biomass for samples measured with the AD5933 to correlate the change in impedance with an increase in biomass from biofilm. The biomass quantification results for samples measured with the AIC are shown in Figure 3-15. These samples displayed a significant increase in biomass associated with the formation of biofilm compared to biofilm-free controls, similar to the potentiostat measured samples. The increased absorbance was statistically significant compared to

LB media alone, according to one-way ANOVA ($p < 0.05$). This indicates that the decrease in impedance is correlated with an increase in biomass, as described in Chapter 2. This further confirms the viability of this device combined with the AD5933 for wireless biofilm monitoring.

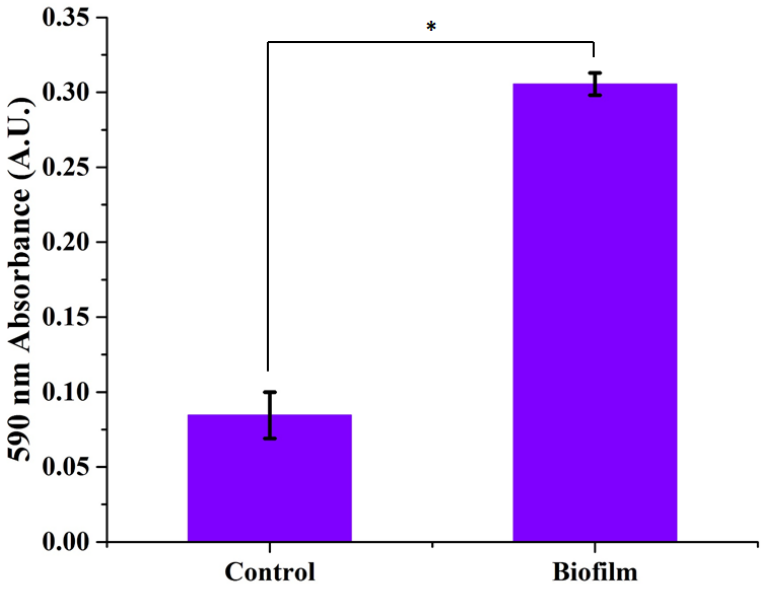

Figure 3-15: End-point biomass quantification for samples with and without biofilm measured with the AD5933. Error bars correspond to standard error (N = 2), *Significance $P < 0.05$ [18].

Initial characterization of this platform utilized a benchtop potentiostat for performing impedance measurements. However, bulky wired equipment is impractical for applications involving inserted medical devices. Here, I demonstrate biofilm detection using the AD5933 to help miniaturize the electronics and overcome this challenge. The AD5933 can be programmed with a BGM121 Bluetooth microcontroller to run impedance measurements and transmit the data wirelessly. The AD5933 was demonstrated as a viable approach for measuring biofilm formation with this device. Compared with the potentiostat standard, the AD5933 demonstrated reduced sensitivity, but the impedance converter successfully measured a decrease in impedance with biofilm formation which correlated with an increase in biomass.

3.3.2 Biofilm management mobile application

Facilitating the use of this system in research and healthcare requires a simple and user-friendly interface that can be used without any prior expertise. To operate the system, a custom, user-friendly mobile application was developed to wirelessly control the PCB and export and display data. The application has both iOS and Android compatible versions and is designed to send commands to the PCB to transition between Sensing, Treatment, and Shutdown modes. In addition, the application reads the raw values from the AD5933 and displays the calculated impedance. Figure 3-16 depicts each of the screens of the application. The application also displays whether the impedance values have surpassed a threshold value that is set by the user to indicate bacterial growth. Overall, this application allows user-friendly control, which facilitates widespread implementation of this tool in research and clinical settings.

After pairing with a device, the device details are shown via a dropdown menu of commands that can be sent to the device, including, Take Measurement, Initiate Treatment, Shutdown, Set Threshold, and Set Gain, summarized and shown in Figure 3-16. Take Measurement begins the impedance sensing, Initiate Treatment prompts the system to output a sine wave for treatment, Shutdown turns off all functions to save power, Set Threshold determines a relative change in impedance, which will trigger a notification in the application, and Set Gain sets the gain factor used to calibrate the sensor via the process described in the AD5933 datasheet [179]. The gain factor and feedback resistor (R_{FB}) used for these experiments, as well as the threshold, are listed in Appendix C.1.

Updates to the measurement parameters, impedance values, and connecting and disconnecting events are recorded in the activity log on the device details screen. This screen also indicates whether the impedance has surpassed the threshold set by the user. The chart icon will

display a chart depicting all of the recorded measurements over time for the currently connected device. When in the pairing screen, the export data feature allows all of the data contained in the activity log to be exported in a spreadsheet. This includes the type of command, impedance data, raw values, time stamps, and device names. A representative export file is shown in Appendix C.2.

After pairing with a device, the device details screen allows control via a dropdown menu of commands that can be sent to the device, summarized below.

i. Take Measurement

This allows a user to take a measurement. When the use selects this command and clicks Send, an input box is displayed. This allows the user to specify how many measurements they want to take and how long the application should wait in between taking measurements. The input format is: [Iterations]*[Duration].

ii. Initiate Treatment

This allows a user to initiate the electric field for treatment. The treatment will continue until either a “Take Measurement” or “Shutdown” command is issued. The user enters the duration of the treatment signal before a “Take Measurement” command is initiated, thus stopping the treatment.

iii. Shutdown

This allows the user to put the device into shutdown mode, reducing current draw to <1 mA. This causes the device to stop ongoing measurements and toggle power switches to the AD5933 and AD2S99 using less power; however, it is still able to receive commands. An “Initiate

Treatment" or "Take Measurement" command will cause the device to come out of sleep mode and perform the action being requested.

iv. Set Threshold

This allows the user to specify a threshold impedance value, which will trigger a notification in the application with the value displayed in red font in the activity log.

v. Set Gain

This allows the user to specify the gain factor to be used when calibrating the impedance measurements using the procedure described in the AD5933 datasheet [179].

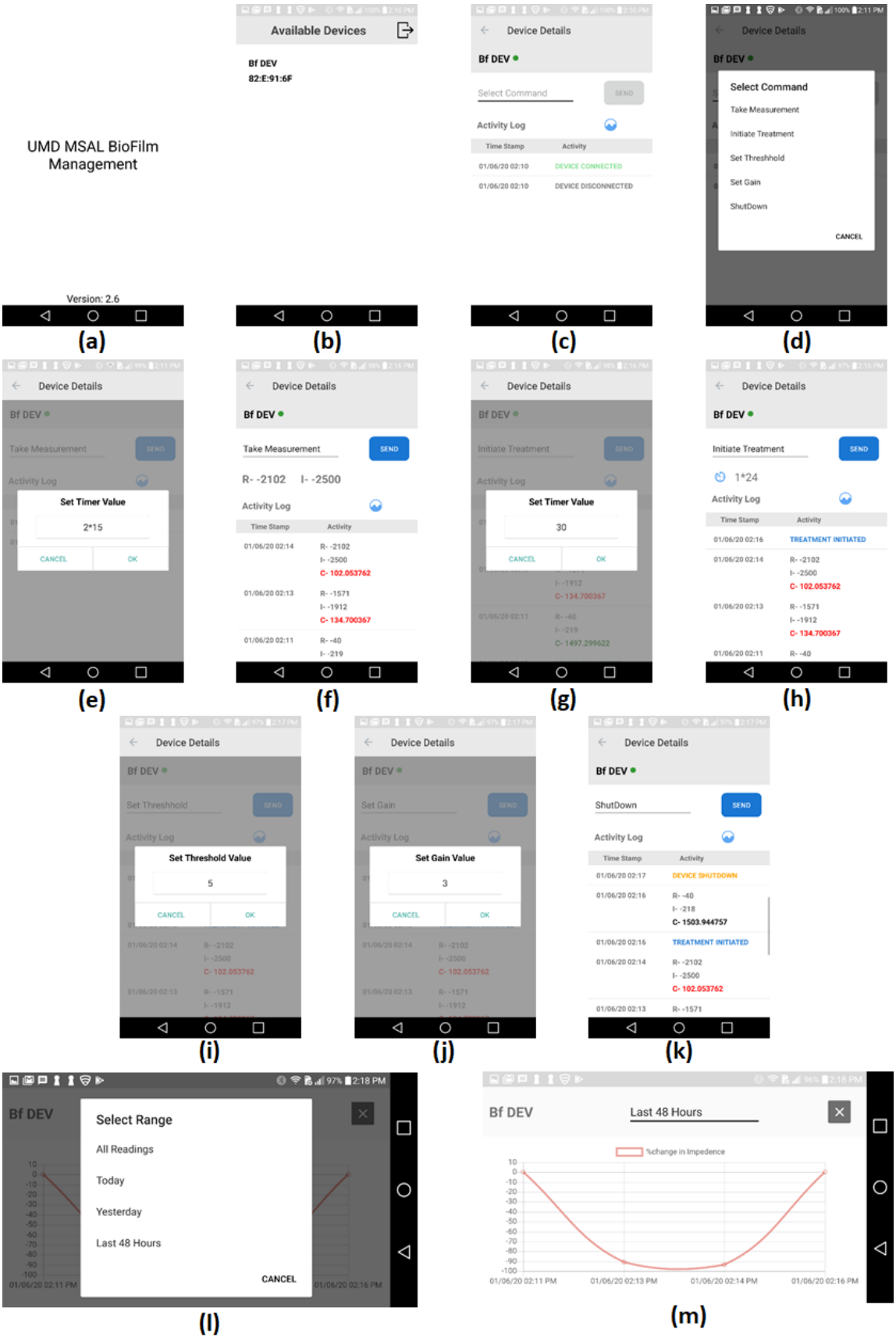
UMD MSAL BioFilm Management
Version: 2.6
(a)
Available Devices
Bf DEV
82:E:91:6F
(b)
Device Details
Bf DEV
Select Command
SEND
Activity Log
Time Stamp
Activity
01/06/20 02:10
DEVICE CONNECTED
01/06/20 02:10
DEVICE DISCONNECTED
(c)
Device Details
Bf DEV
Select Command
Take Measurement
Initiate Treatment
Set Threshhold
Set Gain
ShutDown
CANCEL
(d)
Device Details
Bf DEV
Take Measurement
SEND
Activity Log
Set Timer Value
2*15
CANCEL
OK
(e)
Device Details
Bf DEV
Take Measurement
SEND
R- -2102 I- -2500
Activity Log
Time Stamp
Activity
01/06/20 02:14
R- -2102
I- -2500
C- 102.053762
01/06/20 02:13
R- -1571
I- -1912
C- 134.700367
01/06/20 02:11
R- -40
I- -219
(f)
Device Details
Bf DEV
Initiate Treatment
SEND
Activity Log
Set Timer Value
30
CANCEL
OK
(g)
Device Details
Bf DEV
Initiate Treatment
SEND
1*24
Activity Log
Time Stamp
Activity
01/06/20 02:16
TREATMENT INITIATED
01/06/20 02:14
R- -2102
I- -2500
C- 102.053762
01/06/20 02:13
R- -1571
I- -1912
C- 134.700367
01/06/20 02:11
R- -40
(h)
Device Details
Bf DEV
Set Threshhold
SEND
Activity Log
Set Threshold Value
5
CANCEL
OK
(i)
Device Details
Bf DEV
Set Gain
SEND
Activity Log
Set Gain Value
3
CANCEL
OK
(j)
Device Details
Bf DEV
ShutDown
SEND
Activity Log
Time Stamp
Activity
01/06/20 02:17
DEVICE SHUTDOWN
01/06/20 02:16
R- -40
I- -218
C- 1503.944757
01/06/20 02:16
TREATMENT INITIATED
01/06/20 02:14
R- -2102
I- -2500
C- 102.053762
01/06/20 02:13
R- -1571
(k)
Bf DEV
Select Range
All Readings
Today
Yesterday
Last 48 Hours
CANCEL
(l)
Bf DEV
Last 48 Hours
%change in Impedence
01/06/20 02:11 PM
01/06/20 02:13 PM
01/06/20 02:14 PM
01/06/20 02:16 PM
(m)

Figure 3-16: Mobile application for user-friendly infection management. (a) Splash screen when opening the application. (b) Devices available for pairing, including device name and unique identifier. The upper right corner contains the button for data export. (c) Device details home screen after successful pairing. This includes the activity log that records each action, graph button, and drop-down menu for sending commands. (d) Menu of all commands. (e) Take measurement command interface for performing impedance measurements. The first number corresponds to the number of measurements and the second number corresponds to the interval in seconds between each measurement. (f) Display of impedance results. R is the real component of the impedance, I is the imaginary component of impedance, and C is the total impedance value. Green indicates the initial value, red a value under the threshold, and black a value above the threshold. (g) Initiate treatment interface, showing timer for the duration of the electric field application in seconds. (h) Activity log showing treatment in progress with timer. (i) Interface to set threshold for impedance change in percent. This indicates a user-defined change in impedance below which there may be an infection risk. (j) Command interface for setting the gain factor for impedance sensing calibration. Value is $x10^{-6}$. (k) Activity log showing shutdown command. (l) The options for the graph interface, plotting the relative percent change in impedance over different intervals. (m) Example plot of four measurements [169].

3.4 Synopsis/Summary

In this chapter, I have introduced two distinct approaches for integrating sensing and treatment electrodes with a commercially available Foley catheter. The first approach utilizes a 3D-printed insert, with the flexible electrode rolled and inserted, that interfaces with a cut in the catheter. This approach was relatively robust, allowing both the drainage and anchoring catheter functions to be performed normally. In addition, the materials used for this approach were not found to generate cytotoxic leachates. As an alternative integration approach, I developed a fabrication process utilizing electroless plating and electroplating to generate electrodes directly on the surface of the catheter lumen. Patterning these electrodes was made possible by inserting 3D-printed scaffolds to screen certain areas from the plating solution. These electrodes were shown to be capable of impedance sensing comparable to the impedance sensing seen with the proof-of-concept system from Chapter 2. Finally, I also introduced the electronics system developed to

wirelessly control the catheter device. This includes the PCB containing off-the-shelf components for both sensing and treatment, along with the mobile application for wireless control in a user-friendly manner. The contributions from this chapter demonstrate integration of sensing and treatment electrodes with a urinary catheter, yielding a complete and versatile system for biofilm management.

Chapter 4: Biofilm Management in Synthetic Bladder Environment

In order to advance this technology towards implementation in an *in vivo* or clinical setting, this system first needs to be demonstrated under realistic conditions. The *in vitro* test conditions utilized to evaluate this system in the last two chapters lack certain key aspects of the catheterized bladder. Notably, the results have been impacted by an unrealistic biochemical environment. The LB media utilized to test the sensor response to biofilm growth contains more and different nutrients than are generally present in human urine. This can lead to dramatic differences in how bacteria grow and form biofilms [181], [182]. In addition, the ions present in the solution interact directly with an electrochemical impedance sensor, changing the baseline impedance characteristics. Furthermore, the conditioning layers that form on the electrodes with each solution will be different due to the varying chemical compositions.

The physical environment also impacts the functionality of this system. In particular, a low and constant flow rate has been used previously when characterizing this system. In reality, urination patterns are highly variable, with long periods of no flow separated by periodic voiding [183]. My previous studies using this device have focused on biofilm growth exclusively on the inner lumen of the catheter, where the sensor is placed. While this is the area most commonly colonized by biofilm [168], an indwelling catheter is typically inserted into the bladder where the outer surface is immersed in urine and can become colonized as well. The bladder itself can also be colonized by bacteria [10].

In this chapter, I introduce a synthetic bladder model that I developed to characterize the integrated system in a more realistic environment. This model relies on artificial urine to recreate (1) the biochemical environment for biofilm growth that is more clinically relevant. Artificial urine media has a more realistic concentration of nutrients and ions that should lead to a closer

approximation of clinical biofilm growth. This model also consists of a silicone bladder to recapitulate (2) the physical environment of the catheterized bladder. The bladder with the system inserted forms a flow system that is driven by a programmable peristaltic pump, enabling the system to be studied under variable flow conditions, notably long periods of stagnant flow followed by brief periods of higher flow associated with voiding. The bladder also forms a reservoir with realistic geometry that can be colonized by bacteria. Using this synthetic model, I evaluate each of the key functions of the integrated biofilm management system in a realistic environment. First, I examine biofilm sensing in this model using the prototype. Then, I evaluate the BE-based treatment efficacy. The results from these efforts will help to demonstrate that this is a viable approach for biofilm management in a catheterized bladder as well as facilitate future *in vivo* and clinical studies. In addition, the model developed here can also be utilized as an *in vitro* model for other urinary catheter devices.

I am grateful to Dr. Sangwook Chu for his help designing the realistic bladder model.

4.1 Bacterial Growth Sensing in Realistic Model

Typically, novel catheter anti-infection strategies are evaluated using small portions of the material inoculated with bacteria and are analyzed using traditional imaging or colony counting [123], [184]. Alternatively, murine models of urinary catheterization have been developed, which involve implanting pieces of a catheter in the bladder of a mouse [181], [185]. Rabbit models have also been utilized for evaluating novel urinary catheters [186], [187]. A prominent example of an *in vitro* bladder model was developed by Stickler et al and consisted of a 200 ml glass vessel maintained at 37 °C with a water jacket to study the encrustation of urinary catheters by *Proteus mirabilis* [188]. This model does not fully recreate the geometry of the catheterized bladder, however.

As introduced at the start of this chapter, the bladder model is comprised of a silicone model of the human bladder and artificial urine. Once the Foley catheter with the integrated biofilm management system is inserted, this model recreates several key biochemical and physical characteristics of the catheterized bladder. The impact on impedimetric sensing is explored in detail in this section utilizing this realistic testing platform. This represents a key demonstration of the integrated wireless sensing capabilities with bacterial growth that is more likely to resemble growth in a CAUTI with the sensor electrodes immersed in urine.

This section describes the synthetic bladder model in significant detail. Then, I use this model to evaluate impedance sensing of *Escherichia coli* under two different flow conditions: constant flow and pulsatile flow designed to recreate the variable flow associated with the filling and draining of the artificial urine from the bladder. Combined, these studies support the feasibility of this integrated system for use in bladder environments.

4.1.1 Materials and methods

The modified catheter biofilm management system was evaluated in a synthetic bladder model. Figure 4-1 depicts the synthetic bladder setup, consisting of a 3D-printed silicone human bladder, the inserted modified catheter system, and artificial urine all maintained at 37 °C in an environmental chamber. This synthetic model recapitulates the biochemical environment for bacterial growth via artificial urine, and the programmable peristaltic pump recapitulates the physical flow conditions found in the catheterized bladder. Utilizing artificial urine promotes bacterial growth that is more similar to what is seen in the clinic. This artificial urine media was based on human urine samples and designed to study the growth of urinary pathogens [189].

A 3D-printed silicone model of the human bladder (Lazarus 3D) recreates the physical urine storage/flow system where urinary catheters are inserted. This model has a volume of 350

ml, two ureters, and a urethra. The catheter is inserted into the urethra so that urine may drain, and the balloon may be inflated. One ureter serves as a valve to drain the bladder at the conclusion of the experiment, and the other serves as an inlet to introduce artificial urine at a fixed rate. The tubing connected to the bladder is interfaced with a peristaltic pump that drives the flow. The flow can be maintained at a steady rate or programmed to flow in intermittent pulses. The bladder with inserted catheter system, tubing, and media reservoirs are autoclaved (20 min, at 121 °C) to ensure sterilization. 500 ml of artificial urine (Table 4.1) is added to the artificial urine reservoir in a sterile biosafety cabinet. The artificial urine is filtered with a 0.2 µm PES syringe filter (VWR) to prevent contamination. The complete flow system has ports on both the urine and waste reservoirs with syringe filters to maintain sterility and equalize the pressure during flow experiments. The flow system is placed in an environmental chamber at 37 °C to maintain the temperature and minimize the risk of outside contamination. The pump and urine reservoir are connected to the bladder/catheter system via tygon tubing and stored outside of the environmental chamber. The bladder was left overnight to fill with urine, until the catheter was fully immersed, before growth and treatment experiments were performed.

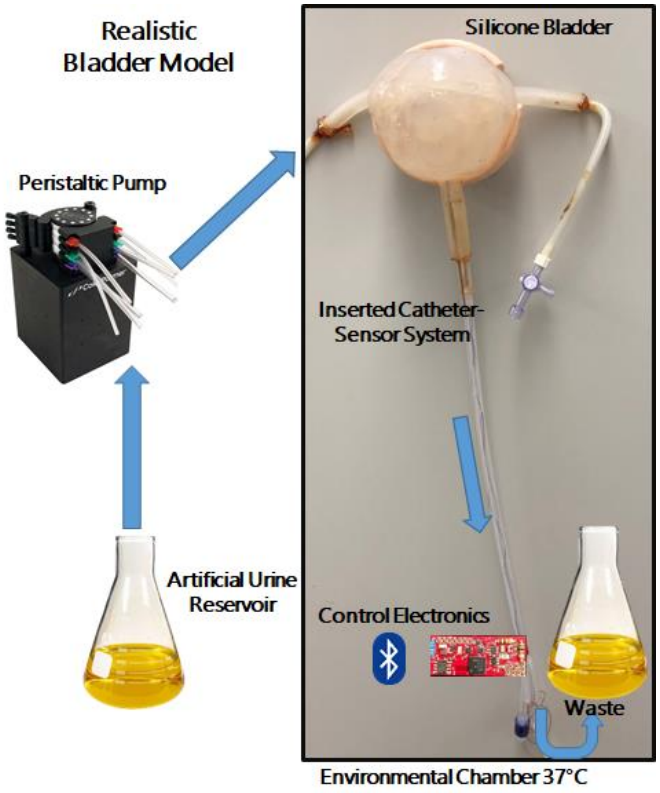

Figure 4-1: Overview of synthetic bladder model setup [169].

Chemical Component	**Concentration**
Peptone	1 g/L
Yeast Extract	5 mg/L
Lactic Acid	100 mg/L
Citric Acid	400 mg/L
Sodium Bicarbonate	2.1 g/L
Urea	10 g/L
Uric Acid	70 mg/L
Creatinine Hydrochloride	900 mg/L
Calcium Chloride Dihydrate	370 mg/L

Sodium Chloride	5.2 g/L
Iron (II) Sulfate	1 mg/L
Magnesium Sulfate Anhydrous	240 mg/L
Sodium Sulfate Decahydrate	3.2 g/L
Potassium Phosphate Monobasic	950 mg/L
Potassium Phosphate Dibasic	1.2 g/L
Ammonium Chloride	1.3 g/L

Table 4-1: Composition of artificial urine for bladder model. Artificial urine was made using deionized water [169].

Biofilm detection experiments were performed using the aforementioned bladder model. An *Escherichia coli* K12 W3110 bacterial culture was prepared in 5 ml of artificial urine and cultured overnight (37 °C, 120 rpm) in an incubator shaker (Brunswick Instruments). A 1:100 dilution of this culture was then grown overnight and diluted relative to artificial urine without any bacteria added. 1 ml of this solution at a dilution of $OD_{600nm} = 0.05$ was added to the system at the start of the experiment. An initial measurement at t = 0 was taken using the mobile application immediately before adding the bacteria. Control samples were made without any bacteria added and 10 µg/ml gentamicin to ensure that there was no contamination throughout the experiment. For the constant flow samples, continuous measurement of the impedance was performed every 30 min throughout the growth period. Measurements for the pulsatile flow samples were taken every 10 min for 10 hours. The change in impedance was recorded as a percentage relative to the initial impedance value (equation 2.1) to account for small discrepancies between the starting raw impedance values of different sensors. Another end-point impedance value was recorded after 24 hours of growth. The adhered biomass was determined using a crystal violet absorbance assay at the conclusion of the pulsatile flow experiment. This consisted of filling the catheter and insert

completely with 0.1% crystal violet solution. The crystal violet was bound with the biofilm material on the surface of the catheter and insert for 15 min. The solution was then drained from the catheter and the system was then rinsed with 10 ml of deionized water to remove excess stain. The insert was carefully removed from the catheter and immersed in 35 ml of decomplexation solution (1 acetone: 4 ethanol) for 35 min. The decomplexation solution dissolved the bound stain, and the OD_{590nm} of the resulting solution corresponds to the relative biomass adhered on the insert with and without biofilm.

One-way ANOVA was performed to evaluate the significance of the impedance sensing results.

4.1.2 Impedance sensor characterization in synthetic model

Figure 4-2 (a) is a representative plot of the impedance change recorded every 30 minutes for 24 hours with *Escherichia coli* added under constant artificial urine flow of 7 ml/h using the realistic bladder model. The impedance decrease is initially more rapid immediately following the addition of the bacteria at t = 0 and then slows after the first 6.5 hours. The relative percentage impedance change decreases by approximately 4.2% over the first 6.5 hours for a rate of -0.65%/h. The decrease then slows, decreasing an additional 2.4% over the next 17.5 hours for a rate of -0.14%/h. This parallels the growth of the bacteria, with a rapid exponential growth phase followed by a plateau [190]. The end-point impedance sensing results show a 13.0% decrease when bacteria are added versus a 5.4% increase for the negative control (Figure 4-2 (b)), demonstrating the viability of this system as a detection tool for the presence of bacteria on an inserted urinary catheter in an artificial urine environment. This trend is similar to what was seen in previous sections in standard LB media; the reduced magnitude and rate of the impedance change in this work is attributed to the lower concentration of nutrients in artificial urine, leading to decreased

bacterial growth. The decrease in impedance seen in Figure 4-2 arises due to the metabolism of growing bacteria on and near the surface [15]. An important consideration for this work moving forward is relating the magnitude of impedance change to real CAUTI outcomes, to identify a threshold that is truly indicative of infection. This should include a calibration curve to equate the average impedance change with the bacterial concentration on the surface, as well as biomass. The slight increase seen in the bacteria-free negative control is due to the formation of small bubbles on the sensor surface over time, which is driven by the temperature difference between the bladder model (37 °C) and the artificial urine reservoir (room temperature) [189]. The bubbles do not interact with the sensor when bacteria are present due to a layer of biofilm forming on the surface.

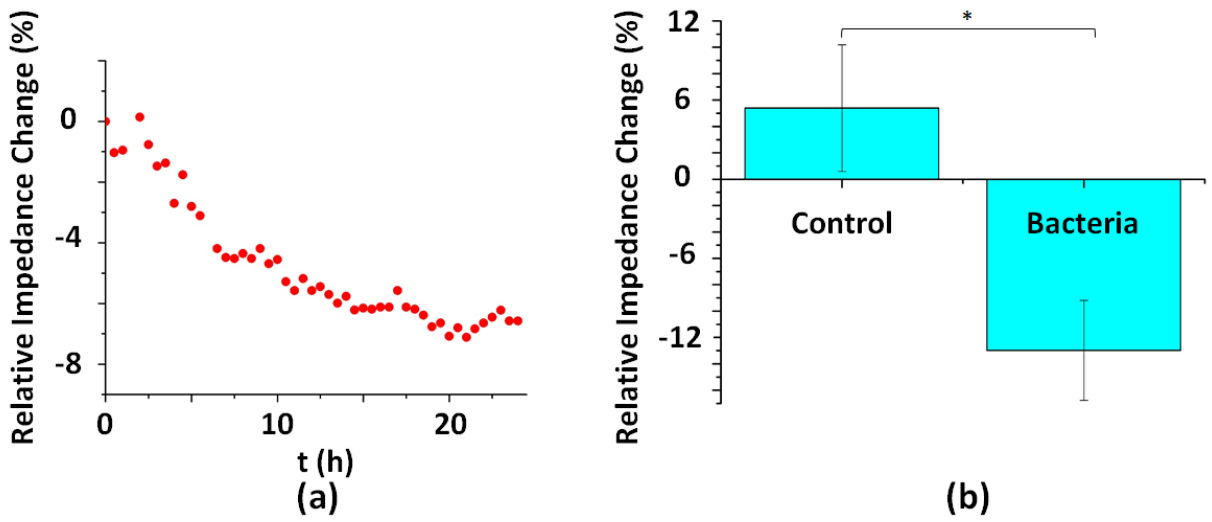

Figure 4-2: (a) Representative real-time relative change in 2 kHz impedance, showing decrease during bacterial growth. (b) End-point relative change in impedance after 24 hours of growth. Control N = 3, Bacteria N = 8, *Significance P<0.05 [169].

4.1.3 Impedance sensor characterization under pulsatile flow

The synthetic bladder model can be utilized to recreate both the biochemical and physical characteristics of the catheterized bladder. Figure 4-3 (a) presents a representative sample of the

impedance recorded every 10 minutes for 10 hours while the sample was subjected to a pulsatile flow pattern that mimics periodic filling of the bladder, followed by catheter drainage. The catheter remained filled with artificial urine throughout the experiment. However, 21 ml flowed every three hours in a pulse, with a flow rate of 5 ml/min, allowing the system to be evaluated under realistic and variable flow conditions. The sample initially displays a higher degree of variability in the impedance change, which is attributed to the lack of a significant biofilm on the surface and inconsistent growth stemming from the static flow between drainage events. However, over time the signal becomes more consistent. The impedance decreases approximately 10.8% over the 10-hour period shown in Figure 4-3 (a). The end-point results in Figure 4-3 (b) display the relative change in impedance after 24 hours of pulsatile flow. The relative decrease in impedance of approximately 20.0% for the samples with bacterial growth compared to a 4.3% increase for the negative control confirms that this system reliably functions as an impedance sensor for monitoring bacterial growth in urinary catheters under realistic flow conditions. The crystal violet absorbance assay adhered biomass measurements in Figure 4-3 (c) further corroborate this implication, demonstrating a correlation between the impedance decrease and an increase in biofilm growth. These results imply that the system functionality is maintained under the variable and realistic flow patterns that may be found in the catheterized bladder.

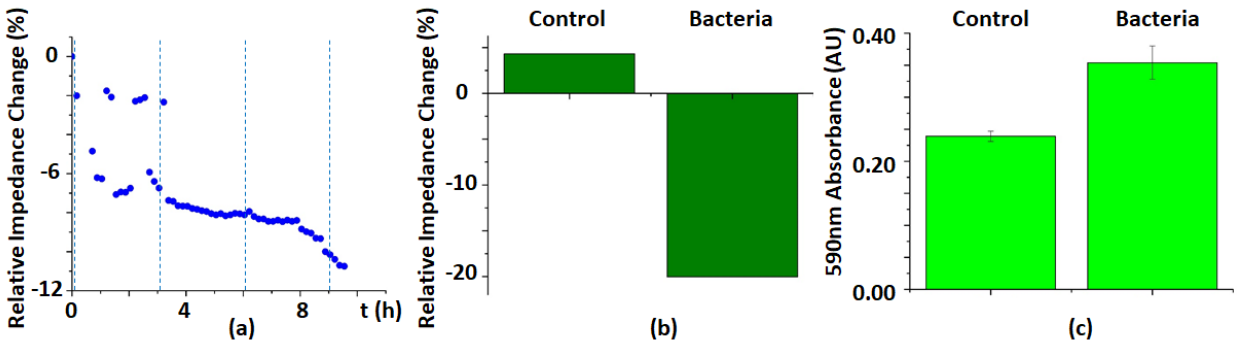

Figure 4-3: (a) Representative real-time 2 kHz relative change in impedance, showing decrease with bacterial growth under pulsatile flow conditions. Dashed blue lines correspond to flow pulses. (b) Representative end-point relative change in impedance for bacterial growth and control samples under pulsatile flow. (c) Biomass staining corresponding to samples with and without bacteria under pulsatile flow, showing a correlation between increased biomass and decreasing impedance (N = 2) [169].

This set of studies demonstrates that these impedimetric sensors function in artificial urine comparably to LB media. Furthermore, variable flow patterns do not significantly alter this function. It is notable that the magnitude of these changes are smaller, but this is primarily attributed to differences in growth by bacteria in each solution. *In vitro* studies like this are invaluable to decrease the risk associated with this approach before time, labor, and cost-intensive *in vivo* or clinical trials are undertaken.

4.2 BE Treatment Efficacy

An essential function of this system is the effective treatment of biofilm once growth has been identified. To achieve this goal and help reduce the incidence of CAUTI, this system can be utilized to administer the BE. The BE can reduce the dosage of antibiotics needed for infection clearance and mitigate the spread of antibiotic resistance. The catheterized bladder environment presents a significant challenge for implementing this approach. The electric field interacts with all of the components of the urine, and electrochemical generation of reactive compounds may play a role in the efficacy of the BE. For this reason, changing the media could change the efficacy of the treatment. As noted previously, the different media changes how the bacteria grow, which can also change their susceptibility to treatment.

In this section, I examine the efficacy of the BE utilizing the integrated catheter system in the synthetic bladder model described in the first half of this chapter. I examine both the planktonic

cell counts and biomass adhered to the sensor surface to quantify the impact of the BE under these realistic conditions.

4.2.1 Materials and methods

After this growth period, one of four different conditions were set for the treatment period: (1) no additional treatment (untreated and unseeded negative control), (2) 10 µg/ml gentamicin and continuous 650 mV, 20 kHz AC signal (BE), (3) 10 µg/ml gentamicin (antibiotic-only), and (4) continuous 650 mV, 20 kHz AC signal (electric field-only). After the treatments had been applied for 24 hours, the end-point impedance was measured using the mobile application and recorded relative to the impedance at the start of the treatment period. At each end-point, the planktonic cell counts were recorded by taking approximately 0.5 ml from the outlet, performing a serial dilution, and counting the CFU/ml on agar plates. The CFU/ml change due to each treatment was determined relative to the CFU/ml found at the beginning of the treatment period, to evaluate the impact that each treatment has on the growth of planktonic bacterial cells. The adhered biomass was determined using the CVS assay described in section 4.1.1. This consisted of filling the catheter and insert completely with 0.1% crystal violet solution. The crystal violet was bound with the biofilm material on the surface of the catheter and insert for 15 min. The solution was then drained from the catheter and the system was then rinsed with 10 ml of deionized water to remove excess stain. The insert was carefully removed from the catheter and immersed in 35 ml of decomplexation solution for 30 min. The OD_{590nm} of the resulting solution corresponds to the relative biomass adhered on the insert for each of the treatment conditions, to determine the efficacy with regards to biofilm reduction.

One-way ANOVA was performed to evaluate the significance of the biomass quantification and CFU/ml results.

4.2.2 BE treatment efficacy

Following the growth of bacteria in the catheterized bladder model for 24 hours, this system enables BE-based treatment to remove biofilms adhered to the catheter surface. The resulting biofilm biomass at the end of 24 hours of treatment was evaluated using a crystal violet absorbance assay (Figure 4-4 (a)), showing highest optical density for untreated samples (OD_{590nm} = 0.333±0.017). This degree of biofilm formation was comparable to those samples treated with gentamicin-only or electric field-only (OD_{590nm} = 0.332±0.027 and OD_{590nm} = 0.324±0.025, respectively). This result for biofilm in artificial urine is consistent with previous *in vitro* results demonstrating that an electric field with this intensity, or gentamicin at this concentration, has limited efficacy for biofilm reduction. Furthermore, the BE (i) showed significantly ($P<0.05$) lower biomass (OD_{590nm} = 0.278±0.010) than the untreated (ii) samples, displaying a synergistic reduction in biofilm using this system. This contrasts with the relative ineffectiveness of the gentamicin (iii) and electric field (iv) treatments for reducing biofilm. The negative control (v) measurement (OD_{590nm} = 0.261±0.024) served as a baseline for comparison; the relatively high baseline signal is driven by precipitates which form in the artificial urine media at 37 °C [189]. It should be noted that the biomass quantification focused on the sensor insert where the electric field was present. The efficacy of this approach would likely improve by having the electrodes act on a higher percentage of the vulnerable surface.

In addition to biofilm biomass evaluation, the change in CFU/ml during each of these treatments was also examined in Figure 4-4 (b). It is important to consider both, as planktonic cell growth and surface-associated biofilm growth contribute to CAUTI. Expectedly, the planktonic bacterial counts rose significantly over the 24 hours of treatment for untreated samples (ii). Similarly, the electric field-treated samples (iv) showed an increase in bacterial cells comparable

to the untreated control, as the electric field only acts on a small portion of the catheter surface and is shown to have limited impact on cell viability [17]. Gentamicin-only (iii) shows a significant ($P<0.05$) decrease in planktonic cells relative to the untreated samples, as these cells are not as tolerant of antibiotic therapy as cells in a biofilm are. The BE (i) shows the most significant ($P<0.05$) reduction in planktonic cells relative to the untreated samples, changing from an increase of 1.19×10^7 CFU/ml for the untreated samples to a decrease of 3.08×10^6 CFU/ml for the BE samples. This is attributed to the combined impact of the antibiotic on the planktonic cells and the synergistic impact of the electric field and gentamicin on the biofilm on the insert surface. It is essential to address both surface-associated and planktonic bacterial growth when developing tools for CAUTI management. In this case, both the surface associated biomass and planktonic bacteria show significant reductions with the BE application. These results, in combination, demonstrate this integrated system as a viable approach for applying the BE in the catheterized bladder environment and reducing the impact of *Escherichia coli* infection. As was mentioned at the conclusion of section 4.1, it is important to perform these *in vitro* studies under realistic conditions to better identify potential pitfalls and risks for future implementation of this system in a clinical or *in vivo* setting. These results suggest that the BE may be a viable strategy for this application; however, additional research needs to be performed for other antibiotics and organisms that are more relevant for CAUTI, such as trimethoprim-sulfamethaxole and uropathogenic *Escherichia coli*, respectively [137], [191].

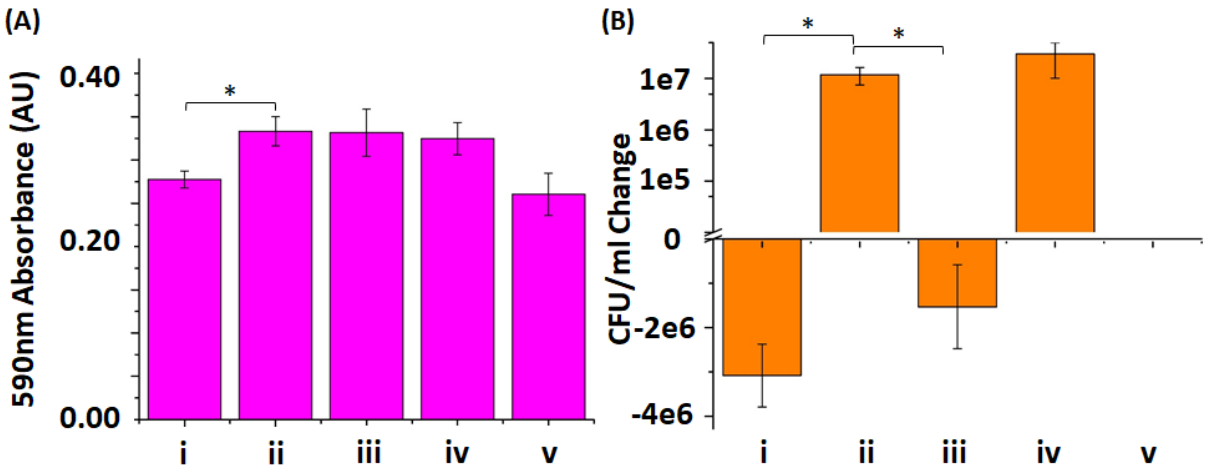

Figure 4-4: (a) End-point biomass staining corresponding to each treatment after the 24-hour treatment period and (b) the change in CFU/ml for each treatment during this period. This shows the lowest biomass for the BE treatment, as well as the largest decrease in CFU/ml. i- BE treated samples (N = 3 (a), N = 3 (b)), ii- untreated samples (N = 3 (a), N = 3 (b)), iii- gentamicin-only treated samples (N = 3 (a), N = 3 (b)), iv- electric field-only treated samples (N = 3 (a), N = 3 (b)), and v- negative control without bacteria (N = 4 (a), N = 3 (b)). *Significance $P<0.05$ [169].

4.3 Synopsis/Summary

In this chapter, I developed a synthetic bladder model for evaluating the performance of the integrated biofilm management system. This model, comprised primarily of a silicone bladder and artificial urine, recreated many of the biochemical and physical characteristics that this system would encounter *in vivo*. I demonstrated impedance sensing of bacterial growth using this system in the synthetic model under both constant and variable flow conditions. Subsequently, I was able to treat these biofilms under realistic conditions using the BE, showing significant reduction in both adhered biomass and planktonic cells. Taken together, the contributions from this chapter support the feasibility of this approach for use in future studies *in vivo* or in the clinic.

Chapter 5: Concluding Remarks

5.1 Highlights

There were several highlights associated with the fabrication and testing of proof-of-concept flexible sensor electrodes for biofilm detection and BE-based treatment described in chapter 2: (1) I fabricated IDEs on a flexible polyimide substrate that seamlessly conforms with a cylindrical catheter surface, (2) I demonstrated real-time impedimetric sensing of biofilm growth on a cylindrical surface, and (3) I correlated the application of the BE using the flexible device with a reduction in strongly adhered biomass.

Another highlight from chapter 2 was the evaluation of the impact of varying curvature on impedance sensor performance. I (1) compared impedimetric sensing and BE treatment *in vitro* at three different curvatures and (2) examined the sensor response of electrodes in planar and cylindrical conformations using commercial simulation software.

There were several key highlights from the integration of electrodes with the commercially-available Foley catheter for biofilm monitoring. I developed two different strategies for electrode integration with urinary catheters: (1) a 3D-printed insert containing flexible electrodes and (2) direct plating of electrodes onto urinary catheters. In addition, I verified that the standard catheter functions are maintained with the integrated device and evaluated the biocompatibility of 3D-printed insert materials.

The development of the electronic systems for control of integrated biofilm management device also yielded several highlights. I (1) demonstrated detection of biofilm using off-the-shelf electronic components, (2) developed a miniaturized PCB for wireless detection, treatment, and data transmission, and (3) developed a mobile application that enabled user-friendly system control and data display.

There were a number of highlights associated with the testing of the integrated system for monitoring and treatment in a realistic *in vitro* bladder model. I (1) assembled a realistic laboratory model of the catheterized bladder for *in vitro* system evaluation, demonstrated real-time impedimetric sensing of bacterial growth under realistic conditions using the integrated system, and utilized the integrated system in the bladder model to effectively implement the BE.

5.2 Summary

This dissertation presents the development of an integrated, microsystems-based approach for addressing the challenge of CAUTI. The progression from a proof-of-concept device to an integrated system in a realistic laboratory bladder is illustrated in Figure 5-1. I adapted a previously developed LOC biofilm characterization platform using a flexible substrate in Chapter 2, allowing the electrodes to be conformed on the inner lumen of a catheter while maintaining functionality. This device detected biofilm growth in real-time through impedimetric sensing. The same electrodes were then utilized to achieve a reduction in adhered biomass via the BE. Chapter 3 then described the integration of this device with a commercially available Foley catheter. Two different approaches were explored: (1) a 3D-printed insert module containing the flexible sensor integrated with the catheter at a transverse cut and (2) plating electrodes directly on the surface of the catheter. In addition to the physical integration of the electrodes, the development of the associated electronic systems was described in this chapter. This included a PCB for wireless sensing and treatment using off-the-shelf components and the mobile application. Combined, the PCB, mobile application, and integrated electrodes comprise the integrated catheter biofilm management system. In Chapter 4, this integrated system is tested in a custom synthetic bladder model to carefully evaluate the sensing and treatment functions under realistic conditions. The result is an integrated system that can support future research *in vivo* and in a clinical setting towards improved management of bacterial infections, notably CAUTI.

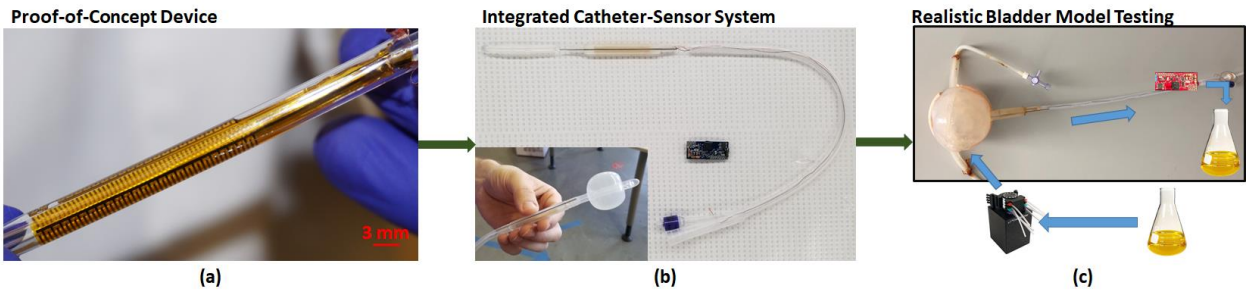

Figure 5-1: Illustration of system development in this dissertation from (a) proof-of-concept device to (b) integration with Foley catheter to (c) evaluation of sensing and treatment under realistic conditions.

In Chapter 2, I developed a proof-of-concept biofilm sensing and treatment device and explored the impact of curvature on device performance. Notably, I fabricated IDE sensors capable of detecting biofilm formation using a flexible polyimide substrate. This substrate allowed the electrodes to be conformed in a cylindrical shape while maintaining the real-time sensing and BE treatment capabilities displayed in previous LOC systems [16]. Sensing was confirmed with significant differences in the impedance change with and without biofilm-forming bacteria and correlated with the adhered biomass. The reduction in biofilm via the BE was also confirmed via the decrease in adhered biomass relative to the controls without treatment, with only antibiotics, or with only the electric field. I utilized COMSOL modelling software and flexible sensors conformed at specified curvatures to investigate the impact that curvature has on these devices. In both cases, the change between planar and curved showed relatively little impact at the size scale that is relevant for urinary catheters, and this appeared to be true for both sensing and treatment. At a radius of curvature of 2.25 mm, the electric field distribution remained relatively unchanged.

The device developed and evaluated in Chapter 2 was integrated with a urinary catheter in Chapter 3. Two different methods were investigated to achieve this goal. I developed a 3D-printed insert that accommodates the urine drainage and anchoring balloon inflation channels to ensure the proper catheter function was maintained. This insert housed the flexible sensor, which was

integrated with the catheter at a transverse cut near the distal tip. This approach allowed me to introduce the electrodes onto the vulnerable area of the catheter without altering the established design. I confirmed that the catheter maintained functionality by verifying liquid drainage and balloon inflation with the device integrated. I also evaluated the biocompatibility of the 3D-printed insert material to help ensure the safety of this technique for indwelling devices. As an alternative approach, I developed a fabrication process which relied on electroless plating with 3D-printed patterning scaffolds to produce isolated electrodes on the surface of a urinary catheter. SEM and EDS analysis confirmed that this process yielded a pair of electrodes on a section of a Foley catheter. These electrodes displayed impedance sensor performance that was comparable to flexible electrodes from Chapter 2 when exposed to *Escherichia coli*. The insert approach was utilized for subsequent experiments as it displayed better sensitivity due to the IDE electrode arrangement. An essential element of this system was the PCB and mobile application that were developed to provide user-friendly control and facilitate implementation by future researchers and clinicians. The developed PCB relied on COTS components to achieve wireless impedance sensing for biofilm detection and electric field generation for the BE in a small form factor that could be attached to the drainage bag of the catheter with minimal disruption for patients and healthcare practitioners. A mobile application was designed specifically to interface with this PCB, enabling seamless control over each of the functions as well as the data readout without specialized training.

After the integrated system was developed, I investigated the use of this system under realistic bladder conditions. Artificial urine recreated the biochemical aspects of the bladder environment, while a 3D-printed silicone bladder with flow, controlled by a programmable peristaltic pump, recreated the physical aspects of this environment. Both the impedimetric sensing and BE treatment functions were explored under these conditions. I found that there was a real-

time decrease in impedance associated with the addition of bacteria in this environment. While the trend was similar to the results from earlier chapters, the magnitude of the change was smaller due to decreased bacterial growth in the bladder setting relative to LB media. Future trials utilizing this system should focus on relating this change to real CAUTI outcomes, to help identify a threshold that is indicative of clinically relevant infection. The biofilm impedance sensing results in the realistic model were consistent under constant and variable flow. When the integrated system was utilized to administer the BE in the bladder model, I was able to show a decrease in both planktonic bacteria via colony counting and adhered biomass via CVS compared to untreated samples. This study forms the foundation for future research by demonstrating the feasibility of this system under realistic conditions.

5.3 Future Work

This dissertation project has laid the groundwork for new research directions that can be explored in the short- and long-term. These include enhancing the functionality of the system through sensor arrays, incorporating additional sensing modalities, and evaluating the system *in vivo* or in a clinical setting. Furthermore, this approach can be applied to many other applications that are susceptible to bacterial colonization, such as water systems and vascular catheters.

5.3.1 Flexible electrode array for biofilm mapping on cylindrical surfaces

The IDE-based impedance sensor provides a single readout for the entire surface. This provides significant utility for identifying general changes in the solution and on the surface. However, biofilm growth is spatially heterogeneous [192], including on the surface of urinary catheters [168]. As a research tool, it would be beneficial to improve the special resolution of this system by utilizing an array of IDEs distributed along the catheter surface. Such a system can indicate the precise location of biofilm formation, which can help direct subsequent device design changes to address specific problem areas or highly targeted regions of treatment. Towards this

end, I adapted the flexible device concept from Chapter 2 into an array device with 8 spatially distinct sets of IDEs.

The electrodes were fabricated on a flexible 25.4 µm-thick polyimide film that can be rolled and inserted to display the sensor surfaces on the interior of the urinary catheter. The fabrication process is displayed in Figure 5-2. In brief, electrodes were patterned via a transparency photomask (Figure 6-3 Appendix A) using photolithography. Metal (20 nm chromium/200 nm gold) was deposited via e-beam deposition, and liftoff in acetone formed the interdigitated electrodes (300 µm width/spacing). The non-sensing areas were passivated with 2.5 µm of Parylene-C, which was removed from the sensor IDEs using protective polyimide tape. This final device (Figure 5-3) was comprised of eight interdigitated impedance sensors distributed over a 40 mm x 14 mm footprint.

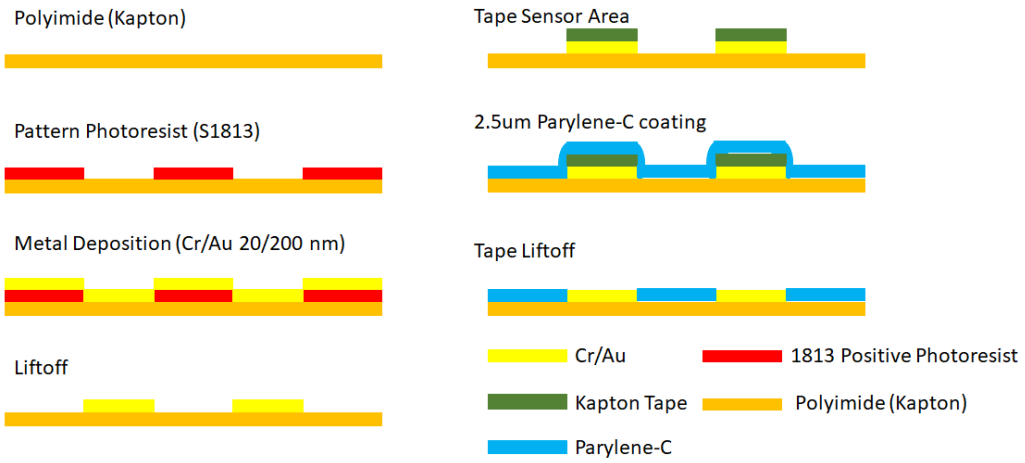

Figure 5-2: Fabrication process flow for producing flexible array sensor.

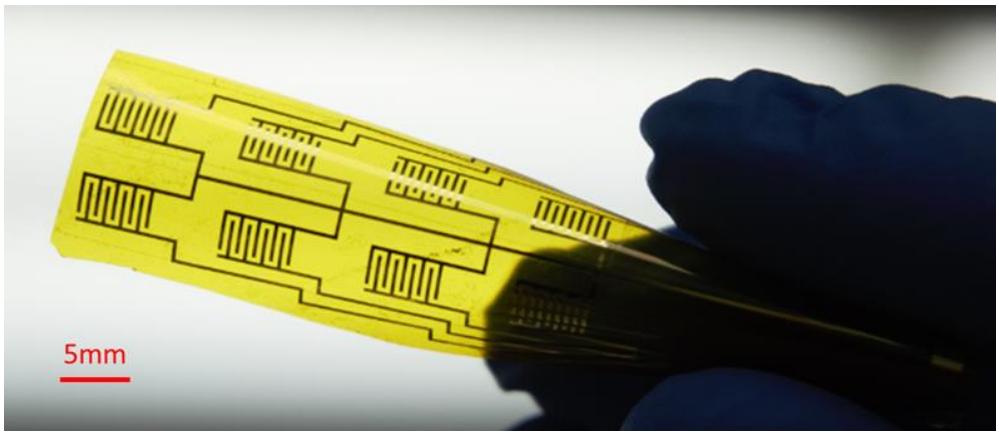

Figure 5-3: Optical image depicting fabricated sensor array on flexible polyimide film. The sensor consists of eight gold IDEs with a common ground.

This system can be evaluated *in vitro* using the same setup utilized to characterize the flexible device in Chapter 2. Array devices like this should facilitate more detailed research into how biofilm grows on catheters and enable more precise interventions.

5.3.2 Multimodal sensor system

In addition to biofilm, there are numerous factors that contribute to and can help identify CAUTIs. An effective system for predicting CAUTI and negative infection outcomes should consider a panel of parameters to provide a more precise diagnosis and allow more effective treatment. These parameters include temperature, pH, and host inflammatory cytokines. An increase in body temperature, fever, is associated with CAUTI [193]. Changes in urine pH can be related to the formation of biofilm by *Proteus mirabilis*, which can lead to the development crystalline blockages in the catheter [10]. Inflammatory cytokines, such as interleukin 6, are also secreted during infection, making them a reasonable target for CAUTI detection [194].

A schematic of a pH, temperature, cytokine, and biofilm sensor integrated onto a single substrate is shown in Figure 5-4. Employing electrochemical sensors for pH [195], biofilm, and cytokines [196], as well as a resistive temperature sensor [197] facilitates integration of these

devices with electronic control systems that process electrical output signals. Further research is needed to more accurately assess the potential biomarkers associated with CAUTI and negative CAUTI outcomes, like pyelonephritis and sepsis. This research will undoubtedly guide the biomarker targets that this multimodal sensor system will be designed to detect. The cytokine sensor, particularly, can be easily modified by changing the biorecognition element affixed to the electrode surface.

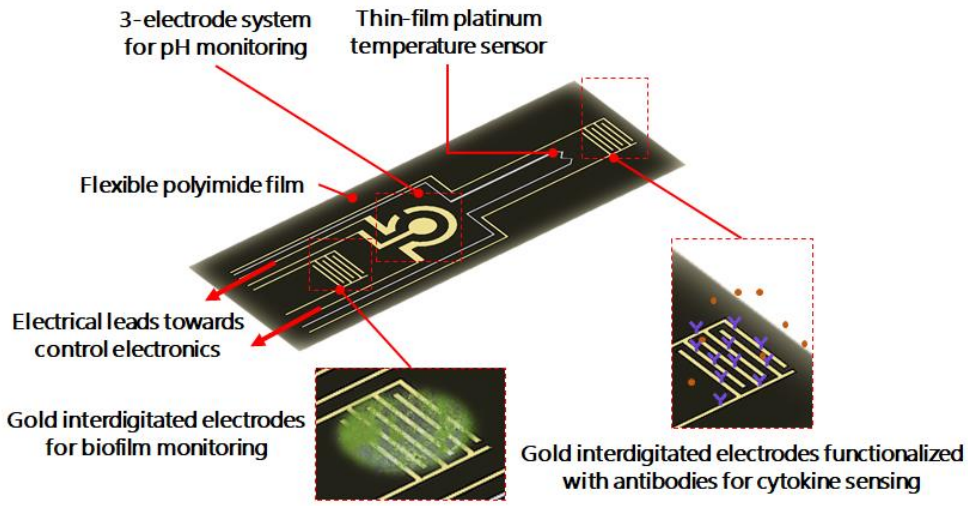

Figure 5-4: System schematic depicting multimodal sensor system with four different sensors for temperature, cytokines, biofilm, and pH, respectively.

The development of a multimodal catheter-integrated sensor system will facilitate the acquisition of a diverse array of real-time and *in situ* data that is currently not available to CAUTI researchers. This system will be a focus of a collaborative National Institutes of Health RC2 proposal between engineers in the Ghodssi group at the University of Maryland, College Park, Dr. Rena Malik, a urologist at the University of Maryland Medical School, and microbiologists Dr. David Rasko at the University of Maryland, Baltimore and Dr. Vincent Lee at the University of Maryland, College Park. The large quantity of data generated with this discovery platform can be analyzed using machine learning algorithms to identify new biomarkers indicative of CAUTI and

negative CAUTI outcomes. The data analysis portion of this project will be supported by Dr. Olga Goloubeva at the University of Maryland, Baltimore and Dr. Najib El-Sayed at the University of Maryland, College Park with expertise in biostatistics and bioinformatics, respectively.

5.3.3 Biofilm sensing in clinical urine

It is invaluable to evaluate the performance of the biofilm sensor in clinical urine samples from patients with indwelling catheters, as this will more accurately represent the conditions in a clinical setting or *in vivo*. The impedance sensor response to biofilm growth in clinical urine samples was evaluated with help from Anthony Chung using previously developed IDEs [16], which were integrated within a PDMS microfluidic channel (2 cm x 500 µm x 100 µm). A microfluidic device was used for this characterization, as the sample sizes were limited and insufficient for use with the bladder model in Figure 4-1. Patient urine samples were acquired from healthy, catheterized patients at the clinic of Dr. Rena Malik from the University of Maryland Medical School. These samples were frozen and transferred to the MEMS Sensors and Actuators Lab where they were stored at -80 °C. Prior to the experiments, the microfluidic systems were sterilized with 1 ml 70% ethanol flowed through the device at 100 µl/min using a syringe pump (Cole Parmer, 74900), followed by 5 ml of DI water at the same flow rate. The conditioning phase consisted of artificial urine being introduced into the device at 20 µl/h for 24 hours. This period allowed the formation of a conditioning layer and flushed any air bubbles out of the system. Patient urine was thawed and filtered with a 0.2 µm syringe filter (polyethersulphone, VWR) to prevent uncontrolled contamination by any bacteria already present in the sample. *Escherichia coli* K12 W3110 were cultured from frozen in LB media overnight in an incubator shaker (Brunswick Scientific) at 250 rpm and 37 °C. The bacteria were then diluted to an OD_{600nm} of 0.25 in the filtered patient urine. The urine sample spiked with bacteria was introduced into the microfluidic device at a flow rate of 100 µl/min. As a control, a urine sample without any bacteria added was also

introduced in another microfluidic device in parallel. Once the sample had filled the device, the flow was stopped, and the bacteria were allowed to attach within the device for the 2-hour seeding phase. Following the conclusion of the seeding phase, filtered patient urine without added bacteria was introduced into the device at a flow rate of 20 µl/h for 24 hours for the growth phase. Throughout the experiment, the impedance at 100 Hz and 5 mV was recorded using a potentiostat (660D, CHInstruments). The entire system was contained within an environmental chamber (Electro-Tech Systems, 5506) at 37 °C. Immediately following the growth phase, the sample was stained with LIVE/DEAD stain in tris buffer, prepared as described in Chapter 3. The stain was introduced into the channel at a flow rate of 20 µl/h for 18 hours so as not to disturb the attached biofilm. The sample was then rinsed with tris buffer at 20 µl/h for 24 hours to remove unbound stain. The samples were then imaged using a confocal microscope (LSM 700, Zeiss) to correlate the presence of biofilm with the impedance change.

A representative sample, spiked with *Escherichia coli*, showed a notable decrease in 100 Hz impedance over the 24 hour growth period (Figure 5-5). The impedance decreased approximately 8% over the first 12 hours, followed by a plateau. However, the control channel without any bacteria added also showed an impedance decrease of approximately 8%. These decreases are attributed to the fouling of the electrode by host proteins [10]. Only a small biofilm was identified in the microfluidic channel with bacteria added using confocal microscopy (Figure 5-6). This aggregate of cells was sparse and mostly dead, as indicated by the dominance of the propidium iodide in the image. This likely contributed to the similarity between the control and biofilm samples. Additional tests are needed to investigate these preliminary results in the future.

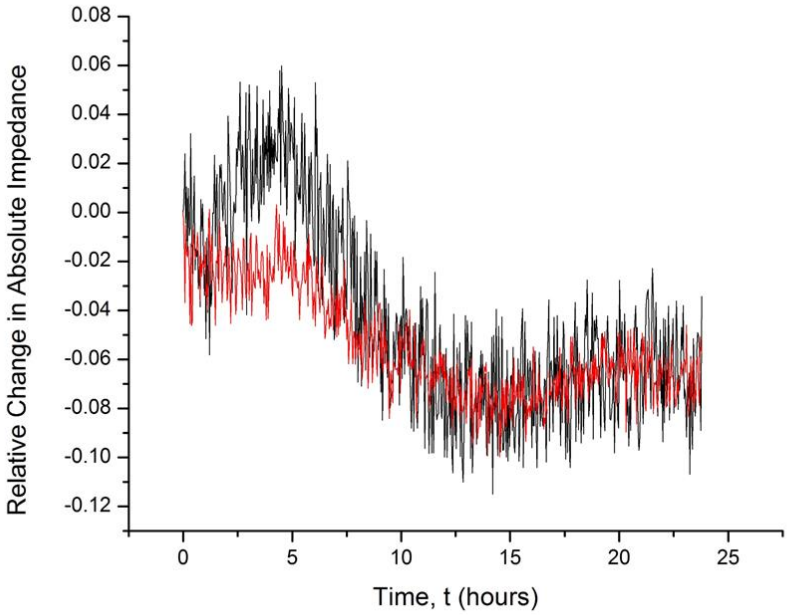

Figure 5-5: 100 Hz, 5 mV impedance transients depicting relative change in impedance over the course of the 24-hour growth period. The black line corresponds to the sample with bacteria added, and the red line corresponds to the control sample.

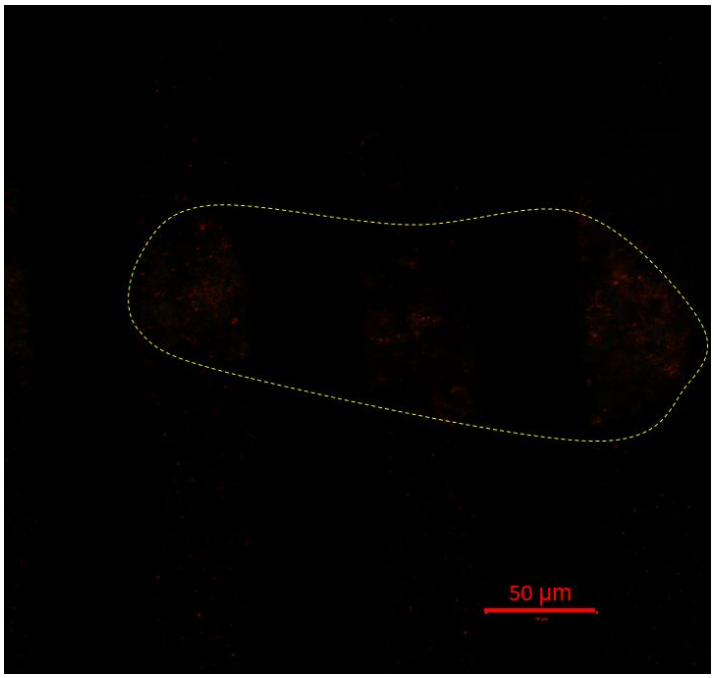

Figure 5-6: LIVE/DEAD stain identifying biofilm growth in microfluidic channel. Dark areas correspond to electrodes. Area encircled in yellow is the sparse biofilm aggregate.

5.3.4 Additional environments vulnerable to biofilm colonization

The system developed in this work has the potential to address challenges in many environments beyond urinary catheters. Biofilm presents a significant issue in healthcare [23], food production [198], water systems [199], [200], and marine [201] environments. Notably, it would be relatively straightforward to adapt this system for use in hospital water pipes and sinks, which can lead to outbreaks among vulnerable populations when they are colonized by *Legionella pneumophila* or *Pseudomonas aeruginosa* [202]–[204]. This would simply involve scaling the device to the appropriate dimensions and calibrating it for use in water. I would expect this system to be simpler than that for the urinary catheter, as urine is more variable and there are more design constraints for indwelling medical devices. The sensing and treatment approach could also be adapted for use with indwelling vascular catheters, which are often colonized by biofilm [205]. This would involve scaling down the system, as vascular catheters are typically smaller than urinary catheters. Careful considerations also need to be made as vascular catheters can become occluded due to thrombus formation [206].

5.4 Conclusion

CAUTI remains a widespread challenge in healthcare despite various efforts to reduce its incidence and impact. Microsystem technologies offer a novel approach for both identifying infection risk due to biofilm growth and eliminating biofilm from the surface of a urinary catheter in a small form factor. This dissertation details the development of a microsystem-based biofilm management system from a flexible proof-of-concept device to an integrated system validated under realistic conditions *in vitro*. I utilized a flexible substrate with microfabricated IDEs to achieve real-time detection via electrochemical impedance sensing and administer an electric field

for BE treatment while conformed in a cylindrical catheter shape. I then leveraged commercial microelectronics and 3D-printing to create a functional integrated prototype, which was subsequently evaluated in a customized *in vitro* bladder model. This is the first demonstration of each of these functionalities with respect to CAUTI and indwelling catheters. Importantly, this is the first implementation of a microsystem-based approach for biofilm detection and treatment on urinary catheters. Recent research has typically focused on novel materials and surface modifications. I anticipate that the system investigated in this dissertation can function synergistically with these other strategies to achieve a reduction in CAUTI incidence.

The research in this dissertation has the potential to generate new kinds of data when evaluating CAUTI for future research and in the clinical setting. The real-time, *in situ* information yielded by this device is unique for these infections and can have far-reaching implications for how biofilms are studied in this context. In addition, the *in vitro* testing model represents a viable technique for evaluating future catheter-based devices and systems, thus establishing a methodology for developing future devices in this space. The initial microsystems demonstration in this dissertation serves as the baseline for developing a multitude of different microsystems for addressing CAUTI. Furthermore, this work can have an impact beyond CAUTI. The developed integration strategies can be implemented for an array of microelectronic sensors for various applications involving non-planar surfaces, particularly in healthcare and biomedical research. Overall, the approach developed in this dissertation will facilitate future biofilm research by generating continuous *in situ* impedance sensing data and the integration effort supports the future use of this system in a clinical setting.

6. Appendices

6.1 Appendix A: Photomask Patterns

A.1 Flexible IDEs with 300 µm finger width and spacing

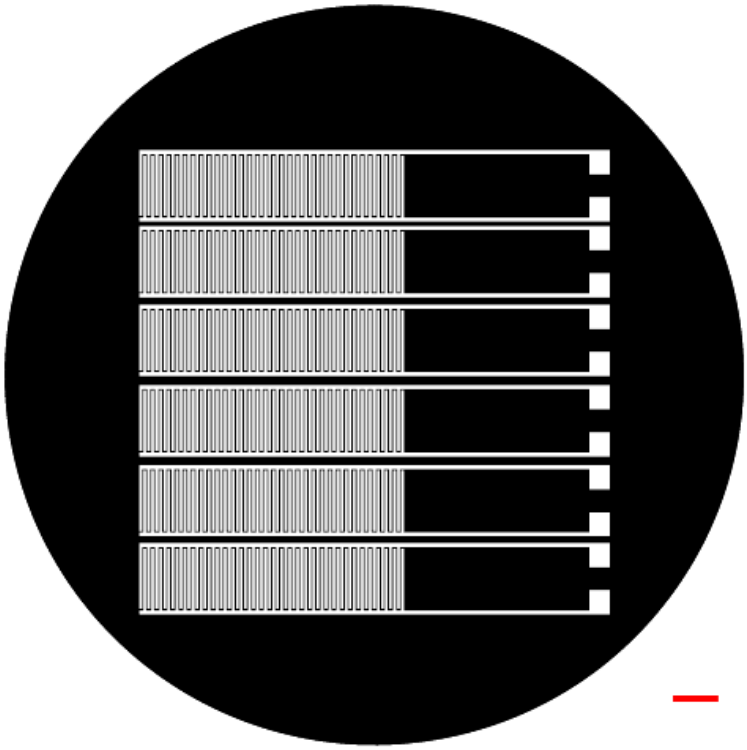

Figure 6-1: Transparency photomask for flexible IDEs. The finger width and spacing is 300 µm over a 10 mm x 40 mm footprint. Leads are an additional 30 mm x 0.5 mm. Contact pads are 3 mm x 3 mm. Scale bar is 5 mm.

A.2 Flexible IDEs used within integrated system

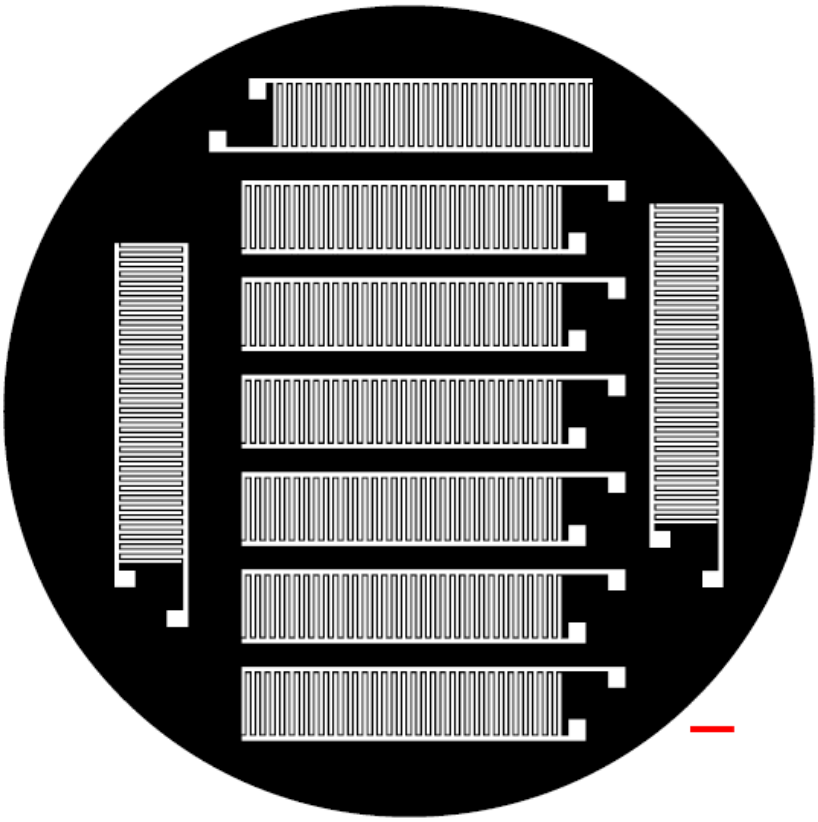

Figure 6-2: Transparency mask for flexible IDEs. Finger width/spacing is 300 µm over a 9.8 mm x 40 mm footprint. Leads 0.5 mm wide, connecting to 2 mm x 2 mm contact pads positioned 0.5 mm or 4.5 mm from the IDEs. Scale bar is 5 mm.

A.3 IDE array device

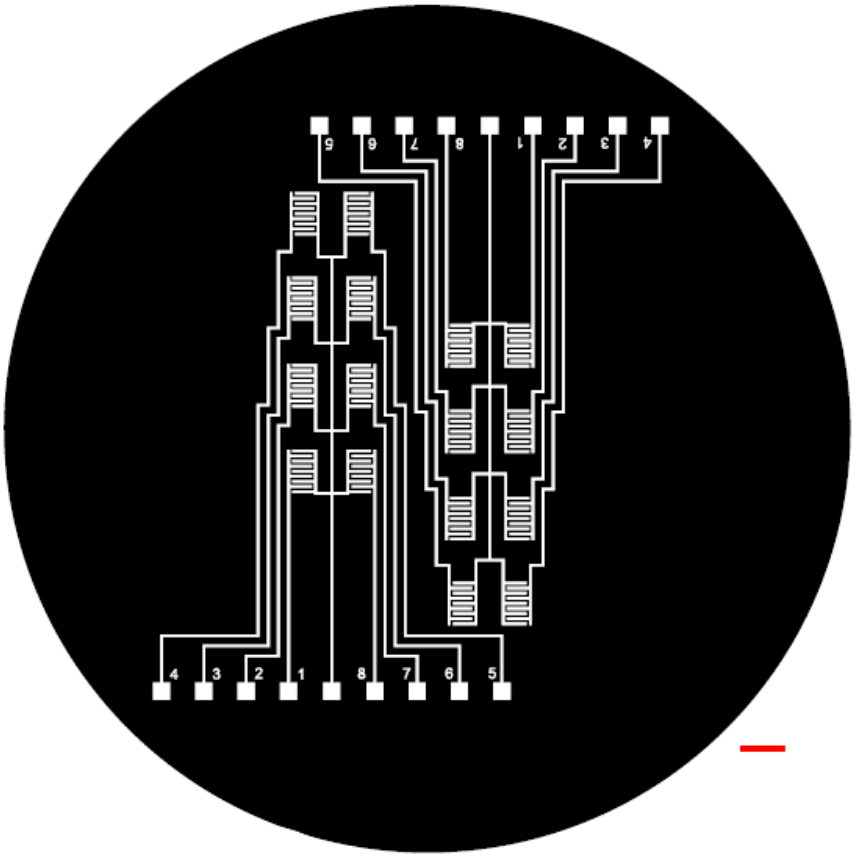

Figure 6-3: Transparency photomask of array device for biofilm mapping. Traces are 300 µm wide and contacts are 2 mm x 2 mm. 8 IDE pairs are evenly spaced over a 9.8 mm x 40 mm footprint with 300 µm finger width and spacing. Each device connects with a common ground. Scale bar is 5 mm.

6.2 Appendix B: Matlab Programs

B.1 EIS Results

```
filepath = 'C:\Users\Ryan\Box Sync\4-channel_4\'; % Enter your data
folder path
filepath_temp = 'C:\Users\Ryan\Box Sync\Temp\'; %Enter filepath for
temp files

startPBS = 1; % start file number of PBS
endPBS = 1; % end file number of PBS

start_date = 27; %enter start date
start_hour = 13; % enter starting hour in 24 hour format
start_min = 10; % enter starting minute

end_date = 27; %enter end date
end_hour = 13; % enter end hour in 24-hour format
end_min = 13; % enter end minute

N= endPBS-startPBS+1; % N= number of txt files/runs of the CHI
M = 60; % M = number of numeric lines in each CHI output text file

Total_time =  (end_date - start_date) * 24 * 60 * 60 + (end_hour -
start_hour)* 60 * 60 + (end_min - start_min) * 60 ; % Calculate total
time in seconds

Time_step = Total_time/(N-1); % average step time in seconds between
two consecutive runs

Time_s = 0: Time_step: Total_time; % create an array called time
Time_h = Time_s/(60*60); % row array of time in hours
Final_time = Time_h'; % column array of time in hours

Final_data = zeros(M,5*N); %size of final data array
Final_realZ = zeros(M,N); %size of final real Z data array
Final_imZ = zeros(M,N); %size of final im Z data array
Final_absZ = zeros(M,N); %size of final abs Z data array
Final_phase = zeros(M,N); %size of final phase of Z data array

j= 1; % counter
column = 1; % counter for column of final arrays
for i = startPBS:endPBS
    filename = [filepath 'endcond' num2str(i) '.txt']; %give path to
files you want to analyze
    fid = fopen(filename, 'r') ;                    % Open source file.
    fgetl(fid) ;                                    % Read/discard line.
    fgetl(fid) ;                                    % Read/discard line.
    fgetl(fid) ;                                    % Read/discard line.
    fgetl(fid) ;                                    % Read/discard line.
    fgetl(fid) ;                                    % Read/discard line.
```

```
    fgetl(fid) ;                                    % Read/discard line.
    fgetl(fid) ;                                    % Read/discard line.
    fgetl(fid) ;                                    % Read/discard line.
    fgetl(fid) ;                                    % Read/discard line.
    fgetl(fid) ;                                    % Read/discard line.
    fgetl(fid) ;                                    % Read/discard line.
    fgetl(fid) ;                                    % Read/discard line.
    fgetl(fid) ;                                    % Read/discard line.
    fgetl(fid) ;                                    % Read/discard line.
    fgetl(fid) ;                                    % Read/discard line.
    fgetl(fid) ;                                    % Read/discard line.
    fgetl(fid) ;                                    % Read/discard line.
    buffer = fread(fid, Inf) ;                      % Read rest of the
file.
    fclose(fid);

    filename2 = [filepath_temp 'endcond' num2str(i) '_TRUNC.txt'];
    fid = fopen(filename2, 'w')  ;   % Open destination file.
    fwrite(fid, buffer) ;            % Save to file without header.
    fclose(fid) ;

    %copy each file content into a temporary array named Temp
    fileID = fopen (filename2, 'r');
    formatSpec = '%f, %f, %f, %f, %f';
    sizeTemp = [5 M];
    Temp = fscanf(fileID, formatSpec, sizeTemp);
    fclose(fileID);
    Transpose_Temp = Temp';

    % Array frequency contains a column array of the frequencies at
which measurements were obtained
    for x=1:M
        Frequency(x,1) = Transpose_Temp(x,1);
        x=x+1;
    end

    %append contents of the array Temp to the final data arrays
    for x=1:M
        shift_y=j;
        for y=1:5
        Final_data(x,shift_y) = Transpose_Temp(x,y);
        y=y+1;
        shift_y=shift_y+1;
        end
    end
    j = j+5; % increment counter by 5 columns

    % Write into individual arrays
    for a=1:M
        Final_realZ(a,column)= Transpose_Temp(a,2);
        Final_imZ(a,column)= Transpose_Temp(a,3);
        Final_absZ(a,column)= Transpose_Temp(a,4);
```

```
        Final_phase(a,column) = Transpose_Temp(a,5);
        a=a+1;
    end
      column = column+1;
end

% plot figure

Avg = mean([Final_data3(:,4) Final_data31(:,4) Final_data32(:,4)],2);
% find average of multiple sweeps

e1 = std([Final_data3(:,4) Final_data31(:,4) Final_data32(:,4)],1,2);
% determine standard deviation of multiple sweeps

e1_2=repmat(NaN,size(e1));
e1_2(1:5:end)=e1(1:5:end);
% only plot every fifth error bar

% Abs Z versus frequency on a log log scale
figure
loglog(Frequency,Avg(:,1), 'r','LineWidth', 2.0)
hold on
errorbar(Frequency,Avg(:,1),e1_2, 'r')
title('Abs Z v. f', 'FontSize',20,'FontWeight','bold')
xlabel('f', 'FontSize',20,'FontWeight','bold')
ylabel('Abs Z', 'FontSize',20,'FontWeight','bold')
set(gca,'fontsize',16,'FontWeight','bold')
print -dpng -r300 AbsZ_vs_Freq
hold off

%delete the _TRUNC temp files in the TEMP folder
 delete('C:\Users\Ryan\Box Sync\Temp\*_TRUNC.txt');
```

B.2 Equivalent Circuit Fitting

```
% Impedance Equivalent Circuit Fitting

% Plot experimental value

filepath = 'C:\Users\Ryan\Box Sync\Biofilm Exp 04102017\'; % Enter
your data folder path
filepath_temp = 'C:\Users\Ryan\Box Sync\Temp\'; %Enter filepath for
temp files

startPBS = 1; % start file number of PBS
endPBS = 1; % end file number of PBS

start_date = 27; %enter start date
start_hour = 13; % enter starting hour in 24 hour format
start_min = 10; % enter starting minute
```

```
end_date = 27; %enter end date
end_hour = 13; % enter end hour in 24-hour format
end_min = 13; % enter end minute

N= endPBS-startPBS+1; % N= number of txt files/runs of the CHI

M = 60; % M = number of numeric lines in each CHI output text file

Total_time =  (end_date - start_date) * 24 * 60 * 60 + (end_hour -
start_hour)* 60 * 60 + (end_min - start_min) * 60 ; % Calculate total
time in seconds

Time_step = Total_time/(N-1); % average step time in seconds between
two consecutive runs

Time_s = 0: Time_step: Total_time; % create an array called time
Time_h = Time_s/(60*60); % row array of time in hours
Final_time = Time_h'; % column array of time in hours

Final_data = zeros(M,5*N); %size of final data array
Final_realZ = zeros(M,N); %size of final real Z data array
Final_imZ = zeros(M,N); %size of final im Z data array
Final_absZ = zeros(M,N); %size of final abs Z data array
Final_phase = zeros(M,N); %size of final phase of Z data array

j= 1; % counter
column = 1; % counter for column of final arrays
for i = startPBS:endPBS
    filename = [filepath 'ch6endseed' num2str(i) '.txt']; %give path
to files you want to analyse num2str(i) removed for this
    fid = fopen(filename, 'r') ;                    % Open source file.
    fgetl(fid) ;                                   % Read/discard line.
    fgetl(fid) ;                                   % Read/discard line.
    fgetl(fid) ;                                   % Read/discard line.
    fgetl(fid) ;                                   % Read/discard line.
    fgetl(fid) ;                                   % Read/discard line.
    fgetl(fid) ;                                   % Read/discard line.
    fgetl(fid) ;                                   % Read/discard line.
    fgetl(fid) ;                                   % Read/discard line.
    fgetl(fid) ;                                   % Read/discard line.
    fgetl(fid) ;                                   % Read/discard line.
    fgetl(fid) ;                                   % Read/discard line.
    fgetl(fid) ;                                   % Read/discard line.
    fgetl(fid) ;                                   % Read/discard line.
    fgetl(fid) ;                                   % Read/discard line.
    fgetl(fid) ;                                   % Read/discard line.
    fgetl(fid) ;                                   % Read/discard line.
    fgetl(fid) ;                                   % Read/discard line.
    fgetl(fid) ;                                   % Read/discard line.
    fgetl(fid) ;                                   % Read/discard line.
    buffer = fread(fid, Inf) ;                     % Read rest of the
file.
    fclose(fid);
```

```
    filename2 = [filepath_temp 'ch6endseed' num2str(i) '_TRUNC.txt'];
%num2str(i)
    fid = fopen(filename2, 'w')  ;    % Open destination file.
    fwrite(fid, buffer) ;             % Save to file without header.
    fclose(fid) ;

    %copy each file content into a temporary array named Temp
    fileID = fopen (filename2, 'r');
    formatSpec = '%f, %f, %f, %f, %f';
    sizeTemp = [5 M];
    Temp = fscanf(fileID, formatSpec, sizeTemp);
    fclose(fileID);
    Transpose_Temp = Temp';

    % Array frequency contains a column array of the frequencies at
which measurements were obtained
    for x=1:M
        Frequency(x,1) = Transpose_Temp(x,1);
        x=x+1;
    end

    %append contents of the array Temp to the final data arrays
    for x=1:M
        shift_y=j;
        for y=1:5
        Final_data(x,shift_y) = Transpose_Temp(x,y);
        y=y+1;
        shift_y=shift_y+1;
        end
    end
    j = j+5; % increment counter by 5 columns

    % Write into individual arrays
    for a=1:M
        Final_realZ(a,column)= Transpose_Temp(a,2);
        Final_imZ(a,column)= Transpose_Temp(a,3);
        Final_absZ(a,column)= Transpose_Temp(a,4);
        Final_phase(a,column) = Transpose_Temp(a,5);
        a=a+1;
    end
      column = column+1;
end

% Abs Z versus frequency on a log log scale
figure
syms x y % Set variables

Rs=37; % Solution resistance (ohms)
Rb=4; % Biofilm resistance (ohms)
Cd=0.000018; % Interfacial capacitance (F)
Cb=0.000012; % Biofilm capacitance (F)
```

```
% Circuit parameter values

x=linspace(10,1000000,1000); % Frequency range and number of points
y=(Rs+Rb+(2./(6.28*x*Cd))+(1./(x*Cb))); % Series circuit model
loglog(Frequency,Final_absZ(:,1),'g','LineWidth', 2.0) % Experimental
result
hold on
loglog(x,y,'r','LineWidth',2.0)
hold off
```

6.3 Appendix C: Mobile Application

C.1 Measurement Parameters

Parameter	Value
R_{FB}	250 Ω
Gain Factor	$3.284732484 * 10^{-6}$
Threshold	0%

Table 6-1: Measurement parameters for wireless sensing using the PCB.

C.2 Representative Export File

ID	DeviceNa	DeviceAd	RealImpe	Imaginary	Impedeni	PctChang	Phase	Commanc	TimeStan	RealRaw	Imaginary	RealAdjus	Imaginary
1780	Bf DEV	00000000-	-161	-489	647.4726		1.252731	Initial Me	2/19/2020	5FFF	17FE	FF5F	FE17
1781	Bf DEV	00000000-						Device Di	2/19/2020	0x0000	0x0000	0x0000	0x0000
1782	Bf DEV	00000000-						Device Cc	2/19/2020	0x0000	0x0000	0x0000	0x0000
1783	Bf DEV	00000000-	-749	-482	374.2426	-42.1995	0.57181	Biofilm Fc	2/19/2020	13FD	1EFE	FD13	FE1E
1784	Bf DEV	00000000-	-749	-485	373.5602	-42.3049	0.574637	Biofilm Fc	2/19/2020	13FD	1BFE	FD13	FE1B
1785	Bf DEV	00000000-						Device Di	2/19/2020	0x0000	0x0000	0x0000	0x0000
1786	Bf DEV	00000000-						Device Cc	2/19/2020	0x0000	0x0000	0x0000	0x0000
1787	Bf DEV	00000000-	-40	-220	1490.712	130.2355	1.390943	Take Mea	2/19/2020	D8FF	24FF	FFD8	FF24
1788	Bf DEV	00000000-	-160	-490	646.6704	-0.1239	1.255181	Biofilm Fc	2/19/2020	60FF	16FE	FF60	FE16
1789	Bf DEV	00000000-	-118	-578	565.0464	-12.7305	1.369411	Biofilm Fc	2/19/2020	8AFF	BEFD	FF8A	FDBE
1790	Bf DEV	00000000-	-140	-660	494.0576	-23.6944	1.361773	Biofilm Fc	2/19/2020	74FF	6CFD	FF74	FD6C
1791	Bf DEV	00000000-	-137	-666	490.2358	-24.2847	1.367921	Biofilm Fc	2/19/2020	77FF	66FD	FF77	FD66
1792	Bf DEV	00000000-	-143	-675	483.105	-25.386	1.362031	Biofilm Fc	2/19/2020	71FF	5DFD	FF71	FD5D
1793	Bf DEV	00000000-	-140	-678	481.4845	-25.6363	1.367169	Biofilm Fc	2/19/2020	74FF	5AFD	FF74	FD5A
1794	Bf DEV	00000000-	-170	-733	442.9942	-31.581	1.342902	Biofilm Fc	2/20/2020	56FF	23FD	FF56	FD23
1795	Bf DEV	00000000-	-168	-732	443.8341	-31.4513	1.345195	Biofilm Fc	2/20/2020	58FF	24FD	FF58	FD24
1796	Bf DEV	00000000-	-173	-736	440.8828	-31.9071	1.339933	Biofilm Fc	2/20/2020	53FF	20FD	FF53	FD20
1797	Bf DEV	00000000-	-175	-738	439.4842	-32.1231	1.337969	Biofilm Fc	2/20/2020	51FF	1EFD	FF51	FD1E
1798	Bf DEV	00000000-	-173	-739	439.1862	-32.1692	1.340837	Biofilm Fc	2/20/2020	53FF	1DFD	FF53	FD1D
1799	Bf DEV	00000000-	-179	-745	435.0461	-32.8086	1.334998	Biofilm Fc	2/20/2020	4DFF	17FD	FF4D	FD17
1800	Bf DEV	00000000-						Treatmen	2/20/2020	0x0000	0x0000	0x0000	0x0000
1801	Bf DEV	00000000-						Device Di	2/20/2020	0x0000	0x0000	0x0000	0x0000
1802	Bf DEV	00000000-						Device Cc	2/21/2020	0x0000	0x0000	0x0000	0x0000
1803	Bf DEV	00000000-						Device Sh	2/21/2020	0x0000	0x0000	0x0000	0x0000
1804	Bf DEV	00000000-	-64	-642	516.65	-20.2051	1.471436	Biofilm Fc	2/21/2020	C0FF	7EFD	FFC0	FD7E
1805	Bf DEV	00000000-						Device Di	2/21/2020	0x0000	0x0000	0x0000	0x0000

Table 6-2: Representative export file from mobile application including device name, time stamp, command, impedance values, phase angle, and calculated percent change.

7. Bibliography

[1] C. for D. C. and P. N. C. for E. Z. I. Diseases, “2018 National and State Healthcare-Associated Infections Progress Report,” 2019.

[2] S. S. Magill *et al.*, “Multistate Point-Prevalence Survey of Health Care–Associated Infections,” *N. Engl. J. Med.*, vol. 370, no. 13, pp. 1198–1208, 2014.

[3] T. G. Emori and R. P. Gaynes, “An overview of nosocomial infections, including the role of the microbiology laboratory,” *Clinical Microbiology Reviews*, vol. 6, no. 4. pp. 428–442, 1993.

[4] A. L. Flores-Mireles, J. N. Walker, M. Caparon, and S. J. Hultgren, “Urinary tract infections: Epidemiology, mechanisms of infection and treatment options,” *Nature Reviews Microbiology*, vol. 13, no. 5. pp. 269–284, 2015.

[5] T. M. Hooton *et al.*, “Diagnosis, Prevention, and Treatment of Catheter-Associated Urinary Tract Infection in Adults: 2009 International Clinical Practice Guidelines from the Infectious Diseases Society of America,” *Clin. Infect. Dis.*, vol. 50, no. 5, pp. 625–663, 2010.

[6] Q. Jordano, M. Molina, E. Acosta, M. Xercavins, and A. de la Sierra, “Diagnosing catheter-associated urinary tract infection: Still a matter of concern,” *European Journal of Internal Medicine*, vol. 52. pp. e30–e31, 2018.

[7] P. A. Tambyah and D. G. Maki, “Catheter-Associated Urinary Tract Infection Is Rarely Symptomatic,” *Arch. Intern. Med.*, vol. 160, no. 5, 2000.

[8] “Estimating the Additional Hospital Inpatient Cost and Mortality Associated With Selected Hospital-Acquired Conditions,” 2017. [Online]. Available:

http://www.ahrq.gov/hai/pfp/haccost2017.html.

[9] C. V Gould, C. A. Umscheid, R. K. Agarwal, G. Kuntz, and D. A. Pegues, “Guideline for Prevention of Catheter-Associated Urinary Tract Infections 2009 Guideline for Prevention of Catheter-Associated Urinary Tract Infections 2009,” *Infect. Control Pract. Advis. Comm. Source Infect. Control Hosp. Epidemiol.*, vol. 31, no. 4, pp. 319–326, 2010.

[10] S. M. Jacobsen, D. J. Stickler, H. L. T. Mobley, and M. E. Shirtliff, “Complicated Catheter-Associated Urinary Tract Infections Due to Escherichia coli and Proteus mirabilis,” *Clin. Microbiol. Rev.*, vol. 21, no. 1, pp. 26–59, 2008.

[11] J. W. Costerton, P. S. Stewart, and E. P. Greenberg, “Bacterial biofilms: a common cause of persistent infections.,” *Science*, vol. 284, no. 5418, pp. 1318–22, 1999.

[12] H. Anwar, M. K. Dasgupta, and J. W. Costerton, “Testing the susceptibility of bacteria in biofilms to antibacterial agents,” *Antimicrob. Agents Chemother.*, vol. 34, no. 11, pp. 2043–2046, 1990.

[13] S. Subramanian, R. C. Huiszoon, S. Chu, W. E. Bentley, and R. Ghodssi, “Microsystems for biofilm characterization and sensing – A review,” vol. 2, no. September 2019, 2020.

[14] M. Pousti, M. P. Zarabadi, M. Abbaszadeh Amirdehi, F. Paquet-Mercier, and J. Greener, “Microfluidic bioanalytical flow cells for biofilm studies: a review,” *Analyst*, vol. 144, no. 1. pp. 68–86, 2019.

[15] J. Paredes, S. Becerro, F. Arizti, A. Aguinaga, J. L. Del Pozo, and S. Arana, “Real time monitoring of the impedance characteristics of Staphylococcal bacterial biofilm cultures with a modified CDC reactor system,” *Biosens. Bioelectron.*, vol. 38, no. 1, pp. 226–232,

2012.

[16] S. Subramanian, E. I. Tolstaya, T. E. Winkler, W. E. Bentley, and R. Ghodssi, “An Integrated Microsystem for Real-Time Detection and Threshold-Activated Treatment of Bacterial Biofilms,” *ACS Appl. Mater. Interfaces*, p. acsami.7b04828, 2017.

[17] J. W. Costerton, B. Ellis, K. Lam, F. Johnson, and A. E. Khoury, “Mechanism of electrical enhancement of efficacy of antibiotics in killing biofilm bacteria,” *Antimicrob. Agents Chemother.*, vol. 38, no. 12, pp. 2803–2809, 1994.

[18] R. C. Huiszoon, J. M. Stine, L. A. Beardslee, P. Ramiah Rajasekaran, W. E. Bentley, and R. Ghodssi, “Flexible Impedance Sensor for Wireless Monitoring of Catheter Biofilms,” in *Hilton Head Workshop 2018: A Solid-State Sensors, Actuators and Microsystems Workshop*, 2018.

[19] M. Elder, “Global Markets for Catheters,” 2016.

[20] H.-C. Flemming, J. Wingender, U. Szewzyk, P. Steinberg, S. A. Rice, and S. Kjelleberg, “Biofilms: an emergent form of bacterial life,” *Nat. Rev. Microbiol.*, vol. 14, no. 9, pp. 563–575, 2016.

[21] M. Hausner and S. Wuertz, “High rates of conjugation in bacterial biofilms as determined by quantitative in situ analysis,” *Appl. Environ. Microbiol.*, vol. 65, no. 8, pp. 3710–3713, 1999.

[22] R. AP., P. J., W. M., and M. P., “Transfer of a conjugative transposon, Tn5397 in a model oral biofilm.,” *FEMS Microbiol. Lett.*, vol. 177, no. 1 PG-63-6, pp. 63–66, 1999.

[23] M. Habash and G. Reid, “Microbial biofilms: their development and significance for

medical device-related infections.," *J. Clin. Pharmacol.*, vol. 39, no. 9, pp. 887–898, 1999.

[24] R. M. Klevens *et al.*, "Estimating Health Care-Associated Infections and Deaths in U.S. Hospitals, 2002," *Public Health Rep.*, vol. 122, no. 2, pp. 160–166, 2007.

[25] J. C. Nickel and J. W. Costerton, "Bacterial Biofilms and Catheters: A Key to Understanding Bacterial Strategies in Catheter-Associated Urinary Tract Infection," *Can. J. Infect. Dis.*, vol. 3, no. 5, pp. 261–267, 1992.

[26] T. R. Garrett, M. Bhakoo, and Z. Zhang, "Bacterial adhesion and biofilms on surfaces," *Progress in Natural Science*, vol. 18, no. 9. pp. 1049–1056, 2008.

[27] M. B. Miller and B. L. Bassler, "Quorum Sensing in Bacteria," *Annu. Rev. Microbiol.*, vol. 55, no. 1, pp. 165–199, 2001.

[28] K. Lewis, "Persister cells, dormancy and infectious disease," *Nature Reviews Microbiology*, vol. 5, no. 1. pp. 48–56, 2007.

[29] A. L. Spoering and K. Lewis, "Biofilms and planktonic cells of Pseudomonas aeruginosa have similar resistance to killing by antimicrobials," *J. Bacteriol.*, vol. 183, no. 23, pp. 6746–6751, 2001.

[30] R. O. Darouiche, "Treatment of Infections Associated with Surgical Implants," *N. Engl. J. Med.*, vol. 35014350, pp. 1422–9, 2004.

[31] P. V. Gawande, A. P. Clinton, K. LoVetri, N. Yakandawala, K. P. Rumbaugh, and S. Madhyastha, " Antibiofilm Efficacy of DispersinB ® Wound Spray Used in Combination with a Silver Wound Dressing ," *Microbiol. Insights*, vol. 7, p. MBI.S13914, 2014.

[32] A. Vendeville, K. Winzer, K. Heurlier, C. M. Tang, and K. R. Hardie, “Making ‘sense’ of metabolism: autoinducer-2, LUXS and pathogenic bacteria,” *Nat. Rev. Microbiol.*, vol. 3, no. 5, pp. 383–396, 2005.

[33] V. Roy, J. A. I. Smith, J. X. Wang, J. E. Stewart, W. E. Bentley, and H. O. Sintim, “Synthetic Analogs Tailor Native Al-2 Signaling Across Bacterial Species,” *J Am Chem Soc*, vol. 132, no. 32, pp. 11141–11150, 2010.

[34] V. Roy *et al.*, “AI-2 analogs and antibiotics: A synergistic approach to reduce bacterial biofilms,” *Appl. Microbiol. Biotechnol.*, vol. 97, no. 6, pp. 2627–2638, 2013.

[35] E. Teirlinck *et al.*, “Laser-induced vapor nanobubbles improve diffusion in biofilms of antimicrobial agents for wound care,” *Biofilm*, vol. 1, p. 100004, 2019.

[36] Y. J. Ruby Chang, J. Perry, and K. Cross, “Low-frequency ultrasound debridement in chronic wound healing: A systematic review of current evidence,” *Plast. Surg.*, vol. 25, no. 1, pp. 21–26, 2017.

[37] D. Monroe, “Looking for chinks in the armor of bacterial biofilms,” *PLoS Biol.*, vol. 5, no. 11, pp. 2458–2461, 2007.

[38] A. E. Khoury, K. Lam, B. Ellis, and J. W. Costerton, “Prevention and control of bacterial infections associated with medical devices,” *ASAIO J.*, vol. 38, no. 3, 1992.

[39] J. L. Del Pozo, M. S. Rouse, and R. Patel, “Bioelectric effect and bacterial biofilms. A systematic review.,” *Int. J. Artif. Organs*, vol. 31, no. 9, pp. 786–95, 2008.

[40] S. A. Blenkinsopp, A. E. Khoury, and J. W. Costerton, “Electrical enhancement of biocide efficacy against Pseudomonas aeruginosa biofilms,” *Appl. Environ. Microbiol.*, vol. 58,

no. 11, pp. 3770–3773, 1992.

[41] S. Subramanian, K. Gerasopoulos, M. Guo, H. O. Sintim, W. E. Bentley, and R. Ghodssi, "Autoinducer-2 analogs and electric fields - an antibiotic-free bacterial biofilm combination treatment," *Biomed. Microdevices*, vol. 18, no. 5, pp. 1–12, 2016.

[42] D. H. Dusane *et al.*, "Electroceutical Treatment of Pseudomonas aeruginosa Biofilms," *Sci. Rep.*, vol. 9, no. 1, 2019.

[43] S. T. Sultana *et al.*, "Electrochemical scaffold generates localized, low concentration of hydrogen peroxide that inhibits bacterial pathogens and biofilms.," *Sci. Rep.*, vol. 5, no. October, p. 14908, 2015.

[44] R. M. Donlan, "Biofilms: Microbial life on surfaces," *Emerging Infectious Diseases*, vol. 8, no. 9. pp. 881–890, 2002.

[45] J. Azeredo *et al.*, "Critical review on biofilm methods," *Critical Reviews in Microbiology*, vol. 43, no. 3. pp. 313–351, 2017.

[46] A. Kharazmi, B. Giwercman, and N. Høiby, "Robbins device in biofilms research," *Methods Enzymol.*, vol. 310, pp. 207–215, 1999.

[47] D. L. Williams, K. L. Woodbury, B. S. Haymond, A. E. Parker, and R. D. Bloebaum, "A modified CDC biofilm reactor to produce mature biofilms on the surface of PEEK membranes for an in vivo animal model application," *Curr. Microbiol.*, vol. 62, no. 6, pp. 1657–1663, 2011.

[48] S. A. Crusz *et al.*, "Bursting the bubble on bacterial biofilms: A flow cell methodology," *Biofouling*, vol. 28, no. 8, pp. 835–842, 2012.

[49] B. F. Gilmore, T. M. Hamill, D. S. Jones, and S. P. Gorman, “Validation of the CDC biofilm reactor as a dynamic model for assessment of encrustation formation on urological device materials,” *J. Biomed. Mater. Res. - Part B Appl. Biomater.*, vol. 93, no. 1, pp. 128–140, 2010.

[50] H. Ceri, M. E. Olson, C. Stremick, R. R. Read, D. Morck, and a Buret, “The Calgary Biofilm Device : New Technology for Rapid Determination of Antibiotic Susceptibilities of Bacterial Biofilms The Calgary Biofilm Device : New Technology for Rapid Determination of Antibiotic Susceptibilities of Bacterial Biofilms,” *J. Clin. Microbiol.*, vol. 37, no. 6, p. 1771, 1999.

[51] M. E. Olson, H. Ceri, D. W. Morck, A. G. Buret, and R. R. Read, “Biofilm bacteria: Formation and comparative susceptibility to antibiotics,” *Can. J. Vet. Res.*, vol. 66, no. 2, pp. 86–92, 2002.

[52] C. Hannig, M. Follo, E. Hellwig, and A. Al-Ahmad, “Visualization of adherent micro-organisms using different techniques,” *Journal of Medical Microbiology*, vol. 59, no. 1. pp. 1–7, 2010.

[53] R. J. Palmer and C. Sternberg, “Modern microscopy in biofilm research: Confocal microscopy and other approaches,” *Curr. Opin. Biotechnol.*, vol. 10, no. 3, pp. 263–268, 1999.

[54] M. T. Meyer, V. Roy, W. E. Bentley, and R. Ghodssi, “Development and validation of a microfluidic reactor for biofilm monitoring via optical methods,” *J. Micromechanics Microengineering*, vol. 21, no. 5, p. 54023, 2011.

[55] J. Kim, M. Hegde, S. H. Kim, T. K. Wood, and A. Jayaraman, “A microfluidic device for

high throughput bacterial biofilm studies," *Lab Chip*, vol. 12, no. 6, p. 1157, 2012.

[56] V. Janakiraman, D. Englert, A. Jayaraman, and H. Baskaran, "Modeling growth and quorum sensing in biofilms grown in microfluidic chambers," *Ann. Biomed. Eng.*, vol. 37, no. 6, pp. 1206–1216, 2009.

[57] K. P. Kim *et al.*, "In situ monitoring of antibiotic susceptibility of bacterial biofilms in a microfluidic device," *Lab Chip*, vol. 10, no. 23, pp. 3296–3299, 2010.

[58] J. Paredes, S. Becerro, and S. Arana, "Label-free interdigitated microelectrode based biosensors for bacterial biofilm growth monitoring using Petri dishes," *J. Microbiol. Methods*, vol. 100, no. 1, pp. 77–83, 2014.

[59] S. M. Radke and E. C. Alocilja, "Design and fabrication of a microimpedance biosensor for bacterial detection," *IEEE Sens. J.*, vol. 4, no. 4, pp. 434–440, 2004.

[60] R. A. Brady, J. G. Leid, A. K. Camper, J. W. Costerton, and M. E. Shirtliff, "Identification of Staphylococcus aureus proteins recognized by the antibody-mediated immune response to a biofilm infection," *Infect. Immun.*, vol. 74, no. 6, pp. 3415–3426, 2006.

[61] K. L. Swope and M. C. Flickinger, "The use of confocal scanning laser microscopy and other tools to characterize Escherichia coli in a high-cell-density synthetic biofilm," in *Biotechnology and Bioengineering*, 1996, vol. 52, no. 2, pp. 340–356.

[62] K. N. Kragh, M. Alhede, L. Kvich, and T. Bjarnsholt, "Into the well—A close look at the complex structures of a microtiter biofilm and the crystal violet assay," *Biofilm*, vol. 1, p. 100006, 2019.

[63] L. Ganderton, J. Chawla, C. Winters, J. Wimpenny, and D. Stickler, "Scanning electron

microscopy of bacterial biofilms on indwelling bladder catheters," *Eur. J. Clin. Microbiol. Infect. Dis.*, vol. 11, no. 9, pp. 789–796, 1992.

[64] Y. Yawata *et al.*, "Monitoring biofilm development in a microfluidic device using modified confocal reflection microscopy," *J. Biosci. Bioeng.*, vol. 110, no. 3, pp. 377–380, 2010.

[65] H. Y. N. Holman, R. Miles, Z. Hao, E. Wozei, L. M. Anderson, and H. Yang, "Real-time chemical imaging of bacterial activity in biofilms using open-channel microfluidics and synchrotron FTIR spectromicroscopy," *Anal. Chem.*, vol. 81, no. 20, pp. 8564–8570, 2009.

[66] S. Mattana *et al.*, "High-contrast Brillouin and Raman micro-spectroscopy for simultaneous mechanical and chemical investigation of microbial biofilms," *Biophys. Chem.*, vol. 229, pp. 123–129, 2017.

[67] P. N. Abadian, N. Tandogan, J. J. Jamieson, and E. D. Goluch, "Using surface plasmon resonance imaging to study bacterial biofilms," *Biomicrofluidics*, vol. 8, no. 2, 2014.

[68] Y. Yuan *et al.*, "Electrochemical Surface Plasmon Resonance Fiber-Optic Sensor: In Situ Detection of Electroactive Biofilms," *Anal. Chem.*, vol. 88, no. 15, pp. 7609–7616, 2016.

[69] W. Hu, X. Qiu, X. Zhang, Z. Zhang, J. Tang, and Y. Yuan, "In-situ detection of electroactive biofilms using an electrochemical surface Plasmon resonance fiber-optic sensor," pp. 1–3.

[70] R. Kiran and S. A. Patil, "Microbial Electroactive Biofilms," in *ACS Symposium Series*, vol. 1323, 2019, pp. 159–186.

[71] N. Zhong, M. Zhao, and Y. Li, “U-shaped, double-tapered, fiber-optic sensor for effective biofilm growth monitoring,” *Biomed. Opt. Express*, vol. 7, no. 2, p. 335, 2016.

[72] R. Philip-Chandy *et al.*, “Optical fiber sensor for biofilm measurement using intensity modulation and image analysis,” *IEEE J. Sel. Top. Quantum Electron.*, vol. 6, no. 5, pp. 764–772, 2000.

[73] Y. W. Kim, M. P. Mosteller, S. Subramanian, M. T. Meyer, W. E. Bentley, and R. Ghodssi, “An optical microfluidic platform for spatiotemporal biofilm treatment monitoring,” *J. Micromechanics Microengineering*, vol. 26, no. 1, 2015.

[74] K. Keiji Kanazawa and J. G. Gordon, “The oscillation frequency of a quartz resonator in contact with liquid,” *Anal. Chim. Acta*, vol. 175, no. C, pp. 99–105, 1985.

[75] V. Reipa, J. Almeida, and K. D. Cole, “Long-term monitoring of biofilm growth and disinfection using a quartz crystal microbalance and reflectance measurements,” *J. Microbiol. Methods*, vol. 66, no. 3, pp. 449–459, 2006.

[76] P. Castro, L. Elvira, J. R. Maestre, and F. M. de Espinosa, “Study of the relation between the resonance behavior of thickness shear mode (TSM) sensors and the mechanical characteristics of biofilms,” *Sensors (Switzerland)*, vol. 17, no. 6, 2017.

[77] A. L. Schofield, T. R. Rudd, D. S. Martin, D. G. Fernig, and C. Edwards, “Real-time monitoring of the development and stability of biofilms of Streptococcus mutans using the quartz crystal microbalance with dissipation monitoring,” *Biosens. Bioelectron.*, vol. 23, no. 3, pp. 407–413, 2007.

[78] I. M. Marcus, M. Herzberg, S. L. Walker, and V. Freger, “Pseudomonas aeruginosa

attachment on QCM-D sensors: The role of cell and surface hydrophobicities," *Langmuir*, vol. 28, no. 15, pp. 6396–6402, 2012.

[79] A. L. J. Olsson, H. C. Van Der Mei, H. J. Busscher, and P. K. Sharma, "Influence of cell surface appendages on the bacterium-substratum interface measured real-time using QCM-D," *Langmuir*, vol. 25, no. 3, pp. 1627–1632, 2009.

[80] A. L. J. Olsson, H. C. van der Mei, H. J. Busscher, and P. K. Sharma, "Acoustic sensing of the bacterium-substratum interface using QCM-D and the influence of extracellular polymeric substances," *J. Colloid Interface Sci.*, vol. 357, no. 1, pp. 135–138, 2011.

[81] K. Waszczuk *et al.*, "Evaluation of Pseudomonas aeruginosa biofilm formation using piezoelectric tuning fork mass sensors," *Sensors Actuators, B Chem.*, vol. 170, pp. 7–12, 2012.

[82] T. Piasecki *et al.*, "Autonomous system for in Situ Assay of Antibiotic Activity on Bacterial Biofilms Using Viscosity and Density Sensing Quartz Tuning Forks," *Procedia Eng.*, vol. 168, pp. 745–748, 2016.

[83] J. D.S. Ballantine *et al.*, "Chapter 1 Why Acoustic Sensors?," *Acoust. Wave Sensors Theory, Des. Physico-Chemical Appl.*, 1997.

[84] E. Gizeli, "Acoustic transducers," in *Biomolecular Sensors*, 2002.

[85] J. Freudenberg, M. Von Schickfus, and S. Hunklinger, "A SAW immunosensor for operation in liquid using a SiO2 protective layer," in *Sensors and Actuators, B: Chemical*, 2001, vol. 76, no. 1–3, pp. 147–151.

[86] E. Berkenpas, P. Millard, and M. Pereira da Cunha, "Detection of Escherichia coli

O157:H7 with langasite pure shear horizontal surface acoustic wave sensors," *Biosens. Bioelectron.*, vol. 21, no. 12, pp. 2255–2262, 2006.

[87] Y. W. Kim *et al.*, "A Surface Acoustic Wave Biofilm Sensor Integrated With A Treatment Method Based On The Bioelectric Effect," *Sensors Actuators A Phys.*, 2015.

[88] Y. W. Kim *et al.*, "An ALD aluminum oxide passivated Surface Acoustic Wave sensor for early biofilm detection," *Sensors Actuators, B Chem.*, vol. 163, no. 1, pp. 136–145, 2012.

[89] E. H. Yoo and S. Y. Lee, "Glucose biosensors: An overview of use in clinical practice," *Sensors*, vol. 10, no. 5. pp. 4558–4576, 2010.

[90] L. C. Clark and C. Lyons, "ELECTRODE SYSTEMS FOR CONTINUOUS MONITORING IN CARDIOVASCULAR SURGERY," *Ann. N. Y. Acad. Sci.*, vol. 102, no. 1, pp. 29–45, 1962.

[91] P. Silley and S. Forsythie, "Impedance microbiology-a rapid change for microbiologists," *J. Appl. Bacteriol.*, vol. 80, no. 3, pp. 233–243, 1996.

[92] L. Yang and R. Bashir, "Electrical / electrochemical impedance for rapid detection of foodborne pathogenic bacteria," *Biotechnol. Adv.*, vol. 26, pp. 135–150, 2008.

[93] M. Varshney and Y. Li, "Interdigitated array microelectrodes based impedance biosensors for detection of bacterial cells," *Biosensors and Bioelectronics*, vol. 24, no. 10. pp. 2951–2960, 2009.

[94] R. Gómez, R. Bashir, and A. K. Bhunia, "Microscale electronic detection of bacterial metabolism," *Sensors Actuators, B Chem.*, vol. 86, no. 2–3, pp. 198–208, 2002.

[95] L. Yang, Y. Li, C. L. Griffis, and M. G. Johnson, "Interdigitated microelectrode (IME)

impedance sensor for the detection of viable Salmonella typhimurium," *Biosens. Bioelectron.*, vol. 19, no. 10, pp. 1139–1147, 2004.

[96] P. Van Gerwen *et al.*, "Nanoscaled interdigitated electrode arrays for biochemical sensors," *Sensors Actuators, B Chem.*, vol. 49, no. 1–2, pp. 73–80, 1998.

[97] J. Paredes, S. Becerro, and S. Arana, "Label-free interdigitated microelectrode based biosensors for bacterial biofilm growth monitoring using Petri dishes," *J. Microbiol. Methods*, vol. 100, no. 1, pp. 77–83, 2014.

[98] L. Liu *et al.*, "Monitoring of bacteria biofilms forming process by in-situ impedimetric biosensor chip," *Biosens. Bioelectron.*, vol. 112, pp. 86–92, 2018.

[99] I. Tubia, J. Paredes, E. Pérez-Lorenzo, and S. Arana, "Brettanomyces bruxellensis growth detection using interdigitated microelectrode based sensors by means of impedance analysis," *Sensors Actuators, A Phys.*, vol. 269, pp. 175–181, 2018.

[100] K. Chabowski *et al.*, "Impedance sensors made in PCB and LTCC technologies for monitoring growth and degradation of pseudomonal biofilm," *Metrol. Meas. Syst.*, vol. 24, no. 2, pp. 369–380, 2017.

[101] D. Gutiérrez, C. Hidalgo-Cantabrana, A. Rodríguez, P. García, and P. Ruas-Madiedo, "Monitoring in real time the formation and removal of biofilms from clinical related pathogens using an impedance-based technology," *PLoS One*, vol. 11, no. 10, 2016.

[102] M. Stöckl, C. Schlegel, A. Sydow, D. Holtmann, R. Ulber, and K. M. Mangold, "Membrane Separated Flow Cell for Parallelized Electrochemical Impedance Spectroscopy and Confocal Laser Scanning Microscopy to Characterize Electro-Active

Microorganisms," *Electrochim. Acta*, vol. 220, pp. 444–452, 2016.

[103] J. Bruchmann, K. Sachsenheimer, B. E. Rapp, and T. Schwartz, "Multi-channel microfluidic biosensor platform applied for online monitoring and screening of biofilm formation and activity," *PLoS One*, vol. 10, no. 2, pp. 1–19, 2015.

[104] O. Estrada-Leypon *et al.*, "Simultaneous monitoring of Staphylococcus aureus growth in a multi-parametric microfluidic platform using microscopy and impedance spectroscopy," *Bioelectrochemistry*, vol. 105, pp. 56–64, 2015.

[105] M. Carminati *et al.*, "A Smart Sensing Node for Pervasive Water Quality Monitoring with Anti-Fouling Self-Diagnostics," in *Proceedings - IEEE International Symposium on Circuits and Systems*, 2018, vol. 2018–May.

[106] I. Tubía, J. Paredes, E. Pérez-Lorenzo, and S. Arana, "Antibody biosensors for spoilage yeast detection based on impedance spectroscopy," *Biosens. Bioelectron.*, vol. 102, pp. 432–438, 2018.

[107] S. Bayoudh, A. Othmane, L. Ponsonnet, and H. Ben Ouada, "Electrical detection and characterization of bacterial adhesion using electrochemical impedance spectroscopy-based flow chamber," *Colloids Surfaces A Physicochem. Eng. Asp.*, vol. 318, no. 1–3, pp. 291–300, 2008.

[108] J. Palmer, S. Flint, and J. Brooks, "Bacterial cell attachment, the beginning of a biofilm," *J. Ind. Microbiol. Biotechnol.*, vol. 34, no. 9, pp. 577–588, 2007.

[109] S. Becerro, J. Paredes, M. Mujika, E. Pérez Lorenzo, and S. Arana, "Electrochemical Real-Time Analysis of Bacterial Biofilm Adhesion and Development by Means of Thin-

Film Biosensors," *IEEE Sens. J.*, vol. 16, no. 7, pp. 1856–1864, 2016.

[110] J. Min and A. J. Baeumner, "Characterization and optimization of interdigitated ultramicroelectrode arrays as electrochemical biosensor transducers," *Electroanalysis*, vol. 16, no. 9, pp. 724–729, 2004.

[111] M. Rahimi and S. R. Mikkelsen, "Cyclic biamperometry at micro-interdigitated electrodes.," *Anal. Chem.*, vol. 83, no. 19, pp. 7555–7559, 2011.

[112] O. Fysun, S. Khorshid, J. Rauschnabel, and H. C. Langowski, "Electrochemical detection of a P. polymyxa biofilm and CIP cleaning solutions by voltammetric microsensors," *Eng. Agric. Environ. Food*, vol. 12, no. 2, pp. 232–243, 2019.

[113] D. L. Bellin, H. Sakhtah, Y. Zhang, A. Price-Whelan, L. E. P. Dietrich, and K. L. Shepard, "Electrochemical camera chip for simultaneous imaging of multiple metabolites in biofilms.," *Nat. Commun.*, vol. 7, p. 10535; 10.1038/ncomms10535, 2016.

[114] R. D. Scott, "The direct medical costs of healthcare-associated infections in U.S. hospitals and the benefits of prevention," *Cdc*, no. March, p. 13, 2009.

[115] N. Sabir *et al.*, "Bacterial biofilm-based catheter-associated urinary tract infections: Causative pathogens and antibiotic resistance," *Am. J. Infect. Control*, vol. 45, no. 10, pp. 1101–1105, 2017.

[116] P. A. Tambyah, K. T. Halvorson, and D. G. Maki, "A prospective study of pathogenesis of catheter-associated urinary tract infections," *Mayo Clin. Proc.*, vol. 74, no. 2, pp. 131–136, 1999.

[117] K. A. Getliffe, "The characteristics and management of patients with recurrent blockage

of long-term urinary catheters," *J. Adv. Nurs.*, vol. 20, no. 1, pp. 140–149, 1994.

[118] P. W. Smith and J. M. Mylotte, "Nursing Home-Acquired Bloodstream Infection," *Infect. Control Hosp. Epidemiol.*, vol. 26, no. 10, pp. 833–837, 2005.

[119] C. S. Hollenbeak and A. L. Schilling, "The attributable cost of catheter-associated urinary tract infections in the United States: A systematic review," *Am. J. Infect. Control*, vol. 46, no. 7, pp. 751–757, 2018.

[120] D. G. Maki, C. E. Weise, and H. W. Sarafin, "A Semiquantitative Culture Method for Identifying Intravenous-Catheter-Related Infection," *N. Engl. J. Med.*, vol. 296, no. 23, pp. 1305–1309, 1977.

[121] B. W. Trautner, R. A. Hull, and R. O. Darouiche, "Prevention of catheter-associated urinary tract infection," *Current Opinion in Infectious Diseases*, vol. 18, no. 1. pp. 37–41, 2005.

[122] K. D. Mandakhalikar, R. R. Chua, and P. A. Tambyah, "New Technologies for Prevention of Catheter Associated Urinary Tract Infection," *Curr. Treat. Options Infect. Dis.*, vol. 8, no. 1, pp. 24–41, 2016.

[123] K. K. Chung, J. F. Schumacher, E. M. Sampson, R. A. Burne, P. J. Antonelli, and A. B. Brennan, "Impact of engineered surface microtopography on biofilm formation of *Staphylococcus aureus*," *Biointerphases*, vol. 2, no. 2, pp. 89–94, 2007.

[124] N. Maccallum *et al.*, "Liquid-Infused Silicone As a Biofouling-Free Medical Material," *ACS Biomater. Sci. Eng.*, vol. 1, no. 1, pp. 43–51, 2015.

[125] Samaun, K. D. Wise, and J. B. Angell, "An IC Piezoresistive Pressure Sensor for

Biomedical Instrumentation," *IEEE Trans. Biomed. Eng.*, vol. BME-20, no. 2, pp. 101–109, 1973.

[126] J. F. L. Goosen, P. J. French, and P. M. Sarro, "Pressure, flow and oxygen saturation sensors on one chip for use in catheters," *Proc. IEEE Micro Electro Mech. Syst.*, pp. 537–540, 2000.

[127] X. Du *et al.*, "Fabrication of a Flexible Amperometric Glucose Sensor Using Additive Processes," *ECS J. Solid State Sci. Technol.*, vol. 4, no. 4, pp. P3069–P3074, 2015.

[128] Q. Yang, A. Lee, R. T. Bentley, and H. Lee, "Piezoresistor-embedded multifunctional magnetic microactuators for implantable self-clearing catheter," *IEEE Sens. J.*, vol. 19, no. 4, pp. 1373–1378, 2019.

[129] I. Kalb, R. Shaw, and M. Ram, "Female incontinence device including electronic sensors," 5476434, 1995.

[130] W. Noda, "TEMPERATURE SENSOR ADAPTER FOR FOLEY CATHETERS," US 2003/0114835 A1, 2003.

[131] W. Noda, "FOLEY CATHETER HAVING REDUNDANT TEMPERATURE SENSORS AND METHOD," USOO6602243B2 (10), 2003.

[132] M. Denton, T. Wolfe, P. Croll, and M. Christensen, "Continuous Intra-Abdominal Pressure Monitoring Urinary Catheter with Optional Core Temperature Sensor," US 2008/0103408 A1, 2008.

[133] W. M. Fallis, "Monitoring urinary bladder temperature in the intensive care unit: State of the science," *Am. J. Crit. Care*, vol. 11, no. 1, pp. 38–47, 2002.

[134] S. Milo, N. T. Thet, D. Liu, J. Nzakizwanayo, B. V. Jones, and A. T. A. Jenkins, “An in-situ infection detection sensor coating for urinary catheters,” *Biosens. Bioelectron.*, vol. 81, pp. 166–172, 2016.

[135] S. Malic, M. G. J. Waters, L. Basil, D. J. Stickler, and D. W. Williams, “Development of an ‘early warning’ sensor for encrustation of urinary catheters following Proteus infection,” *J. Biomed. Mater. Res. - Part B Appl. Biomater.*, vol. 100 B, no. 1, pp. 133–137, 2012.

[136] D. J. Stickler, S. M. Jones, G. O. Adusei, and M. G. Waters, “A sensor to detect the early stages in the development of crystalline Proteus mirabilis biofilm on indwelling bladder catheters,” *J. Clin. Microbiol.*, vol. 44, no. 4, pp. 1540–1542, 2006.

[137] R. R. Spurbeck and H. L. T. Mobley, “Uropathogenic Escherichia coli,” in *Escherichia coli: Pathotypes and Principles of Pathogenesis: Second Edition*, 2013, pp. 275–304.

[138] P. M. Harrey, B. J. Ramsey, P. S. A. Evans, and D. J. Harrison, “Capacitive-type humidity sensors fabricated using the offset lithographic printing process,” *Sensors Actuators, B Chem.*, vol. 87, no. 2, pp. 226–232, 2002.

[139] J. Engel, J. Chen, and C. Liu, “Development of polyimide flexible tactile sensor skin,” *J. Micromechanics Microengineering*, vol. 13, no. 3, pp. 359–366, 2003.

[140] T. Sekitani, U. Zschieschang, H. Klauk, and T. Someya, “Flexible organic transistors and circuits with extreme bending stability.,” *Nat. Mater.*, vol. 9, no. 12, pp. 1015–1022, 2010.

[141] A. Mercanzini *et al.*, “Demonstration of cortical recording using novel flexible polymer neural probes,” *Sensors Actuators, A Phys.*, vol. 143, no. 1, pp. 90–96, 2008.

[142] J. M. Seo, S. J. Kim, H. Chung, E. T. Kim, H. G. Yu, and Y. S. Yu, “Biocompatibility of polyimide microelectrode array for retinal stimulation,” *Mater. Sci. Eng. C*, vol. 24, no. 1–2, pp. 185–189, 2004.

[143] J. T. W. Kuo *et al.*, “Novel flexible Parylene neural probe with 3D sheath structure for enhancing tissue integration,” *Lab Chip*, vol. 13, no. 4, pp. 554–561, 2013.

[144] W. Gao *et al.*, “Fully integrated wearable sensor arrays for multiplexed in situ perspiration analysis,” *Nature*, vol. 529, no. 7587, pp. 509–514, 2016.

[145] G. Li and D.-W. Lee, “An advanced selective liquid-metal plating technique for stretchable biosensor applications,” *Lab Chip*, 2017.

[146] W. Y. Wu, X. Zhong, W. Wang, Q. Miao, and J. J. Zhu, “Flexible PDMS-based three-electrode sensor,” *Electrochem. commun.*, vol. 12, no. 11, pp. 1600–1604, 2010.

[147] D.-H. Kim, “stretch force reduction due to nanotube meander- ing. This structure provides a volume per strut of D′L 2 sin(120°) and a calculated density of r,” *Nature*, vol. 320, no. April, pp. 507–511, 2008.

[148] R. C. Huiszoon, S. Subramanian, P. Ramiah Rajasekaran, L. Beardslee, W. Bentley, and R. Ghodssi, “Flexible Platform for In Situ Impedimetric Detection and Bioelectric Effect Treatment of Escherichia coli Biofilms,” *IEEE Trans. Biomed. Eng.*, vol. 66, no. 5, pp. 1337-1345, 2019.

[149] K. G. Ong, J. Wang, R. S. Singh, L. G. Bachas, and C. a Grimes, “Monitoring of bacteria growth using a wireless, remote query resonant-circuit sensor: application to environmental sensing.,” *Biosens. Bioelectron.*, vol. 16, no. 4–5, pp. 305–12, 2001.

[150] P. Stoodley, K. Sauer, D. G. Davies, and J. W. Costerton, “Biofilms as Complex Differentiated Communities,” *Annu. Rev. Microbiol.*, vol. 56, no. 1, pp. 187–209, 2002.

[151] G. A. O’Toole, L. A. Pratt, P. I. Watnick, D. K. Newman, V. B. Weaver, and R. Kolter, “Genetic approaches to study of biofilms,” *Methods Enzymol.*, vol. 310, pp. 91–109, 1999.

[152] M. Feoktistova, P. Geserick, and M. Leverkus, “Crystal violet assay for determining viability of cultured cells,” *Cold Spring Harb. Protoc.*, vol. 2016, no. 4, pp. 343–346, 2016.

[153] Y. W. Kim *et al.*, “Effect of electrical energy on the efficacy of biofilm treatment using the bioelectric effect,” *npj Biofilms Microbiomes*, vol. 1, no. July, p. 15016, 2015.

[154] A. Di Biasio and C. Cametti, “On the dielectric relaxation of biological cell suspensions: The effect of the membrane electrical conductivity,” *Colloids Surfaces B Biointerfaces*, vol. 84, no. 2, pp. 433–441, 2011.

[155] K. Asami, “Characterization of heterogeneous systems by dielectric spectroscopy,” *Progress in Polymer Science (Oxford)*, vol. 27, no. 8. pp. 1617–1659, 2002.

[156] K. Asami, T. Hanai, and N. Koizumi, “Dielectric analysis of Escherichia coli suspensions in the light of the theory of interfacial polarization,” *Biophys. J.*, vol. 31, no. 2, pp. 215–228, 1980.

[157] B. Korth, L. F. M. Rosa, F. Harnisch, and C. Picioreanu, “A framework for modeling electroactive microbial biofilms performing direct electron transfer,” *Bioelectrochemistry*, vol. 106, pp. 194–206, 2015.

[158] S. Park, Y. Zhang, T. H. Wang, and S. Yang, “Continuous dielectrophoretic bacterial

separation and concentration from physiological media of high conductivity," *Lab Chip*, vol. 11, no. 17, pp. 2893–2900, 2011.

[159] J. Wu, M. Lian, and K. Yang, "Micropumping of biofluids by alternating current electrothermal effects," *Appl. Phys. Lett.*, vol. 90, no. 23, 2007.

[160] R. C. Huiszoon, S. Preza, W. E. Bentley, and R. Ghodssi, "FLEXIBLE BIOFILM DETECTION AND TREATMENT PLATFORM CHARACTERIZATION ON PLANAR VERSUS 3D SURFACES," in *8th ASM Conference on Biofilms*, 2018.

[161] R. C. Huiszoon, S. Subramanian, T. E. Winkler, S. Preza, and R. Ghodssi, "Electrodynamic modeling of bacterial biofilm impedance sensing," in *2017 FDA/BMES Frontiers in Medical Devices Conference: Innovations in Modeling and Simulation*, 2017.

[162] F. Lisdat and D. Schäfer, "The use of electrochemical impedance spectroscopy for biosensing," *Analytical and Bioanalytical Chemistry*, vol. 391, no. 5. pp. 1555–1567, 2008.

[163] International Organization for Standardization, "BS EN ISO10993-5," *Int. Stand. ISO 10993-5 Biol. Eval. Med. devices - Part 5 Tests Cytotox. Vitr. methods*, vol. 3 Ed, p. 42, 2009.

[164] Formlabs, "Materials for rapid prototyping," *Mater. data sheet Stand.*, pp. 4–6, 2017.

[165] Stratasys, "Biocompatible Clear MED610 Datasheet." p. 2, 2018.

[166] D. S. L.B., D. A. S.G., D. S. P.P.C., H. J., and D. S. C. C.A., "Cytotoxic effects of different concentrations of chlorhexidine," *Am. J. Dent.*, vol. 20, no. 6, pp. 400–404, 2007.

[167] C. G. Y. Ngan *et al.*, "Optimising the biocompatibility of 3D printed photopolymer

constructs in vitro and in vivo," *Biomed. Mater.*, vol. 14, no. 3, 2019.

[168] G. T. Werneburg *et al.*, "The Natural History and Composition of Urinary Catheter Biofilms: Early Uropathogen Colonization with Intraluminal and Distal Predominance," *J. Urol.*, vol. 203, no. 2, pp. 357–364, 2020.

[169] R. C. Huiszoon, S. Chu, J. M. Stine, L. A. Beardslee, and R. Ghodssi, "Integrated System for Bacterial Detection and Biofilm Treatment On Indwelling Urinary Catheters," *Sci. Rep.*, Submitted July 2020.

[170] K. Zitta *et al.*, "Salicylic acid induces apoptosis in colon carcinoma cells grown in-vitro: Influence of oxygen and salicylic acid concentration," *Exp. Cell Res.*, vol. 318, no. 7, pp. 828–834, 2012.

[171] S. Olliges *et al.*, "In situ observation of cracks in gold nano-interconnects on flexible substrates," *Scr. Mater.*, vol. 58, no. 3, pp. 175–178, 2008.

[172] B. J. Kim, H. A. S. Shin, I. S. Choi, and Y. C. Joo, "Electrical failure and damage analysis of multi-layer metal films on flexible substrate during cyclic bending deformation," in *Proceedings of the International Symposium on the Physical and Failure Analysis of Integrated Circuits, IPFA*, 2011.

[173] D. H. Kim and J. A. Rogers, "Stretchable electronics: Materials strategies and devices," *Adv. Mater.*, vol. 20, no. 24, pp. 4887–4892, 2008.

[174] M. Schlesinger, "Electroless Deposition of Nickel," in *Modern Electroplating: Fifth Edition*, 2011, pp. 447–458.

[175] T. A. Green, "Gold electrodeposition for microelectronic, optoelectronic and microsystem

applications," *Gold Bulletin*, vol. 40, no. 2. pp. 105–114, 2007.

[176] R. C. Huiszoon, S. Chu, L. A. Beardslee, P. R. Rajasekaran, W. E. Bentley, and R. Ghodssi, "IN SITU SENSOR ELECTRODE PATTERNING ON URINARY CATHETERS TOWARDS INFECTION PREVENTION MEMS Sensors and Actuators Lab , Institute for Systems Research , Fischell Department of Bioengineering , 3 Department of Electrical and Computer Engineering , Universit," in *2019 20th International Conference on Solid-State Sensors, Actuators and Microsystems & Eurosensors XXXIII (TRANSDUCERS & EUROSENSORS XXXIII)*, 2019, no. June, pp. 2193–2196.

[177] R. P. Frankenthal, "The Anodic Corrosion of Gold in Concentrated Chloride Solutions," *J. Electrochem. Soc.*, vol. 129, no. 6, p. 1192, 1982.

[178] S. Labs, "BGM121/BGM123 Blue Gecko Bluetooth SiP Module Data Sheet," p. 99, 2017.

[179] Analog Devices, "AD5933 [Material Safety Data Sheet]," p. 40, 2005.

[180] Analog Devices, "AD2S99 Programmable Oscillator," 1995.

[181] S. J. Cole, A. R. Records, M. W. Orr, S. B. Linden, and V. T. Lee, "Catheter-Associated Urinary Tract Infection by Pseudomonas aeruginosa Is Mediated by Exopolysaccharide-Independent Biofilms," *Infect. Immun.*, vol. 82, no. 5, pp. 2048–2058, 2014.

[182] C. J. Alteri, S. N. Smith, and H. L. T. Mobley, "Fitness of Escherichia coliduring urinary tract infection requires gluconeogenesis and the TCA cycle," *PLoS Pathog.*, vol. 5, no. 5, 2009.

[183] K. Wrenn, *Dysuria, Frequency, and Urgency*. 1990.

[184] N. J. Irwin, M. G. Bryant, C. P. McCoy, J. L. Trotter, and J. Turner, “Multifunctional, Low Friction, Antimicrobial Approach for Biomaterial Surface Enhancement,” *ACS Appl. Bio Mater.*, vol. 3, no. 3, pp. 1385–1393, 2020.

[185] K. Yu *et al.*, “Anti-adhesive antimicrobial peptide coating prevents catheter associated infection in a mouse urinary infection model,” *Biomaterials*, vol. 116, pp. 69–81, 2017.

[186] R. Hachem *et al.*, “Novel antiseptic urinary catheters for prevention of urinary tract infections: Correlation of in vivo and in vitro test results,” *Antimicrob. Agents Chemother.*, vol. 53, no. 12, pp. 5145–5149, 2009.

[187] J. L. Pugach, V. DiTizio, M. W. Mittelman, A. W. Bruce, F. DiCosmo, and A. E. Khoury, “Antibiotic hydrogel coated foley catheters for prevention of urinary tract infection in a rabbit model,” *J. Urol.*, vol. 162, no. 3 I, pp. 883–887, 1999.

[188] D. J. Stickler, N. S. Morris, and C. Winters, “Simple physical model to study formation and physiology of biofilms on urethral catheters,” *Methods Enzymol.*, vol. 310, pp. 494–501, 1999.

[189] T. Brooks and C. W. W. Keevil, “A simple artificial urine for the growth of urinary pathogens,” *Lett. Appl. Microbiol.*, vol. 24, no. 3, pp. 203–206, 1997.

[190] H. Fujikawa, A. Kai, and S. Morozumi, “A new logistic model for Escherichia coli growth at constant and dynamic temperatures,” *Food Microbiol.*, vol. 21, no. 5, pp. 501–509, 2004.

[191] T. A. Rowe and M. Juthani-Mehta, “Diagnosis and management of urinary tract infection in older adults,” *Infectious Disease Clinics of North America*, vol. 28, no. 1. pp. 75–89,

2014.

[192] H. C. Flemming and J. Wingender, “The biofilm matrix,” *Nature Reviews Microbiology*, vol. 8, no. 9. pp. 623–633, 2010.

[193] T. M. Hooton *et al.*, “Diagnosis, prevention, and treatment of catheter-associated urinary tract infection in adults: 2009 international clinical practice guidelines from the Infectious Diseases Society of America,” *Clin. Infect. Dis.*, vol. 10, no. 5, pp. 625–663, 2010.

[194] S. N. Abraham and Y. Miao, “The nature of immune responses to urinary tract infections,” *Nature Reviews Immunology*, vol. 15, no. 10. pp. 655–663, 2015.

[195] J. Zhou, L. Zhang, and Y. Tian, “Micro Electrochemical pH Sensor Applicable for Real-Time Ratiometric Monitoring of pH Values in Rat Brains,” *Anal. Chem.*, vol. 88, no. 4, pp. 2113–2118, 2016.

[196] A. Qureshi, J. H. Niazi, S. Kallempudi, and Y. Gurbuz, “Label-free capacitive biosensor for sensitive detection of multiple biomarkers using gold interdigitated capacitor arrays,” *Biosens. Bioelectron.*, vol. 25, no. 10, pp. 2318–2323, 2010.

[197] S. Xiao, L. F. Che, X. Li, and Y. Wang, “A cost-effective flexible MEMS technique for temperature sensing,” *Microelectronics J.*, vol. 38, no. 3, pp. 360–364, 2007.

[198] S. Srey, I. K. Jahid, and S. Do Ha, “Biofilm formation in food industries: A food safety concern,” *Food Control*, vol. 31, no. 2, pp. 572–585, 2013.

[199] H. C. Flemming, “Biofouling in water systems - Cases, causes and countermeasures,” *Appl. Microbiol. Biotechnol.*, vol. 59, no. 6, pp. 629–640, 2002.

[200] M. N. B. Momba, R. Kfir, S. N. Venter, and T. E. Cloete, “An overview of biofilm

formation in distribution systems and its impact on the deterioration of water quality," *Water SA*, vol. 26, no. 1, pp. 59–66, 2000.

[201] A. Kerr *et al.*, "The early stages of marine biofouling and its effect on two types of optical sensors," *Environ. Int.*, vol. 24, no. 3, pp. 331–343, 1998.

[202] J. O. Tobin, R. A. Swann, and C. L. Bartlett, "Isolation of Legionella pneumophila from water systems: methods and preliminary results," *Br. Med. J. (Clin. Res. Ed).*, vol. 282, no. 6263, pp. 515–517, 1981.

[203] R. Murga, T. S. Forster, E. Brown, J. M. Pruckler, B. S. Fields, and R. M. Donlan, "Role of biofilms in the survival of Legionella pneumophila in a model potable-water system," *Microbiology*, vol. 147, no. 11, pp. 3121–3126, 2001.

[204] E. J. Anaissie, S. R. Penzak, and M. C. Dignani, "The Hospital Water Supply as a Source of Nosocomial Infections," *Arch. Intern. Med.*, vol. 162, no. 13, p. 1483, 2002.

[205] M. A. Ryder, "Catheter-related infections: It's all about biofilm," *Top. Adv. Pract. Nurs.*, vol. 5, no. 3, 2005.

[206] A. Wallace *et al.*, "Anti-fouling strategies for central venous catheters," *Cardiovascular Diagnosis and Therapy*, vol. 7. pp. S246–S257, 2017.